

Universidade do Minho
Escola de Engenharia

Tiago dos Santos Abreu

Towards non-invasive glucose monitoring in contact lenses

janeiro de 2025

Towards non-invasive glucose monitoring in contact lenses
Tiago dos Santos Abreu
UMinho | 2025



Universidade do Minho
Escola de Engenharia

Tiago dos Santos Abreu

Towards non-invasive glucose monitoring on contact lenses

Master's Dissertation
Master's in Engineering Physics
Devices, Microsystems and Nanotechnologies

Work supervised by:
Dr. Andrea Capasso
Professor Dr. João Pedro dos Santos Hall Agorreta de Alpuim

January de 2025

COPYRIGHTS AND TERMS OF USED OF WORK BY THIRD PARTS

This is an academic work that can be used by third parties as long as the internationally accepted rules and good practices are respected, concerning copyright and related rights. Thus, this work can be used under the terms set out in the license below. If the user needs permission to be able to make use of the work under conditions not provided for in the indicated license, he must contact the author, through the RepositóriUM of the University of Minho.

License granted to the users of this work



Atribuição
CC BY
https://creativecommons.org/licenses/by/4.0/

ACKNOWLEDGMENTS

First and foremost, I would like to express my gratitude to my supervisor, Dr. Andrea Capasso, for the opportunity, unwavering support, and the possibility to participate in several projects in parallel with the work presented in this thesis, expanding my skills and knowledge in different fields. I would like to express my sincere gratitude to Professor Pedro Alpuim for the invaluable opportunity to work with the 2DMD group at the Iberian International Nanotechnology Laboratory (INL). I deeply appreciate his insightful discussions and thoughtful suggestions during our weekly meetings, which greatly contributed to the development of this work.

I extend my acknowledgments to all my colleagues in the 2DMD group for their support, engaging discussions, and training sessions, in particular Vicente Lopes, Tiago Pereira and Gabriel Moreira for all the shared knowledge and conversations during breaks that were instrumental for my growth and development. I would like to thank Mafalda for generously providing the graphene biosensors used in the glucose experiments, as well as for her support throughout the process.

Finally, I would like to express my deepest gratitude to my family and friends for their unwavering support and continuous encouragement throughout my academic journey. Their belief in me has been a constant source of strength and inspiration.

STATEMENT OF INTEGRITY

I hereby declare having conducted this academic work with integrity. I confirm that I have not used plagiarism or any form of undue use of information or falsification of results along the process leading to its elaboration. I further declare that I have fully acknowledged the Code of Ethical Conduct of the University of Minho.

RESUMO

Diabetes mellitus, uma doença metabólica prevalente que afeta centenas de milhões de pessoas em todo o mundo, exige uma monitorização contínua da glicose para uma gestão eficaz. Os métodos atuais de monitorização da glicemia, como os glicosímetros comerciais, embora precisos, são invasivos e desconfortáveis, realçando a necessidade de alternativas não invasivas e ultrassensíveis. Os biomarcadores presentes no sangue foram encontrados em menor quantidade nas lágrimas, abrindo a possibilidade de usar o olho para monitorização não invasiva. As lentes de contacto surgem como potenciais candidatas para uma plataforma de biossensores, uma vez que mantêm contacto direto com o filme lacrimal. Aqui, apresentamos uma plataforma de deteção de glicose utilizando transístores de efeito de campo de grafeno controlados por eletrólitos (EG-GFETs) funcionalizados com enzimas glicose oxidase. A caracterização detalhada do material por espectroscopia Raman e fotoeletrônica de raios-X confirma a imobilização bem-sucedida da enzima, com um aumento acentuado do conteúdo de azoto de 0,9% para 7,6% de concentração atómica na superfície do grafeno, indicando cobertura com glicose oxidase. Os EG-GFET demonstram um limite de deteção ultrabaixo de 1 attomolar, com uma mudança consistente de voltagem do ponto de Dirac de +26 ± 4 mV e uma resposta linear a seis ordens de grandeza (até 1 picomolar, com uma sensibilidade de 10, 6 mV/década). O sensor mantém uma elevada seletividade na presença de interferentes e em lágrimas artificiais (com um limite de deteção de 100 attomolar). Com base neste conhecimento, desenvolvemos ainda uma estratégia dedicada à potencial integração de uma plataforma de deteção de glicose baseada em lentes de contacto revestidas de grafeno. Estas lentes com grafeno foram caracterizadas minuciosamente através de diversas técnicas para avaliar a sua qualidade, incluindo a morfologia, continuidade e uniformidade das camadas. O método de transferência de grafeno foi otimizado para superar desafios anteriores, como a rutura do filme e a cobertura irregular, incorporando um suporte impresso em 3D, permitindo a melhoria do processo de transferência. Foi desenvolvido um protocolo para funcionalizar o grafeno para deteção de glicose, integrando um modelo personalizado impresso em 3D que garantiu a imersão controlada e a proteção da lente durante a funcionalização. A espectroscopia Raman e as medições do ângulo de contacto foram empregues para monitorizar as modificações causadas no grafeno em cada etapa de funcionalização. Além disso, a espectroscopia ultravioleta-visível confirmou a interação bem-sucedida entre a glicose e a enzima imobilizada, com evidências de produção de peróxido de hidrogénio.

Palavras-chave: Diabetes; Monitorização de glicose; Grafeno; Transístores de efeito de campo; Lentes de contacto.

ABSTRACT

Diabetes mellitus, a prevalent metabolic disorder affecting hundreds of millions worldwide, demands continuous glucose monitoring for effective management. Current blood glucose monitoring methods, such as commercial glucometers, though accurate, are invasive and uncomfortable, highlighting the need for non-invasive, ultra-sensitive alternatives. The biomarkers present in the blood have been found in smaller quantities in the tears, opening the possibility of using the eye for non-invasive monitoring. Contact lenses emerge as a potential candidate for a biosensing platform, as they maintain direct contact with the tear film. Here, we present a glucose sensing platform using electrolyte-gated graphene field-effect transistors (EG-GFETs) functionalized with glucose oxidase enzymes. Detailed material characterization by Raman and X-ray photoelectron spectroscopies confirms successful enzyme immobilization, with a marked increase in nitrogen content from 0.9% to 7.6% atomic concentration on the graphene surface, indicating substantial glucose oxidase coverage. The EG-GFETs demonstrate a ultra-low limit-of-detection of 1 attomolar, with a consistent Dirac point voltage shift of +26 ± 4 mV and a linear response across six orders of magnitude (up to 1 picomolar, with a sensitivity of 10.6 mV/decade). The sensor maintains high selectivity in the presence of interferents and in complex media, such as artificial tears (with a limit-of-detection of 100 attomolar). Moving from this know-how, we further develop a strategy dedicated to the potential integration of a graphene-based glucose sensing platform in contact lenses. Graphene-coated lenses were thoroughly characterized using multiple techniques to assess their quality, including morphology, continuity, and layer uniformity. The graphene transfer method was optimized to overcome previous challenges, such as film rupture and uneven coverage, by incorporating a newly designed 3D-printed holder, enabling the upscaling of the transfer process. A specific protocol was developed to functionalize the graphene for glucose sensing, integrating a custom 3D-printed template that ensured controlled immersion and protection of the lens during functionalization. Raman spectroscopy and water contact angle measurements were employed to monitor modifications caused in the graphene at each functionalization step. Additionally, ultraviolet-visible spectroscopy confirmed the successful interaction between glucose and the immobilized enzyme, with evidence of hydrogen peroxide production.

Keywords: Diabetes; Glucose monitoring; Graphene; Field-effect transistors; Contact lenses.

INDEX

Copyrights and terms of used of work by third parts ii

Acknowledgments iii

Statement of integrity iv

Resumo v

Abstract vi

List of Abbreviations, Initials and Acronyms x

Figure Index xi

Table index xvii

1. Introduction 1

1.1 Graphene 3

1.1.1 Chemical vapor deposition growth 6

1.2 Graphene field effect transistor technology 9

1.2.1 Biosensing 9

1.3 Graphene-based contact lens technology 12

1.3.1 Biosensing 13

2. Materials and Methods 17

2.1 Graphene production 17

2.1.1 Transfer 17

2.1.2 Functionalization 18

3. Characterization Techniques 19

3.1 Optical microscopy 19

3.2 Scanning electron microscopy 20

3.3 Raman spectroscopy 21

3.4 X-ray photoelectron spectroscopy 24
3.5 Ultraviolet-visible spectroscopy 25
3.6 Contact angle measurements 26
3.7 Field effect transistor measurements 28
4. Glucose sensing via electrolyte-gated graphene field-effect transistor 29
4.1 Functionalization and characterization of the graphene channel 29
4.2 Analysis of the glucose sensing mechanism 35
4.3 Investigation of the sensor selectivity 38
4.4 Conclusion 43
5. Towards glucose sensing in graphene-based contact lenses 45
5.1 Graphene integration in contact lenses 45
5.2 Graphene functionalization for glucose sensing 54
5.2.1 Optimization procedure 57
5.3 Conclusion and future outlook 65
References 68
Appendix I 86
Appendix II 87
Appendix III 88
Appendix IV 89
Appendix V 90
Appendix VI 91
Appendix VII 92
Appendix VIII 93
Appendix IX 94
Appendix X 95

Appendix XI 96

Appendix XII 97

Appendix XIII 98

Appendix XIV 99

Appendix XV 100

Annex I 101

List of Abbreviations, Initials and Acronyms

2D – Two dimensional

CA – Contact angle

CL – Contact lens

Cu – Copper

CVD – Chemical vapor deposition

DA - Dopamine

DI – Deionized

DMF – Dimethylformamide

DNA - Deoxyribonucleic acid

DAC - Digital-to-Analog converter

DDT - 1-Dodecanethiol

DMSO - Dimethyl sulfoxide

EDL – Electric double-layer

EGTs - Electrolyte-gated transistors

Gr – Graphene

G-FET – Graphene Field Effect Transistor

EG-GFET – Electrolyte-gated graphene field effect transistor

EM - Electromagnetic

ERG - Electroretinogram

FAD - flavin adenine dinucleotide

FET – Field Effect Transistors

FWHM - Full width at half maximum

GOx – Glucose Oxidase

LED - Light-emitting diode

PBASE - 1-pyrene-butyric acid n-hydroxy succinimide ester

PBS - Phosphate buffered saline

PCE - Power Conversion Energy

PDMS - Polydimethylsiloxane

PEDOT - Poly(3,4-ethylenedioxythiophene)

PET – Poly(ethylene terephthalate)

PMMA - Poly(methyl methacrylate)

PPM - Parts Per Million

RGO – Reduced Graphene Oxide

SAM - Self-assembled monolayer

Si – Silicon

SiO_2 – Silicon Dioxide

WCA – Water Contact Angle

FIGURE INDEX

Figure 1: (a) Lattice structure of graphene (a1 and a2 are the lattice unit vectors and δi, i=1,2,3 are the nearest-neighbour vectors) (b) Graphite (c) Carbon nanotubes (d) Fullerenes (e) Electronic dispersion in the honeycomb lattice. Left: energy spectrum (in units of t) for finite values of t and t', with t=2.7 eV and t'=−0.2t. Right: zoom in on the energy bands close to one of the Dirac points. Reproduced from [46]. . 4
Figure 2: Schematic of general elementary steps of a typical CVD process. Reproduced from [83]. 7
Figure 3: (a) Schematic diagram of the transfer process of CVD-grown graphene on copper foil by wet transfer. Reproduced from [84]. (b) Wet transfer method developed to transfer the CVD-grown graphene to the CLs at INL. 8
Figure 4: (a) Functionalized GFET with bio-recognition elements. (b) Schematic of the Debye screening effect makes biomolecules carry zero net charge due to the Debye screening effect of ions in electrolyte. Reproduced from [94]. (c) Typical transfer curve I_{ds} (V_g) of a GFET, illustrating key metrics in its use as a sensor. Smaller graphs, from top to bottom represent the change in the voltage of the charge neutrality point V_{CNP}, change in the transconductance of electrons g_m(e) or holes g_m(h), and change in the current amplitude, including at the charge neutrality point I_{CNP}. Reproduced from [62]. 11
Figure 5: (a) Operation of the soft, smart CL. Reproduced from [130]. (b) Photographs (left, off-state; right, on-state) of operating wireless display with lens shape located on the artificial eye. Scale bars, 1 cm. Reproduced from [131]. (c) Schematic of the reading circuit for wireless sensing on CLs. Reproduced from [131]. (d) Working principle of the device and current pathway through a fractured graphene woven fabric. Reproduced from [118]. (e) Graphene as a shielding layer against EM waves and dehydration protection. Reproduced from [132]. 15
Figure 6: Optical microscope used at INL facilities. 20
Figure 7: (a) SEM at INL facilities. (b) Close up photograph of the stage. 21
Figure 8: (a) Three types of scattering processes that can occur when light interacts with a molecule. (b) Diagram of the Rayleigh and Raman scattering processes. Reproduced from [138]. 22
Figure 9: (a) Raman spectra of pristine (top) and defected (bottom) graphene. Reproduced from [140]. (b) Raman spectra of graphene with different number of layers. Reproduced from [143]. 23
Figure 10: Raman confocal microscope at INL's facilities. (a) Microscope and fiber optic Raman probe. (b) CCD detectors and laser excitation source. 23

Figure 11: XPS analysis shows the binding energies of carbon species. (a) A table of C 1s binding energy ranges for various carbon compounds. (b) XPS spectrum on the C 1s region, with a prominent peak at 284.5 eV, corresponding to sp^2-hybridized carbon. Reproduced from [144]. 24
Figure 12: System used for (a) liquid samples and (b) solid samples at INL facilities. 26
Figure 13: Schematic illustrations show graphene wettability modulation by doping-induced Fermi level shifts. Reproduced from [158]. 27
Figure 14: Water contact angle at INL's cleanroom. (a) Water Contact Angle setup. (b) Close up photograph of the stage and DI water syringe of the setup. 28
Figure 15: Detailed characterization of graphene's functionalization process for glucose detection. (a) Functionalization process. (b) Raman spectra of each stage involved in the immobilization of GOx molecules on graphene: pristine graphene (Gr, black), PBASE modification (Gr/PBASE, red) and GOx immobilization (Gr/PBASE/GOx, blue). Each spectrum is an average of 1500 measurements. (c) 2D vs G frequency plot of the 1500 measurements of Gr, Gr/PBASE and Gr/PBASE/GOx. (d) Mechanical strain (ε, %) vs charge (hole) density (n, 10^{12} cm^{-2}) plot of 1500 measurements for each functionalization step. The plot is a linear transformation of the 2D vs G frequency plot shown in Figure 15c. 31
Figure 16: (a) Deconvoluted high-resolution C 1s and (b) N 1s spectra of Gr, Gr/PBASE and Gr/PBASE/GOx. 32
Figure 17: Functionalization and characterization of electrolyte-gated graphene field-effect transistors (EG-GFETs) for glucose detection. (a) Schematic of an EG-GFET and the total functionalization process involved in graphene modification for glucose sensing: 1) DDT - Au gate passivation. 2) PBASE - non-covalent modification with pyrene linkers + GOx - immobilization of the biorecognition element, GOx. 3) ETA - blocking of unreacted sites of PBASE. (b) Transfer curves of one EG-GFET measured after each functionalization stage and (c) their respective average value of the V_{DIRAC} for 50 transistors (data is represented in mean ± standard error mean (sem)). 34
Figure 18: Glucose sensing via EG-GFETs and Raman spectroscopy in 1x PBS. (a) Comparison of the ΔV_{DIRAC} as a function of glucose concentration for Gr^{-}, Gr^{-}/PBASE and Gr^{-}/PBASE/GOx/ETA. In the latter, V_{DIRAC} positively shifts as the glucose concentration increases, resulting in p-type doping with the lowest reported glucose LOD of 1 aM. The negative control tests show the opposite response. The data are presented as mean ± sem. (b) Transfer curve trend of one transistor for the different glucose concentrations in the linear range (1 aM-1 pM). (c) 2D vs G frequency plot of Gr/PBASE/GOx/ETA with varying glucose concentration (1 nM-1 mM). For each concentration, a distribution of the peaks position

within 300 measurements (over a total area of 300 μm^2) is displayed with the corresponding average point. The surface was treated with DDT to passivate the Au electrodes. 36
Figure 19: H_2O_2 measurements on EG-GFETs. (a) 1 µM-1mM H_2O_2 influence on V_{DIRAC} of bare graphene surfaces (only DDT passivation). The sensor shows n-type doping. (b) 1 mM H_2O_2 measured on Gr/PBASE/Gox/ETA, showing p-type doping. On the same sensor, after washing with 1 x PBS (Glu 0 M), glucose (Glu nM-Glu mM) was measured, with no variation of the V_{DIRAC} with increasing concentrations. The same concentration of H_2O_2 (1 mM) exhibited opposite behaviour for Gr and Gr/PBASE/GOx/ETA, confirming that glucose detection is based on the detection of H_2O_2. 37
Figure 20: Selectivity of the EG-GFETs with Gr/PBASE/GOx/ETA configuration. (a) Comparison of the sensors' response to glucose and lactate in 1 x PBS, showing linear and erratic trends, respectively. (b) Calibration curve of the ΔV_{DIRAC} as a function of glucose, ascorbic acid and lactate concentrations in 1 x PBS, in a ratio of 1:1:1, showcasing the sensitivity and selectivity of the sensors in a complex medium. 39
Figure 21: Selectivity of the EG-GFETs with Gr/PBASE/GOx/ETA configuration. Calibration curve of the ΔV_{DIRAC} as a function of glucose concentrations in an artificial tear, showcasing the sensitivity and selectivity of the sensors in a complex medium. 40
Figure 22: (a-b) OM imaging of a bare and a graphene-coated CL, respectively. (c-d) SEM imaging of bare CLs with 469x and 1000x magnification, respectively. (e-f) SEM imaging of graphene-coated CLs with 500x and 1000x magnification, respectively. 46
Figure 23: Raman Spectrum of (a) the template utilized as support and (b) a bare CL. 47
Figure 24: Graphene coated CL. (a) Optical Image (b) Raman Spectrums corresponding to the crosses marked on (a) 47
Figure 25: (a) 2D vs G frequency plot of the 500 measurements of graphene-coated CL before and after being stored in CL solution for 1 day. (The before and after corresponding to the purple and dark cyan, respectively). (b) Mechanical strain (ε, %) vs charge (hole) density (n, 10^{12} cm^{-2}) plot of the measurements done in (a). The plot is a linear transformation of the 2D vs G frequency plot shown in Figure 25a. 48
Figure 26: Three different lenses after polymer removal, where the one indicated with the blue arrow was not fully covered with graphene and the two indicated by the red arrow were fully covered. 49
Figure 27: (a) 3D-printed template designed to optimize the transfer process (inset: graphene-coated CLs after transfer). (b) Optical image of the graphene (c) Average Raman Spectrum of 10 maps taken on the four different graphene-coated CLs. 50
Figure 28: Graphene-coated CL with four electrodes made of silver paste. 51

Figure 29: Setup for the measurement of the graphene conductivity with Au electrodes on top of a flattened CL. 52
Figure 30: (a) Comparison of the optical transmittance between a graphene-coated CL and a bare CL and (b) Difference in percentage between both. 53
Figure 31: (a) Setup for the dehydration experiment. (b) Comparison of the weight loss between the vials sealed with a bare and a graphene-coated CL. 54
Figure 32: (a) Vial and (b) CL container utilized for functionalization. 55
Figure 33: Microscopic images of the graphene after PBASE incubation. 55
Figure 34: Raman Spectrum at different laser powers after (a) 4h incubation and (b) 1 day. 56
Figure 35: (a) Optical image of the graphene after GOx incubation and (b) Raman Spectrum. 57
Figure 36: Template design for the functionalization of graphene on the CL surface (a) without the vial and (b) with the vial. The process for the functionalization is depicted from (c) to (e). 58
Figure 37: (a) Optical image of graphene-coated CL before being submerged in DMSO, with (b) its corresponding Raman spectra. (c) Optical image of graphene-coated CL after being submerged in DMSO, with (d) its corresponding Raman spectra 59
Figure 38: (a) Microscope Image of the graphene-coated lens and highlighted area of a map taken. (b) Raman spectra of each stage involved the immobilization of GOx molecules on graphene: pristine graphene (Gr, orange), PBASE modification (Gr/PBASE, violet) and GOx immobilization (Gr/PBASE/GOx, olive). Each spectrum is an average of 1000 measurements. (c) 2D vs G frequency plot of the 1000 measurements of Gr, Gr/PBASE and Gr/PBASE/GOx in both CL and Si/SiO_2. (The Gr, Gr/PBASE and Gr/PBASE/GOx of Si/SiO_2 correspond to the black, red and blue, respectively). (d) Mechanical strain (ε, %) vs charge (hole) density (n, 10^{12} cm^{-2}) plot of the measurements for each functionalization step in each substrate. The plot is a linear transformation of the 2D vs G frequency plot shown in Figure 38c. 61
Figure 39: (a) 2D vs G frequency plot and (b) linear transformation with respect to the charge density and mechanical strain of 3 sets of points corresponding to Gr/CL. Each set of points are a combination of at least 500 measurements. 62
Figure 40: Average WCA measurements over time (inset: one of the measurements). 63
Figure 41: WCA characterization of the functionalization process (a) in CLs and (b) Si/SiO_2 substrate. 64
Figure 42: (a) Molecular absorption spectrum of 1 mM glucose solution after reacting with the fully functionalized CL. (b) Molecular absorption spectrum different concentrations of H_2O_2. In both spectrums glucose (1 mM in 1 x PBS) was utilized as reference. 65

Figure 43: (a) Raman spectra of GOx: powder form and dissolved in DI water. (b) The 2800-3100 cm^{-1} range (highlighted by a yellow stripe in (a)) fitted with Lorentzian functions. (c) Gr/PBASE and Gr/PBASE/GOx spectra zoomed-in in the 2800-3100 cm^{-1} range, showing a small contribution at 2947 cm^{-1} in the Gr/PBASE/GOx spectrum, not visible in Gr/PBASE. 86
Figure 44: FWHM distribution of the 2D and G peaks of graphene for Gr, Gr/PBASE and Gr/PBASE/GOx on Si/SiO_2. 87
Figure 45: XPS survey spectra for Gr, Gr/PBASE and Gr/PBASE/GOx. 88
Figure 46: (a) EG-GFETs' finished wafer. (b) Layout of EG-GFETs' chip. Drains (yellow pads), sources (blue pads), gates (green pads) and graphene channels (red rectangles). 89
Figure 47: Variation of 2D and G modes frequency after Au passivation with DDT molecules. Visualization on (a) 2D vs G frequency plot and on (b) mechanical strain vs charge density plot. Variation of 2D and G modes frequency after Gr incubation with DMSO. Visualization on (a) 2D vs G frequency plot and on (b) mechanical strain vs charge density plot. All data shown are a combination of 1500 measurements for each step. 90
Figure 48: Calibration curves for Gr*, Gr/PBASE and Gr/PBASE/GOx/ETA in nM-mM (saturation) range. The three cases show almost no variation with an increase in glucose concentration. 91
Figure 49: Corresponding (a) charge density and (b) mechanical strain calibration curves extracted from 2D and G position values of Figure 40c. At 1 mM, there is an overall increase in hole concentration of ~9 x 10^{12} cm^{-2}. The mechanical strain varies minimally between concentrations (1 nM-1 mM, with a ~ 0.1% increase in compressive strain only after 1 nM was detected. 92
Figure 50: Calibration curve of (a) lactate sensing and (b) ascorbic acid on EG-GFETs in Gr/PBASE/GOx/ETA configuration within the same concentration range as glucose (aM-nM). As opposed to glucose, the sensors had an erratic behavior in response to lactate, proving the selectivity to glucose. 93
Figure 51: CL after being cut in four different zones pointed by the black arrows and flattened on a glass coverslip..... 94
Figure 52: (a) Shadow mask on top of graphene before the sputtering of Au (b) Gr/Cu foil after the sputtering of Au (c) Photograph of the Au electrode/Gr/CL after scooping. (d) Setup of the probe station in the cleanroom. (e) Photographs during the conductivity measurement of the CL using a template as support. 95

Figure 53: (a) Optical image of the interface between the 10nm Au electrode/Gr-Gr and (b) Optical image of the interface between the 30nm Au electrode/Gr-Gr and (c) Raman Spectra in the indicated crosses in (b). 96
Figure 54: Raman Spectra of the CL (a) before and (b) after the PBASE functionalization in three random positions on the CL. 97
Figure 55: FWHM distribution of the 2D and G peaks of graphene for Gr, Gr/PBASE and Gr/PBASE/GOx on Si/SiO_2. 98
Figure 56: H_2O_2 molecular absorption for different concentrations using PBS a reference. 100

TABLE INDEX

Table 1. Relative at. % of carbon, nitrogen, and oxygen calculated from C 1 s, N 1 s, and O 1 s high-resolution peaks, respectively, for the as-transferred graphene, Gr/PBASE, and Gr/PBASE/GOx samples. 32

Table 2. Components used to fit the C 1 s spectra of the as-transferred graphene, Gr/PBASE, and Gr/PBASE/GOx samples. For each of them, the binding energy position in eV and the relative atomic concentration (at. %) are reported. 33

Table 3. State-of-the-art glucose sensing, considering their sensing system, detection method, LOD, linear range, sensitivity and selectivity. 41

Table 4: Values of the graphene peaks in the functionalization process 99

1. INTRODUCTION

Glucose is a primary source of energy for cellular activity in the body, and maintaining its optimal concentration in the blood is crucial. However, certain patients suffer from metabolic disorders that affect glucose processing. *Diabetes mellitus*, a major metabolic disorder that impairs glucose regulation, affects more than 400 million people worldwide and is projected to impact up to ~700 million people by 2045 [1], [2]. This condition is characterized by hyperglycemia resulting from defects in insulin secretion or action [3], [4]. Without proper management, diabetes can lead to severe complications such as blindness, cardiovascular diseases, nerve damage, and even cancer [3]. Many glucose measurement approaches exist, and efforts are being devoted to achieving functional continuous glucose monitoring. Glucose sensors range from optical (by using tilted fibers, photonic crystals or liquid crystals) [5], [6] to electrochemical (through functionalized graphene derivatives and modified or bare electrodes) [7], [8]. Essentially, they can be classified as non-enzymatic or enzymatic. Non-enzymatic sensors rely on the direct electrochemical oxidation of glucose, induced by the intrinsic catalytic properties of the electrode materials [9], which can be metallic (*e.g.*, Pt, Au, or Cu), polymeric or carbon-based [10], [11]. These sensors are conceptually simple, versatile, low-cost, highly stable and durable [12], [13]. However, they lack biorecognition probes, which are crucial when sensing any analyte in highly complex media such as body fluids [12]. Although more costly and susceptible to degradation over time due to environmental factors [14], enzymatic glucose sensors offer unmatched sensitivity and selectivity toward glucose. The integration of a glucose-recognition element, such as glucose oxidase (GOx) enzymes, allows selective transducing only when exposed to glucose [15], [16]. Enzymatic finger-pricking sensors are suitable and for accurate at-home monitoring of blood glucose levels (between 4.4 and 6.7 mM in the daytime) [17], [18], but these can be perceived as invasive, uncomfortable, and risky, leading to reluctance or rejection in 30 % of patients [19]. Other biofluids, such as tears and saliva (normal glucose levels of 0.1–0.2 mM for both), have been proposed as diagnostic biofluids to replace blood. They are considered ideal for non-invasive glucose monitoring but would require high sensitivity, since their fasting glucose concentrations are lower than those of blood (averaging > 0.4 mM for tears and > 0.8 mM for saliva *vs.* > 7 mM for diabetic patients) [20], [21], [22], [23], [24]. At present, tear- and saliva-based glucose sensors have not progressed enough to enter the market.

In recent years, graphene emerged as a key material for electronics and sensing technologies, capitalizing on high surface-to-volume ratio, excellent carrier mobility and ease in functionalization [25], [26], graphene represents an ideal platform to interact efficiently with the surrounding environment and react to external stimuli with high sensitivity. In particular, the ability to transduce biological interactions into measurable electrical signals is valuable for biosensing. Graphene field-effect transistors (GFETs) have been implemented as biosensors able to detect a wide array of analytes, ranging from gases to biological molecules, at extremely low concentrations and with exceptional precision [27], [28], [29]. Modification with specific recognition elements allows fine-tuning the selectivity of GFETs, even in complex body fluids [30], [31], [32]. Particularly, electrolyte-gated graphene field-effect transistors (EG-GFETs) exploit a highly efficient local gating mechanism to improve sensitivity.

As healthcare continues to evolve, wearable technology has shifted significant attention into integrating selective glucose biosensing into stable and biocompatible platforms. Contact lenses (CLs) are now the gold standard for futuristic wearable tear-based glucose monitoring, as they can provide continuous physical contact with the eye without irritation [33]. The abundance of biomarkers on the tear film and the continuous touch with the eye have promoted the creation of several innovative methods for tracking biological signals from the eyes, offering minimally invasive monitoring of disease onset [34], [35], [36]. Integration of electronic components can be embedded into smart CLs, allowing monitorization of the biometric data [37], [38]. These point-of-care, portable devices can potentially treat eye diseases by delivering drugs, heat, light, and electrical stimulation [39]. [40]. Important factors to consider are their portability, affordability, and user-friendliness [41]. [42]. To this end, the use of biocompatible and flexible electrode materials is imperative. Graphene, the famous single layer of carbon atoms, is known for its outstanding textbook properties, such as inherent low light absorption, high conductivity, favorable mechanical properties and easy functionalization. The integration of graphene should maintain the optical properties of the CLs while selectively detecting and real-time monitoring the intended biomarker with minimal invasiveness [33], [37], [41], [43].

This dissertation is divided into five chapters. In the introductory chapter, the properties of graphene, its production and extensive applications of different fields are explored with a focus on the biosensing field, were ease to functionalization enables fabrication of biosensors for different types of molecules, including glucose. The motivation behind the CLs technology is then described, highlighting the different types of diseases that are reflected in the eye and the current technology that integrates graphene to sense these biomarkers. The second chapter gives a comprehensive description of the materials and methods

employed in fabrication of the devices used in this thesis. The following chapter introduces all the characterization techniques essential for measuring and understanding the devices. Chapters four and five are related to the experimental work, showcasing all results and their discussion. The former focuses in validating the glucose detection theory through different types of experiments and further exploring the glucose sensing mechanisms in more complex mediums, and the latter focuses on in-depth analyses of graphene-coated lenses and development of protocols that could benefit future biosensing contact lenses.

1.1 Graphene

Graphene is simply a single layer of carbon atoms, which was first isolated in 2004 and earned Andre Geim and Kostya Novoselov the 2010 Nobel Prize in Physics [44],[45]. This layer consists of two equivalent carbon sublattices A and B arranged in a hexagonal honeycomb form (Figure 1a) [44]. Due to the flexibility of the graphene bonds, it can exist as different allotropes. Graphite, for example, can be viewed as a stack of graphene layers, where the layers are held together by weak van der Waals forces (Figure 1b). Carbon Nanotubes are rolled-up cylinders of graphene, which exhibit exceptional strength and conductivity (Figure 1c). Fullerenes are molecules consisting of wrapped graphene by the introduction of pentagons on the hexagonal lattice, forming spherical or cylindrical structures (Figure 1d). These can be used to understand the several physical and electronic properties of each [46]. The graphene bonds are characterized by hybridization between one *s* orbital and two *p* orbitals leading to a trigonal planar structure. Each atom of carbon forms three sp^2 bonds to its nearest neighbouring carbon atoms which are 1.42 Å apart (Figure 1a), leaving one *p* orbital unchanged. All bonds between the carbon atoms are known as sigma bonds and are responsible for the robustness of the lattice structure in all allotropes [46]. Moreover, a delocalized weaker bond is formed by the unaffected p orbital with neighbouring carbon atoms, which is perpendicular to the planar structure, and responsible for creating the π band which gives the material's optoelectronic properties [46], [47]. The π electrons are responsible for the formation of the π and π^* states, corresponding to the valence and conduction band, respectively. These two bands touch at six points that can be reduced to a pair, K and K', which are independent of one another due to symmetry (Figure 1e). These points are named Dirac points and are where the conduction and valence bands have a very tiny overlap making it a zero-band gap material [48].

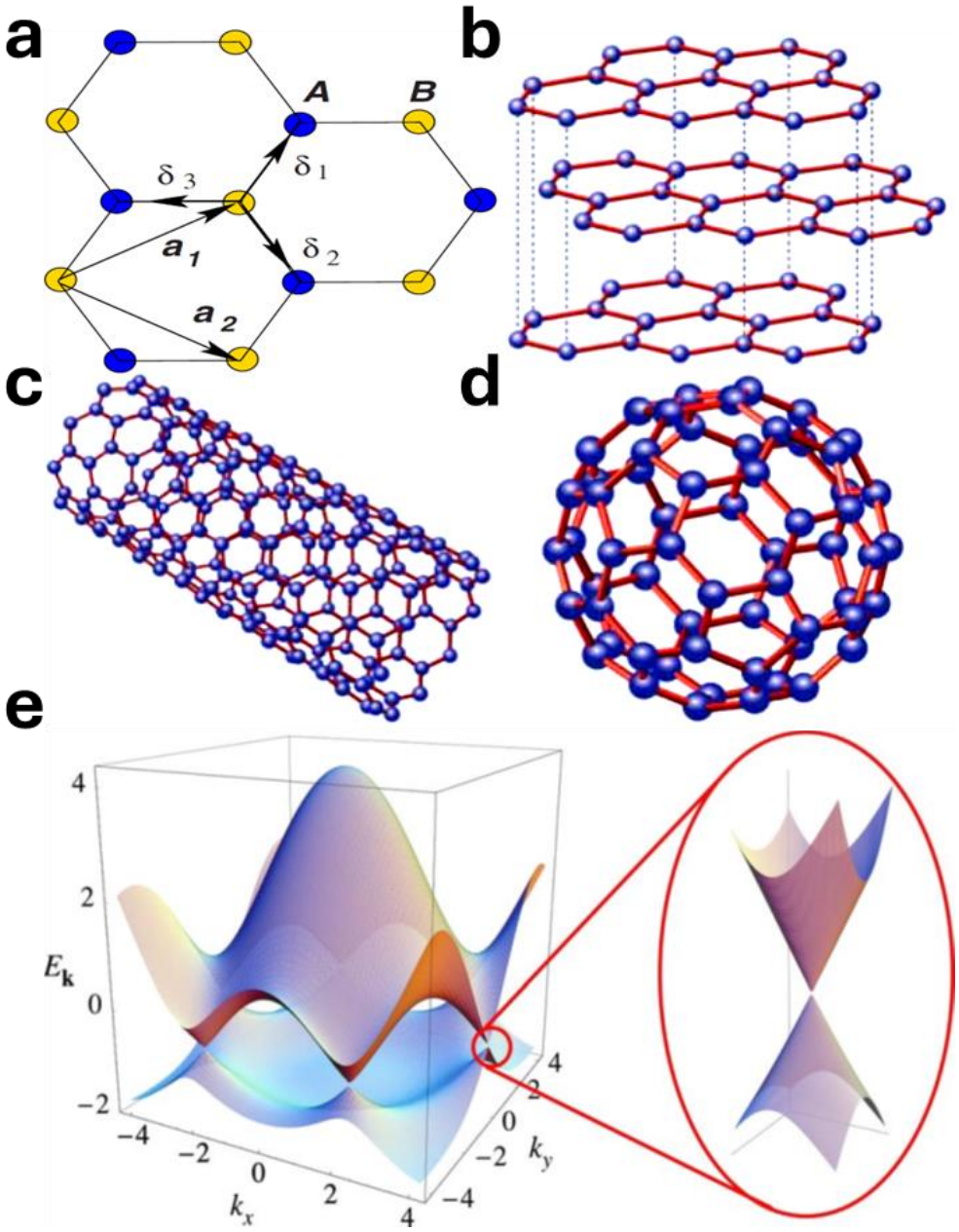


Figure 1: (a) Lattice structure of graphene (a1 and a2 are the lattice unit vectors and δi, i=1,2,3 are the nearest-neighbour vectors) (b) Graphite (c) Carbon nanotubes (d) Fullerenes (e) Electronic dispersion in the honeycomb lattice. Left: energy spectrum (in units of t) for finite values of t and t', with t=2.7 eV and t'=−0.2t. Right: zoom in on the energy bands close to one of the Dirac points. Reproduced from [46].

The extraordinary characteristics of graphene originate precisely from this unaffected *p* orbital which results in an extremely stiff material, that exhibits very high thermal conductivity, has zero effective mass, is impermeable to gases, and displays high mobility of charge carriers [49]. At room temperature, graphene can achieve carrier mobilities of around 10,000 $cm^2/V.s$ when voltage is applied. Additionally,

it shows a robust ambipolar electric field, which indicates that the electric field has a substantial impact on both electrons and holes. Compared with traditional materials, graphene exhibits higher stiffness, elasticity and tensile strength [50], and is even considered the strongest nanomaterial ever tested. Optically, a single layer of graphene can transmit light up to 97.7% (absorbing only 2.3% of the light) [51]. Such textbook properties have prompted the integration of graphene to improve several fields [52], [53], [54]. In the context of solar cells, the ability to easily dope graphene, and thus reducing the graphene sheet resistance allowed an improvement in power conversion efficiency (PCE) of a factor of 4.5 compared with the undoped device [55] and further improvements in PCE were achieved when using graphene for transparent electrodes for perovskite solar cells [56]. Other types of electronic devices that benefit from graphene are supercapacitors. It was shown that the preparation method has a high impact on the device's performance, as its high capacitance and energy density depend on the quality of the graphene [57], [58]. Furthermore, chemically modified graphene with controlled dope levels improves capacitance [59]. Besides electronic research, graphene has also been explored in photonic applications, more specifically in transistor-based photodetectors. Compared with conventional photodetectors, the use of single- and multi-layer graphene leads to high bandwidth light detection, zero source-drain bias and dark current operation, and good internal quantum efficiency [60]. Further research used a double-layer heterostructure allowing room-temperature photodetection from the visible to the mid-infrared range with high responsivity [61]. Graphene has been also employed as a transducing material for sensing applications, where it is used for the transport of electrical current. The ease for immobilization of biorecognition elements on its surface allows for specific capture of targeted analytes, where the interaction between these two elements causes electrostatic changes in the environment which graphene is sensitive to, allowing detection [62], [63]. Since the first synthesis of graphene by mechanically exfoliating graphite (Scotch tape method) [44], several methods have been developed to improve graphene growth quality and in different scalabilities. The methods for preparing graphene can be divided into two main categories: the bottom-up and the top-down [64], [65]. The bottom-up method involves assembling smaller units into larger nanostructures through various physical and chemical processes. In contrast, the top-down method involves breaking down bulk materials into smaller structures to create the desired nanostructures. Top-down approaches are intrinsically the best solution to produce graphene materials with high yields and in large, scalable volumes [66]. Examples of these techniques include mechanical exfoliation and liquid-phase exfoliation. The bottom-up approach includes processes like chemical vapor deposition (CVD) and thermal decomposition of SiC.

1.1.1 Chemical vapor deposition growth

CVD is the most common method to produce graphene and is defined by the deposition of a solid on a heated surface from a chemical reaction in the vapor phase [67]. CVD has cemented its position as a crucial technique for the preparation and synthesis of graphene for various applications [68], [69], having been used to successfully grow a 30-inch graphene film, paving a way to produce graphene at a large scale [70]. Comparing the materials used as catalysts for graphene growth, the most used being Nickel and Copper (Cu), Cu is the most used due to having a higher catalytic activity for the growth [71]. Cu has an ultralow carbon solubility (7.4 ppm at 1020°C) [72], meaning that even if the hydrocarbon concentration is high or the growth time is long there will not occur carbon precipitation and saturation, thus only a small amount of carbon dissolved in the Cu resulting in a large area of monolayer graphene, with only few-layered graphene flakes being present in low percentages [68], [73], [74]. An important factor to have in consideration is the effect of hydrogen (H_2), which can negatively impact the quality of the graphene film [75]. This happens because suboptimal ratio between methane (CH_4) and H_2 can lead to an inhibitor role of graphene, where the H_2 dissociative chemisorption competes with CH_4 dissociative dehydrogenation on surface sites [75]. In the other hand, it can enhance the provision of CH radicals needed for graphene nucleation [76]. Moreover, the purity and pre-treatment of Cu also play a crucial role in the outcome of graphene synthesis [77]. Before the growth, the substrate needs to be pretreated and annealed at high temperatures to improve substrate characteristics [78]. During the annealing process the introduction of very small quantities of oxygen and H_2 into the chamber can help reduce nucleation sites of the graphene by burning any carbon-containing contaminants and reduce and activate the weakly oxidized Cu surface, respectively [78]. The growth is initiated by introducing hydrocarbon precursor into the chamber that decomposes into active carbon species to fuel the growth of graphene [78]. Usually methane (CH_4) and acetylene (C_2H_2) are the most used hydrocarbons, followed by ethylene (C_2H_4) [71]. The hydrocarbons precursors get adsorbed onto the Cu substrate. After the growth, the temperature of the chamber and as-formed graphene should be reduced to near room temperature to prevent oxidation of graphene [71], [79]. Therefore, the CVD process for graphene growth can be divided into heating the chamber, substrate annealing, graphene growth, and cooling steps. Figure 2 shows in detail the graphene growth process. First, the reactants are transported into the CVD reactor. The gaseous precursor can undergo a reaction to form active species in the vapor phase. These reactant gases then either undergo gas-phase reactions to form intermediate reactants and gaseous by-products via homogeneous reactions or diffuse directly through the boundary layer to the substrate. Then, both are

transported onto the substrate through the surface adsorption. These species would then diffuse on the substrate, collide with each other, and finally overcome the energy barrier to initiate the nucleation, growth and coalescence as well as formation of reaction by-products. Finally, any gaseous products and unreacted species desorb from the surface and are carried away from the reaction zone [71], [78].

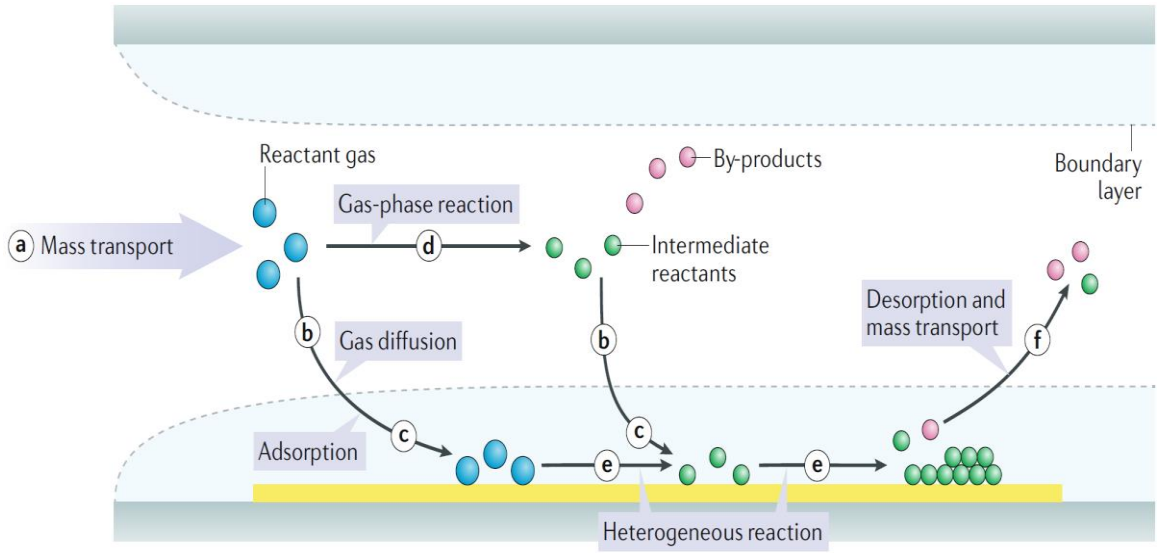


Figure 2: Schematic of general elementary steps of a typical CVD process. Reproduced from [83].

Even though the CVD graphene growth method has received considerable attention for achieving optimal conditions [80], [81], graphene defects may arise during the transfer process, originating either due to the trapped water between the graphene and the target substrate or due to the Cu morphology [82].

Transfer process

The transfer of graphene to multiple substrates is typically done using a wet transfer process that involves the deposition of a polymer, such as polymethyl methacrylate (PMMA), to provide mechanical stabilization for the graphene during transfer, followed by chemical etching of the metal catalyst and subsequent fishing of the graphene-polymer stack with the target substrate, where the polymer will be later dissolved [83]. The wet transfer process used is based on Yoon et al. sample preparation [84], where the CVD-grown graphene on the Cu foil is spin-coated with a PMMA polymer to then proceed to the etching of the metallic catalyst (Figure 3a). Starting with a $FeCl_3$ (Iron(III) chloride) solution to etch the growth substrate, the PMMA/Gr substrate then goes through several intercalated baths (such as deionized (DI) water and hydrochloric acid) to essentially remove any etchant impurities. The CVD-grown graphene is scooped onto the target substrate and dried either at room temperature or by curing at higher temperatures. Because PMMA is only used as a sacrificial and supporting layer, the final step is to remove it (usually in acetone).

In the case of CLs, a similar process was developed at INL where a template was specifically designed to support the CLs when scooping the graphene. This template has a hemispherical radius curvature equal to that of the contact lens (CL) to avoid the appearance of air bubbles when scooping the PMMA/Gr. A hot template is used at 80°C for 45 min to dry the water that stayed trapped between the CLs and the graphene. The removal of the PMMA layer is done by emerging the template CLs in an acetone bath for approximately 1 hour (Figure 3b). The wet transfer is then concluded when the CL is put in a saline solution.

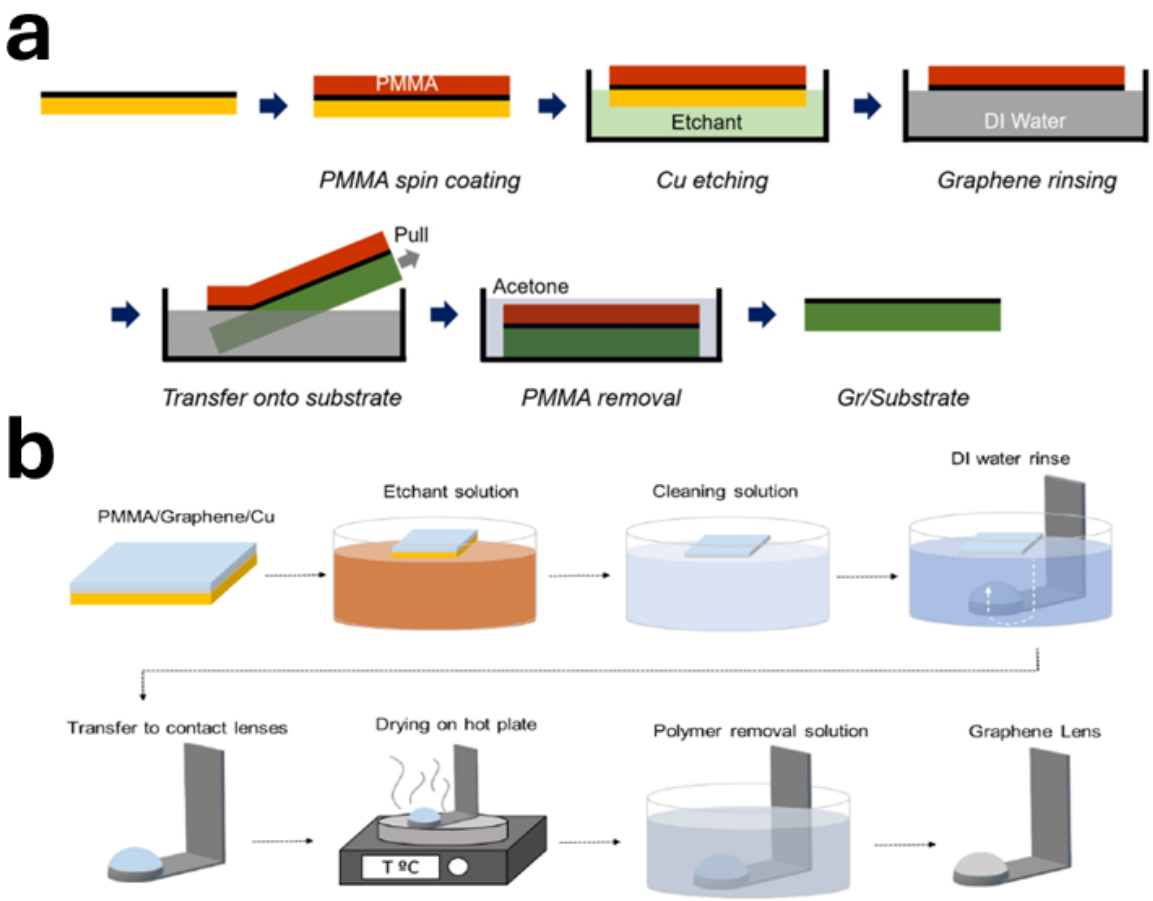


Figure 3: (a) Schematic diagram of the transfer process of CVD-grown graphene on copper foil by wet transfer. Reproduced from [84]. (b) Wet transfer method developed to transfer the CVD-grown graphene to the CLs at INL.

1.2 Graphene field effect transistor technology

Field-effect transistors (FETs) are key components in electronics, most used in digital circuits and amplifiers. The FETs are composed of three metallic conducting electrodes: Source (S), Drain (D) and Gate (G) where the conductive channel connects the S and D. The current between these two electrodes is controlled by the G, by applying an electric field. Traditional FETs use a thin insulating layer (dielectric) between the G and the channel to control conductivity, making them suitable in high-speed, low-power electronic devices [85]. In addition to their importance in computing and communications technologies, FET-based sensors have generated interest in biosensing and chemical detection applications, due to their high sensitivity, and potential for miniaturization. One of the most promising types of FETs is the graphene-based field-effect transistors (GFETs) [85]. Graphene and graphene-related materials have been largely exploited to develop improved chemical and biological electrochemical sensors. This is not only due to the better and unique electrochemical properties of graphene but also to the ease of functionalizing the graphene surfaces with specific elements of interest [64],[86]. These properties make GFETs particularly attractive for biosensing applications, where ultra-sensitive detection of biomolecules is required. Electrolyte-gated transistors (EG-Ts) are very similar to the traditional ones with a key difference, instead of the classical very thin insulating layer (dielectric) which separates the G electrode and the channel, in EG-Ts the G and the channel are in direct contact with an electrolyte. Equally, the conductivity of the channel is modulated by the voltage applied to the gate [87], [88]. EG-Ts are known to be stable in an aqueous environment, operate at low voltages, and can transduce and amplify biological signals into electronic signals, making them important building blocks for enhanced bioelectronics [89], [90], [87], [88]. Graphene has been implemented as the material for the conducting channel, forming electrolyte-gated graphene field-effect transistor (EG-GFET), where the channel will be in direct contact with the electrolyte resulting in a device that outperforms current technologies in terms of their gate sensitivity.

1.2.1 Biosensing

In order to make GFET sensors specific to a target molecule, the graphene surface needs to be functionalized with molecules that are capable of recognizing and capturing target analyte, known as probe molecules Figure 4a. Often the graphene surface is not completely covered with the probe molecules and to inhibit non-specific interactions that could lead to false results, passivation strategies

are employed [91]. Biorecognition events causing changes in membrane integrity can be electrically monitored using functionalized EG-GFETs [92], but the high expectations for GFETs are still to be met because they are primarily sensitive to the charges carried by the biomolecules adsorbed on the graphene surface, which suffers from the ionic screening due to mobile ions present in the solution, known as the Debye screening effect [93]. In electrolytes, this screening effect is characterized by the Debye length (λ_D). The λ_D is characterized by the net electrostatic effect in the analyte and how far its electrostatic effect persists, in other words, it is the thickness of the electrical double layer (EDL) (Figure 4b). Having a critical effect on the overall performance of the sensor [48], [94]. When the analyte is drop-casted into the channel to serve as a medium of detection, the application of a Gate voltage will cause the formation of an EDL on the graphene channel, which consists of two parallel layers of opposite charge that act like a capacitor due to their approximation, significantly increasing the capacitance and transconductance of the device. Depending on the doping of the graphene the first layer will consist of positive ions if the graphene is n-doped and negative ions if p-doped. The second layer is roughly associated with the channel. The changes in ionic concentration or charge distribution within the electrolyte, confined to the Debye screening length, are effectively transduced to the graphene channel by modeling its capacitance [25], [95], [96], [97]. This is the reason why EG-FETs are very sensitive to changes in the environment and this intimate correlation with the environment around its surface, means that changes in the pH solution/analyte and proteins attached to the surface can all have an immediate impact on the channel conductance [98].

The mode of operation of a GFET when sensing target molecules can be understood by two main characteristics, the transfer curves and the change in transconductance. By fixing a bias between the drain and the source (Vds), transfer curves can be obtained by sweeping the gate voltage Vg. This results in a plot where the current is plotted as a function of the gate bias, typically with a V-shaped curve, as illustrated in Figure 4c [62]. This shape translates an exchange in the polarity of the majority charge carriers in the graphene layer when sweeping the gate voltage: the left branch (or p-branch) represents an increasing density of positive charge carriers (holes), while the right branch (or n-branch) represents negative charge carriers (electrons) [62], [99]. This occurs because, unlike silicon transistors and other semiconductors with a bandgap greater than zero, which exist in two different states (p-type and n-type), in the case of graphene, the same transistor can function as both p-type and n-type [62], [99]. The appearance of a minimum value for the current is noticeable, where both positive and negative carriers have equal populations. This point between the two branches is known as the Charge Neutrality Point,

also referred as Dirac Point [62]. Transconductances for holes (g_m(h)) and electrons (g_m(e)) are not necessarily the same, in which case the transfer curve is asymmetrical [62]. The interaction between biological targets and biorecognition elements at the surface of graphene can alter the doping state of graphene by altering the electric field and thus creating a shift in the Dirac point from its initial value [62]. The polarity represents the direction of the change on the voltage axis: p-doping when the Dirac Point shifts to more positive voltage, n-doping when it shifts to more negative voltage [62]. This change is proportional to the concentration of analyte molecules in the liquid.

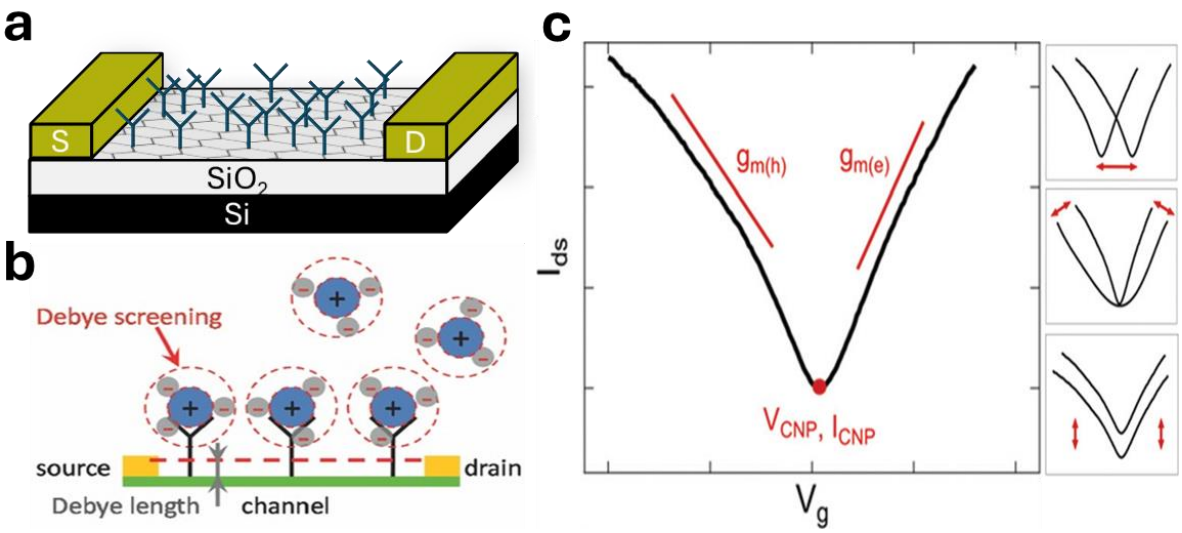


Figure 4: (a) Functionalized GFET with bio-recognition elements. (b) Schematic of the Debye screening effect makes biomolecules carry zero net charge due to the Debye screening effect of ions in electrolyte. Reproduced from [94]. (c) Typical transfer curve I_{ds} (V_g) of a GFET, illustrating key metrics in its use as a sensor. Smaller graphs, from top to bottom represent the change in the voltage of the charge neutrality point V_{CNP}, change in the transconductance of electrons g_m(e) or holes g_m(h), and change in the current amplitude, including at the charge neutrality point I_{CNP}. Reproduced from [62].

The graphene functionalization can be either by covalent binding of probe molecules, which are known to alter the graphene electrical properties while having high stability on the graphene surface enabling repeatability or by non-covalent binding, where the most used linker molecule is 1-pyrene butanoic acid succinimidyl ester (PBASE) due to the molecule having an aromatic pyrene group that non-covalently binds graphene without changing the channel electronic properties [62], which is important for the fabrication of high-sensitivity sensors. The graphene can then be functionalized with antibodies [100], [101], DNA[26], [102], [103], and proteins [104]. Fernandes et al. successfully functionalized an EG-GFET device utilizing PBSE for the detection of Matrix Metalloproteinase 9, overcoming the hydrophobicity of graphene that hinders the immobilization of antibodies [100]. A back-gated EG-GFET was functionalized

with antibodies to detect exosomes successfully for the first time, achieving a high sensitivity to low concentrations of at least 0.1 μg/mL [101]. DNA hybridization detection has also been achieved, where the current in the graphene channel significantly changes with the full complementary DNA attaching to the DNA aptamer while the non-complementary DNA causes insignificant changes [102], making it possible to detect a concentration of the DNA hybridization as low as 25 aM (10^{-18}) [103]. Dopamine (DA), a neurotransmitter which is related to Parkinson's disease was reported to be detected utilizing multiple graphene transistors in an array configuration allowing the independent and simultaneous detection in the same sample in concentrations as low as 1 aM [26]. GFETs has also been used to studied for glucose detection, primarily through the functionalization of the graphene channel with GOx. Early studies utilizing these systems for glucose detection were able to achieve limit of detection down to the 0.1 mM [105]. For instance, different techniques were introduced to achieve lower LODs, resulting in highly sensitive glucose sensors, going as low as the μM concentrations [106], [107].

1.3 Graphene-based contact lens technology

In this section, graphene-based technology embedded into CLs will be discussed as well as its potential in different types of applications where the simple introduction of graphene can improve its properties. The properties and possibilities of CLs have been explored in several ways, from the detection of physical and chemical biomarkers on eye, such as intraocular pressure and glucose. Since the first graphene-coated lens was achieved, and some beneficial properties such as environmental electromagnetic shielding and dehydration protection effect was obtained, the integration of graphene for different applications would allow the dispose of materials used to build sensors on the CLs that would change its properties and even obstruct clear vision [108]. For example, graphene was utilized in an adaptive lens to correct presbyopia as a conductive coating. This adaptive lens exhibited fast response time of an electrical signal that provides a continuous change in the effective refractive index of the lens, changing the lens power and allowing the user to focus on nearby objects, thereby replicating the accommodation mechanism of the younger eye [109]. Furthermore, the addition of graphene derivatives to the CLs has been reported to enhance the physical and anti-bacterial properties while also improving the oxygen permeability [110]. Other applications were shown when using graphene electrodes for conformal, full cornea recording of ERG, exhibiting a superior solution compared to current methods used for measuring electrical potential on the corneal surface since these are usually related to discomfort due to direct

contact with a rigid CL [111]. The potential use of CLs as a drug delivery transport system represents an innovative and promising approach in the field of ophthalmic drug administration as different studies showed that GO not only enhanced drug-loading capacity and improved the mechanical properties of the CL but also increased the release time of the drug offering an effective method to treat different types of diseases [112], [113].

1.3.1 Biosensing

The development of CL-based sensors technology has gained traction in the past decade largely due to advances in the miniaturization of electrical circuits and the identification of relevant biomarkers in the tear and the eye. The eye provides information through physical biomarkers such as the intraocular pressure (IOP). Elevated IOP can lead to glaucoma, a disease that changes the curvature of the cornea and can lead to the progressive degeneration of the optic nerve which can end in blindness [114]. The current method to measure IOP often leads to misleading clinic diagnoses, making it important to find an alternative, being the ultimate objective of achieving real-time monitoring to mitigate the consequences of high IOP [115]. Several studies have proposed the application of graphene as a resistive sensor that could be integrated into CLs. The working principle consists of detecting the curvature change on the cornea by monitoring the resistance of the graphene sensors that change if the CL is stretched. Liu et al, proposed a "fish scale" microstructure on a PDMS substrate, a biocompatible material used to form CLs. Using this structure, a Wheatstone bridge was developed exhibiting a sensibility of 3.166 mV/mmHg and good linearity [116]. Xu et al, was able to achieve a higher sensitivity of 150 μV/mmHg, also using a graphene-based Wheatstone bridge [117]. The major throwback in both these studies is that wires were used to connect the CLs to an external processing chip and only then wireless communication was made. Integration of the processing chip into the CL is necessary to avoid affecting the wearer's movements and day-to-day life [116], [117]. Zhan et al. proposed a different structure for the detection of IOP. Graphene in a woven fabric (GWF) arrangement mounted on the outside of the lens. Changes in the cornea curvature forms cracks on the GWF and thus increase resistance. This structure was shown to have "healing" properties enabling the constant formation and mending of these cracks enabling the continuous monitoring of IOP (Figure 5d) [118].

As tears are a more accessible and less complex body fluid (than serum or plasma) and sampling is much less invasive, research is starting to focus on how disease processes affect the tear film

composition. It has been observed that the presence of abnormal metabolic molecules in tears arises from dysregulation in metabolic pathways. By determining the compositional changes these cause in the tear profile, pathways in disease progression may be identified, allowing for more predictive and personalized therapy of the individual. Several studies have reported finding several biomarkers related to breast cancer, diabetes, Alzheimer, dry eye syndrome and nerve injury present on the tear film [119], [120], [121], [122], [123], [124]. The eyes are one of the most important sources of clinical information in the human body. The close relation between tears and blood generates the presence of multiple chemical biomarkers that can be tracked to diagnose and prevent severe diseases. A biomarker present on the tear film is cortisol, a molecule that reflects stress or inflammation. A graphene channel on a FET was chemically bonded with anti-bodies (C-Mab) and integrated onto a CL with an electrical circuit capable of achieving wireless communication. The sensor enabled a detection of a concentration of 10 pg/ml, that is low enough compared with the quantity of cortisol found in the tear film [125]. Similar to tracking biomarkers to manage illnesses, continuous neurotransmitter detection in tears such as dopamine (DA), that are related to neurodegenerative diseases, can provide indicators that can help anticipate future symptoms [37]. A biosensing electrode was prepared from PEDOT functionalized with sulfur-doped graphene (PEDOT-G) and the tyrosinase and poly (3,4 ethylene dioxythiophene) enzyme in order to understand the relation between DA and myopia. A limit of detection was achieved for concentrations of 101 nM. Further tests showed the existence of a correlation between DA and myopia diopters, supporting the underlying relationship between the DA concentration in tears and the negative diopters [126].

One of the most prominent molecules in the tear film is glucose. Several strategies have been developed to fabricate a non-invasive method using CLs, for example, an early study showed the fabrication of an electrode formed on a thin PDMS membrane that was functionalized with GOx and was supported by a soft CL [127]. This study did not use graphene but showed the possibility of monitoring glucose changes in the tear film using a wired line connected to the flexible electrode causing minimal irritation to the eye [127]. CVD-grown graphene has shown potential different types of bio-applications [128], [129] being its integration to CLs no different. A study tested a LED as a visual indication for glucose sensing. An antenna, two electrodes, and a functionalized graphene channel compose the resistive glucose sensor that was integrated with the LED onto the CLs (Figure 5a) [130]. The circuit's working concept is that when the sensor is exposed to tear fluid with a glucose concentration over a certain threshold (0.9 mM), the sensor's resistance decreases, which causes the LED's parallel circuit to become less resistant and eventually switch off [130]. Another study used a hybrid structure comprising graphene and silver nanowire was

created, and it was utilized as the electrodes of a GFET. The graphene channel was functionalized with GOx. The CL's integrated electronic circuitry included an antenna coil (Figure 5b) achieving detection of 1 μM of glucose [131]. Wireless operation was achieved by coupling the sensor with an external antenna as shown in Figure 5c [131].

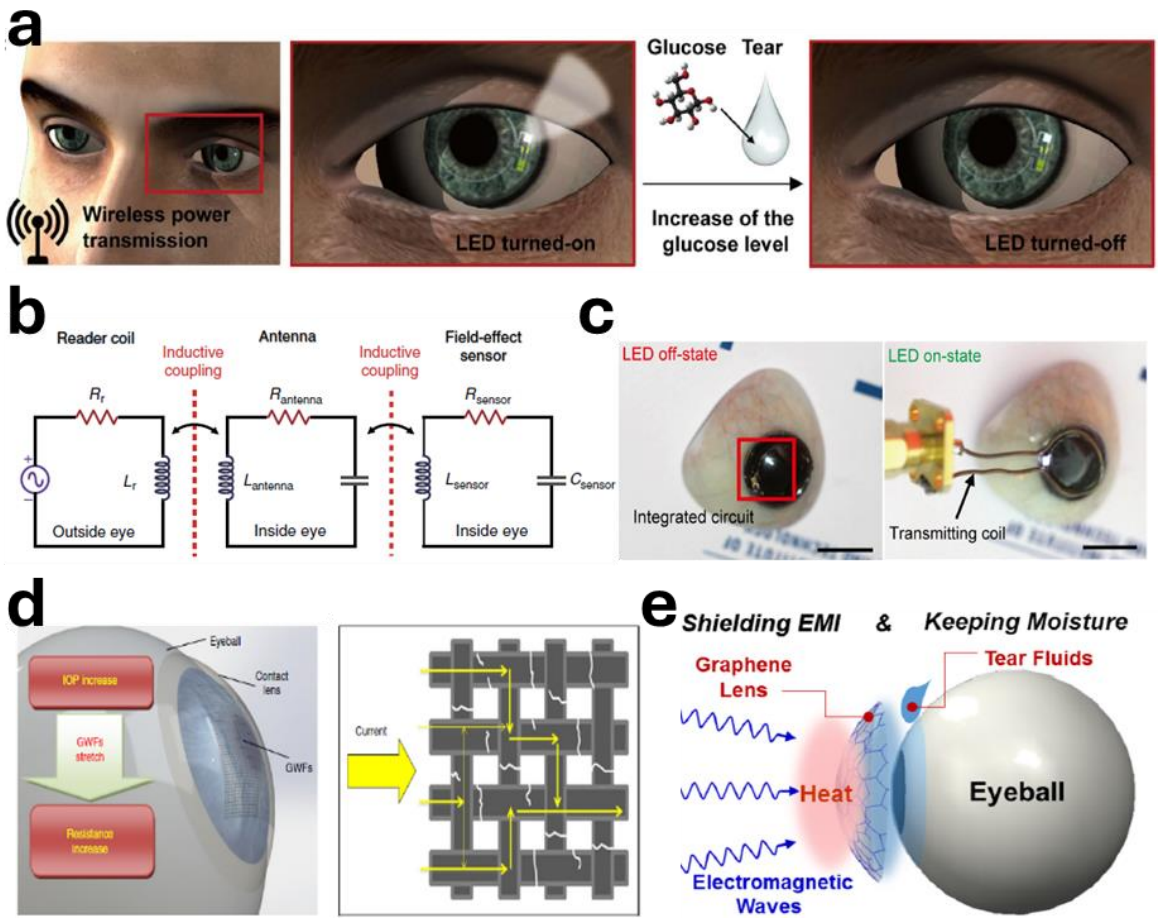


Figure 5: (a) Operation of the soft, smart CL. Reproduced from [130]. (b) Photographs (left, off-state; right, on-state) of operating wireless display with lens shape located on the artificial eye. Scale bars, 1 cm. Reproduced from [131]. (c) Schematic of the reading circuit for wireless sensing on CLs. Reproduced from [131]. (d) Working principle of the device and current pathway through a fractured graphene woven fabric. Reproduced from [118]. (e) Graphene as a shielding layer against EM waves and dehydration protection. Reproduced from [132].

Ideally, the integration of a sensing device would be accompanied by a wireless circuit system to transmit data in real-time and have continuous monitoring. Although electrical circuits have been successfully integrated into CLs, a reliable method to wirelessly power these circuits has yet to be established. In most cases, it is necessity to use wires, opposing as a major drawback as it can lead to discomfort from the patient and potentially promote air bubbles between the CL and the cornea [133]. As graphene has

attracted a lot of attention for its suitable characteristics in the optical, mechanical, and electrical fields, researchers think of it as the perfect candidate to fabricate these sensing systems that could be embedded to the CLs [134]. In particular, graphene-based sensors, such as electrolyte-gated graphene field-effect transistors (EG-GFETs), have shown notable improvements compared to conventional sensors which the circuits integrated into the CLs could benefit from.

2. MATERIALS AND METHODS

In this chapter, we define all the techniques used to fabricate the materials and devices in this work. Firstly, graphene growth and its transfer to different substrates. Surface functionalization of the graphene on electrolyte-gated field-effect transistors, bare Si/SiO_2 substrates and contact lenses is also described.

2.1 Graphene production

Monolayer graphene growth was performed in an EasyTube ET3000 chemical vapor deposition (CVD) system (CVD Corp, USA). Graphene was grown on copper (Cu) foils/substrates that act as catalysts. The 5×5 cm^2 Cu foils (99.99+% purity) were initially chemically treated in a solution of $FeCl_3$, HCl, and DI water for 1 min under ultrasound to reduce rugosities and organic contamination and then heated on a hot plate at 250°C in air for 20 min for partial oxidation. The oxidized Cu foils were placed into a three-zone quartz tube furnace, and the chamber was evacuated to approximately 10 mTorr and then filled with 250 sccm argon (Ar, 99.999 % purity) and 170 sccm hydrogen (H, 99.999 % purity) gas mixtures. Once the growth temperature and pressure were reached, 1.25 sccm CH_4, the carbon precursor, was introduced into the chamber. Monolayer graphene growth was carried out at 1040°C and 6 Torr for 1 h on both sides of the Cu foil.

2.1.1 Transfer

Graphene was transferred via an optimized poly(methyl methacrylate) (PMMA) solution designed to provide mechanical support during the transfer cycles while suppressing potential contamination [135]. The optimized PMMA is a mixture of PMMA-550k (550,000 average molecular weight) and PMMA-15k (15,000 average molecular weight) in anisole at a 2:1 ratio (3 wt. %). PMMA was spin-coated (3000 rpm, 30 s) on the top side of the graphene/Cu/graphene, followed by drying in a fume hood at room temperature (RT) overnight. Plasma ashing (PVA TePla GiGAbatch, O_2: Ar 1:1, 0.75 mbar, 230 W, 25°C, 2 min) was performed to remove graphene from the back side of the sample. To dissolve the Cu, the sample was floated in a 0.5 M $FeCl_3$ solution for 2 h. After full etching, the graphene/PMMA membrane was rinsed in cycles of DI water and 2% HCl solution baths for 30 min to remove etchant impurities. Finally, the graphene/PMMA was rinsed in DI water two times and transferred to the target substrate. For the CL a dedicated holder was designed in AutoCAD (AutoDesk) and printed with a stereolithography

(SLA) 3D printer (3D printer SLA – Formlabs Form 2). SLA 3D printing uses a laser to cure solid isotropic parts from a liquid photopolymer resin. The resin used for the fabrication of the 3D-printed template was grey resin (Ponto Z). The full transfer process is illustrated in Figure 3b.

2.1.2 Functionalization

The functionalization process of EG-GFETs followed the general procedure developed in [136], requiring four fundamental steps. Between every functionalization step, the chips were thoroughly cleaned with Milli-Q water, dried with N_2 flow and measured with undiluted phosphate buffer saline (1 x PBS, pH = 7.4). 1 x PBS was prepared by diluting two tablets in 400 mL of Milli-Q water. 1) Au gates were passivated with DDT (2 mM in ethanol), a gold blocking agent, for 2 h. Every 30 minutes, 40 µL were applied to the chips due to ethanol evaporation; 2) 40 µL of PBASE (10 mM in dimethyl sulfoxide; DMSO), a hetero-bifunctional linker binding graphene and GOx, were put on the chips for 2 h in a humid chamber. 3) A solution of GOx (10 mg/mL in Milli-Q water) was applied in 40 µL and incubated overnight (~ 16 h), in a humid chamber, to link to PBASE. iv) 40 µL of ETA was dropped on the chips and incubated for 30 min. To confirm that GOx was correctly immobilized on graphene, we performed a robust characterization of the steps 2) and 3) of the functionalization process on separate graphene samples transferred onto Si/SiO_2 unpatterned substrates. To prepare D-(+)-glucose, ascorbic acid, lactic acid (lactate) and H_2O_2 concentrations, stock solutions of 1 mM of each analyte were prepared and diluted in 1 x PBS. To prove the inactivation of GOx by H_2O_2, 40 µL of 1 mM of H_2O_2 was added to the Gr/PBASE/GOx/ETA device and left in contact for 10 min. Afterwards, the chip was thoroughly cleaned with 1 x PBS. For the selectivity test with the artificial tear, glucose concentrations were prepared directly in the artificial tear medium. A dedicated support was designed to support the CLs during the transfer and functionalization process in AutoCAD (AutoDesk) and printed with a stereolithography (SLA) 3D printer (3D printer SLA – Formlabs Form 2). SLA 3D printing uses a laser to cure solid isotropic parts from a liquid photopolymer resin. The resin used for the fabrication of the 3D-printed template was grey resin (Ponto Z). The functionalization process of the graphene-coated lenses followed a similar approach to the one done on the EG-GFETs. H_2O_2 was used to prove the activity of the enzyme. The full transfer process is illustrated in Figure 36c-e.

3. CHARACTERIZATION TECHNIQUES

In this chapter, the techniques used for the characterization of the fabricated materials and devices are described. The analyses were conducted using techniques such as optical microscopy, water contact angle, Raman spectroscopy, X-ray Photoelectron Spectroscopy, Scanning electron microscopy, Ultraviolet-visible spectroscopy and field effect transistor measurements. These techniques provided useful information about the CVD-grown graphene intrinsic characteristics, such as its quality, number of layers, continuity and electrical changes caused by the different experiments carried out throughout this work and help better understand the glucose sensing mechanisms.

3.1 Optical microscopy

The optical microscope (OM) is the oldest technique of microscopy with its concept being born more than 2000 years ago, when it was discovered that it was possible to amplify a small object utilizing a spherical-shaped transparent 'lens' [137]. This fundamental idea has developed over time, leading to the emergence of more sophisticated OM. This technique utilizes visible light and a system of lenses to magnify and resolve structures at the microscopic level. The resulting magnified image can be either observed by eye or by live view and capture. The latter uses software that provides a live view of the sample, allowing for real-time observation. OM is one of the simplest tools to examine 2D (Two-dimensional) materials. For example, this method can give information about contamination and homogeneity of the CVD graphene. It's easy to see wrinkles, holes, and cracks that occur during growth and transfer. It's also possible to distinguish if graphene is multi-layered or monolayer through the contrast difference. In this work, images were acquired using a Motic PSM-1000 microscope with 3 lenses (10x, 50x and 100x) and a mechanical stage (Figure 6). The digital images were acquired with a Moticam 5+ and the Motic Images Plus application software.



Figure 6: Optical microscope used at INL facilities.

3.2 Scanning electron microscopy

Scanning Electron Microscopy (SEM) is a powerful non-destructive technique that utilizes a focused beam of electrons to scan the surface of a sample, achieving resolutions down to the nanometer scale. When the electron beam interacts with the sample, it generates various signals, including secondary electrons, backscattered electrons, and characteristic X-rays, which are analyzed. These signals are then detected and provide valuable information about the material's topography, morphology, and composition. One challenge faced when using SEM is the potential overcharge of the surface if the sample is not electrically conductive, which can lead to image distortion and potential damage. To avoid this happening, usually a thin layer/tape of conductive material is used. SEM can acquire high-resolution images with magnifications from ~10x to over 200,000x. This level of detail is not possible to obtain when using the conventional optical microscope. Figure 7 shows the SEM available at the INL facilities, which was used in this study to examine the morphology and integrity of graphene layers on contact lenses.

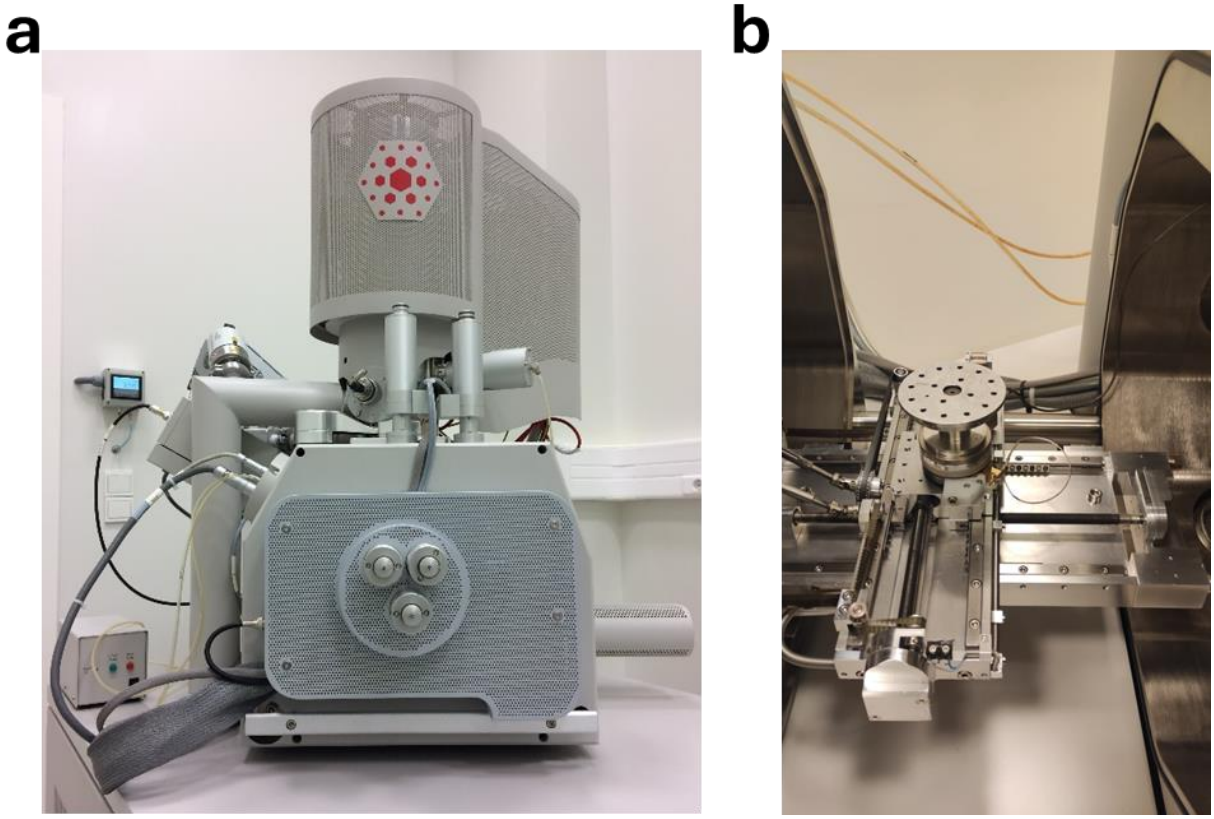


Figure 7: (a) SEM at INL facilities. (b) Close up photograph of the stage.

3.3 Raman spectroscopy

Raman spectroscopy is a non-destructive technique capable of measuring the vibrational energy modes of a sample using scattered light. This technique takes advantage of molecular vibrations to provide valuable information about the chemical and structural composition of each molecule. These molecular vibrations, caused by the movements of its individual atoms, are highly sensitive to the exact structure of the molecule. This results in a unique vibrational spectrum, often referred to as the molecule's "fingerprint" [138]. In Raman spectroscopy, a sample is irradiated with a laser of a single frequency. The interaction between the laser and the molecules causes the light to be scattered, where three possible outcomes can occur (Figure 8a). The most common result that takes place during scattering events is known as Rayleigh or elastic scattering, where the energy of the molecule is conserved, and the energy and wavelength of the scattered photon remains the same. The other outcome that can happen is inelastic scattering, although not as common can still occur and is the basis for Raman scattering. If the molecule gains energy from the photon during the scattering (excited to a higher

vibrational state) then the scattered photon loses energy, increasing its wavelength. This occurrence is called Stokes Raman scattering. Inversely, if the molecule loses energy by relaxing to a lower vibrational state the scattered photon gains the corresponding energy and its wavelength decreases, is called Anti-Stokes Raman scattering (Figure 8b) [138].

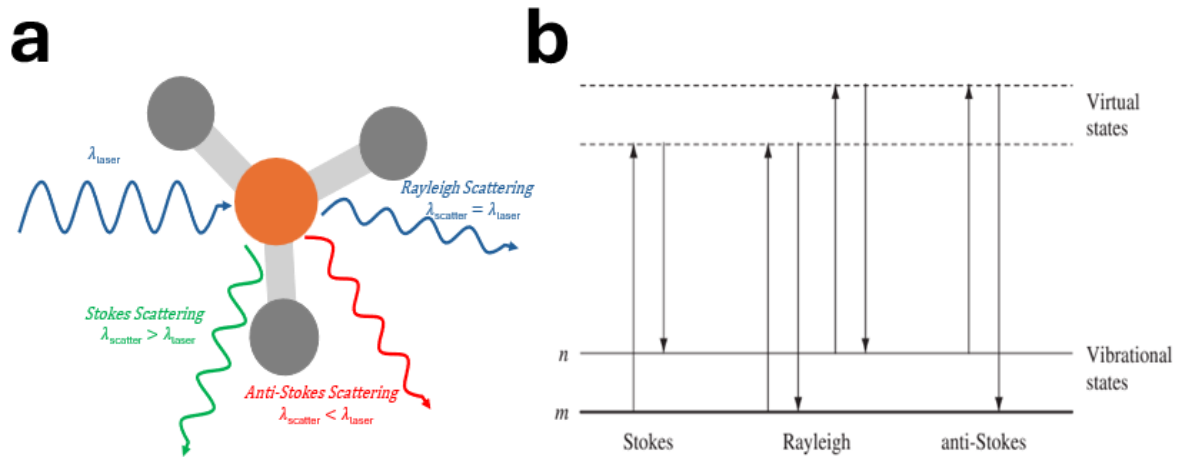


Figure 8: (a) Three types of scattering processes that can occur when light interacts with a molecule. (b) Diagram of the Rayleigh and Raman scattering processes. Reproduced from [138].

It is a powerful technique for characterizing sp^2- and sp^3-hybridized carbon allotropes with high resolution, enabling the identification and detailed analysis of all members of the carbon family [63], [139]. This is important as all sorts of carbon species can occur, in other words, unwanted by-products and structural damage can appear when synthesizing graphene [139]. Thus, allowing a further characterization of the CVD-grown graphene to a deeper level. Any variation of electronic properties due to defects, edges, doping or magnetic fields affects the positions, widths, and intensities of the Raman peaks, which are divided into two fundamentally different sets of peaks, the D, G, 2D and modes due to the in-plane vibrations (Figure 9a) [140]. The D peak (1350 cm^{-1}) is known as the disorder band and its intensity is directly proportional to the number of defects [141]. It is a resonant band that exhibits dispersive behavior, which means that there are several very weak modes underlying this band and the choice of excitation laser used will enhance different modes, which could lead to different positions and shape depending on the laser frequency used. Monitoring the 2D peak (2700 cm^{-1}), a result of the two-phonon lattice vibrational process and the G peak (1580 cm^{-1}) which arises from the in-plane vibration of *sp2* carbon bonds, enables the characterization of the structural and electronic properties of graphene [142]. By comparing the intensities of both peaks, I(2D)/I(G) is possible to estimate the number graphene of layers, with a high ratio indicating monolayer (Figure 9b). Both these peaks are sensitive to doping and structural changes

which means that there will be changes in its position and full width half maximum (FWHM) when under different conditions [143].

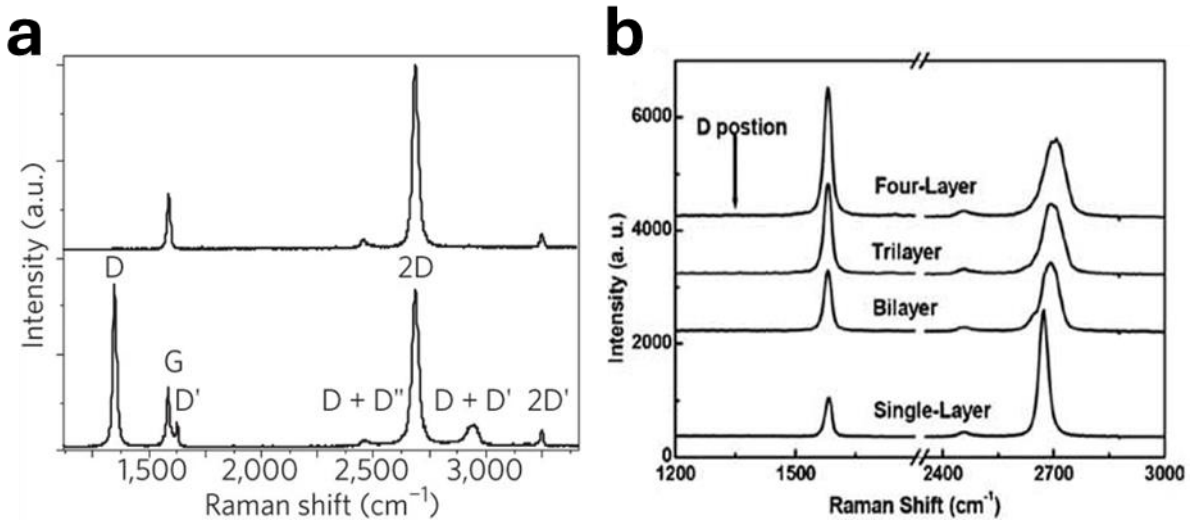


Figure 9: (a) Raman spectra of pristine (top) and defected (bottom) graphene. Reproduced from [140]. (b) Raman spectra of graphene with different number of layers. Reproduced from [143].

Measurements were performed with an ALPHA300 R confocal Raman microscope (WITec) (Figure 10) using 532 nm laser light for excitation at room temperature. The laser beam was focused on the sample with 50x (NA = 0.7) and 100x (NA = 0.9 DIC) lenses (Zeiss). Single acquisitions and large-area scans were performed using a 600 grooves/mm grating with 3 mW laser power. Raman data analysis was performed with Project FIVE+ software (WITec).

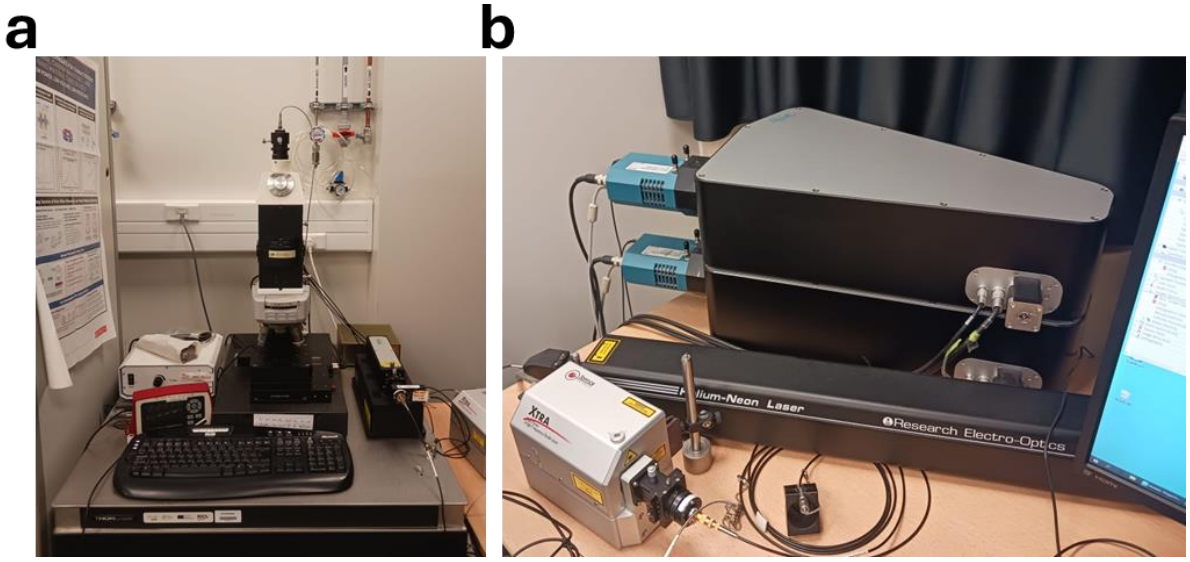


Figure 10: Raman confocal microscope at INL's facilities. (a) Microscope and fiber optic Raman probe. (b) CCD detectors and laser excitation source.

3.4 X-ray photoelectron spectroscopy

X-ray photoelectron spectroscopy (XPS) is a relatively recent technique known for its high sensitivity for chemical analysis. Surface analysis by XPS involves irradiating a solid in vacuo with monoenergetic soft x-rays and analyzing the emitted electrons by energy. These photons have limited penetrating power meaning that they interact with atoms in the surface region of the sample, the reason it is a surface sensitive technique. As a result of this interaction, electrons are emitted by the photoelectric effect and the kinetic energy that remains on the emitted electron is the quantity measured by converting it to binding energy using the spectrometer work function. The spectrum is obtained as a plot of the number of detected electrons per energy interval versus their binding energy. Figure 11a shows the different binding energies of carbon species and Figure 11b a spectrum of a carbon atom in the 1s region. Since there are a variety of possible final states of the ions from each type of atom, there is a corresponding variety of kinetic energies of the emitted electrons. As a result, each element has a unique set of binding energies making, XPS a valuable technique for identifying elements and determining their surface concentrations. Variations in the elemental binding energies (the chemical shifts) arise from differences in the chemical potential and polarizability of compounds. These chemical shifts can be used to identify the chemical state of the materials being analyzed [144].

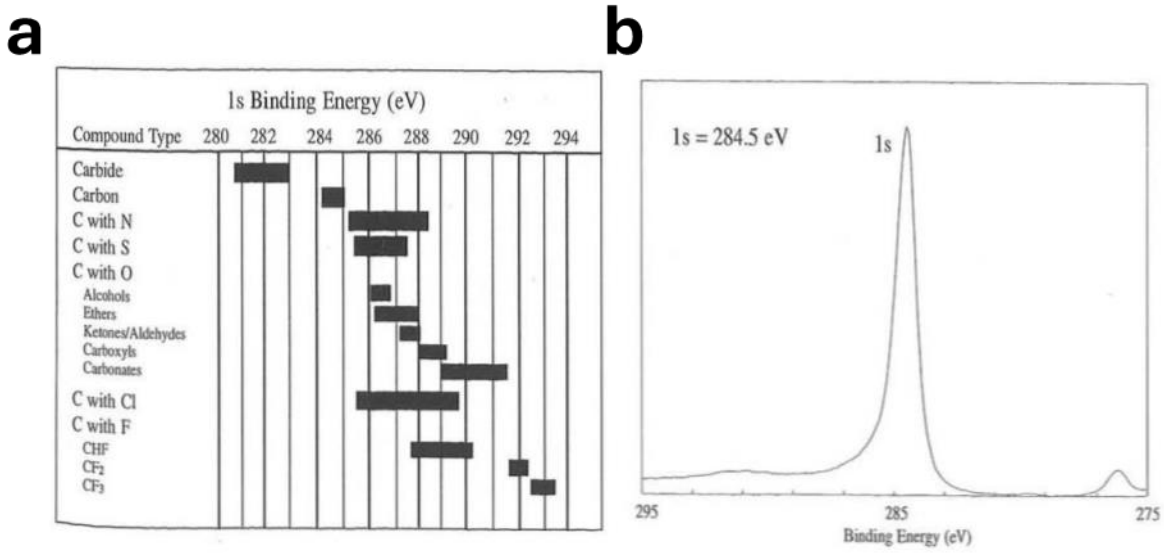


Figure 11: XPS analysis shows the binding energies of carbon species. (a) A table of C 1s binding energy ranges for various carbon compounds. (b) XPS spectrum on the C 1s region, with a prominent peak at 284.5 eV, corresponding to sp^2-hybridized carbon. Reproduced from [144].

XPS spectra were acquired with an ESCALAB 250 XI (Thermo Fisher Scientific, Source: Al Kα 1486.6 eV, 650 μm spot size, Source Power: 300 W, Pass energy: 160 eV – survey; 10 eV – high resolution) system with an analysis chamber maintained in ultrahigh vacuum (UHV ~ 5×10^{-10} mbar) conditions where the functionalized monolayer graphene on the 2x2 cm^2 Si/SiO_2 substrates was placed. The spectra were referenced to the graphene C–C bonds at 284.5 eV. The spectra were analyzed with CasaXPS software (Casa Software Ltd., version 2.3.25) [145], and the residual background was eliminated via the Shirley method across the binding energy range of the peaks of interest.

3.5 Ultraviolet-visible spectroscopy

Ultraviolet-visible (UV-vis) spectroscopy is an analytical technique used to measure the light absorbed or transmitted through a sample in either liquid or solid state using a reference. This technique measures the intensity of light in the ultraviolet (UV, 10nm - 400nm) and visible (vis, 400nm - 800nm) of the electromagnetic spectrum. The resulting absorbance spectrum depends on the chemical composition of the sample being analyzed, with peaks corresponding to electronic transitions. According to the Beer-Lambert law, absorbance is directly proportional to the concentration of the absorbing species, path length, and molar absorptivity, allowing for quantitative analysis of the sample. Electronic energy levels consist of multiple vibrational energy levels, each of which further contain several rotational energy levels. When a photon interacts with a molecule, it can induce a transition between electronic energy levels if its energy matches the required energy difference. The resulting absorption of radiation is measured and plotted against the electromagnetic wavelength to generate the spectrum. UV-vis measurements were performed on a Shimadzu UV-Vis spectrophotometer, which allows the measurement of spectra of light absorption with wavelengths ranging from 200 nm to 900 nm for liquid samples (Figure 12a). The liquid samples were placed on dedicated cuvettes (Thor Labs) which were illuminated for the acquisition of the absorbance vs wavelength spectrums. For the solid samples, the measurements were performed on a PerkinElmer LAMBDA 950 UV-VIS-NIR spectrophotometer (Figure 12b). The samples were measured with the help of a support.

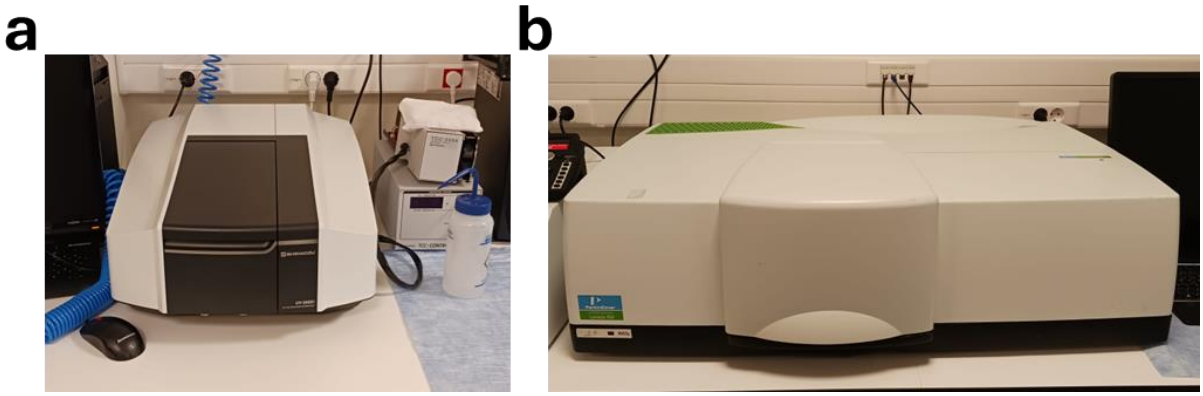


Figure 12: System used for (a) liquid samples and (b) solid samples at INL facilities.

3.6 Contact angle measurements

Water Contact Angle (WCA) measurements are usually used to estimate the wettability of a given surface. A droplet forms a semi-spherical shape on top of a solid substrate when it is dropped onto it due to surface tension in the liquid and the liquid's attraction to the surface. The angle created at the point of contact between a tangent to the liquid surface and the solid surface is known as the contact angle. Usually, the WCA measurements are classified into two main categories: hydrophobic surface, defined as when the WCA is around 90° and above, or hydrophilic surface when the WCA produced is low. These two categories are related to low surface energy and high surface energy, respectively [146], [147].

In the case of graphene, there have been several studies evaluating its wettability [148]. The results have led to a divergence of opinions within the community where some researchers claim that pristine graphene is hydrophilic [149], [150] while others claim it to be hydrophobic [151], [152]. These results had the community consider the possible effect of the substrates having some sort of impact on the WCA. Some claimed that the single-layer graphene had complete dependence on the substrate and the increased number of layers leads towards bulk graphite WCA values [153]. Later the "wetting translucency" term was introduced to characterize the partial effect that the substrate was shown to have on graphene [154]. It was believed that about 30% of the van der Waals interactions between the water and the substrate was transmitted through the graphene layer, acting as a translucent barrier [154]. The absence of this transparency was also considered, and the wettability was attributed to the dimensionality of graphene that could result in a variety of interfacial phenomena that influence the material's apparent wettability [148], these include the possible unwanted doping of graphene, sample preparation methods

and measurement procedures that can modify the graphene hydrophilicity [155], and possible contamination of the sample due to exposure to ambient air [148], [156]. A study reported that airborne hydrocarbons must be considered when measuring the WCA of graphene as they get adsorbed on graphitic surfaces resulting in a more hydrophobic surface [156]. However, it was shown that this contamination was shown to be partially reversible by thermal annealing and controlled ultraviolet–O3 treatment [156]. Nevertheless, graphene wettability is related to the Fermi level, and it can be tuned either through chemical or electrical doping. Moving the Fermi level away from the Dirac point showed better hydrophilicity either by p-doping or n-doping (Figure 13) [157], [158].

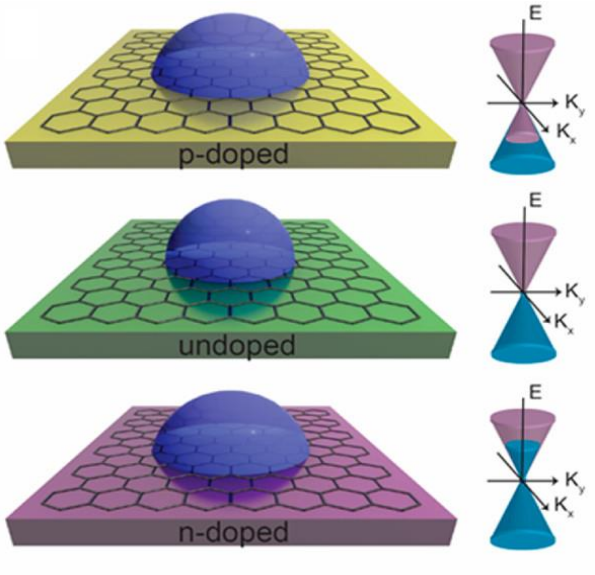


Figure 13: Schematic illustrations show graphene wettability modulation by doping-induced Fermi level shifts. Reproduced from [158].

Static wetting angle measurements were conducted with a drop shape analysis-contact angle (DSA-CA) system (Figure 14) using DI water as the liquid medium to characterize each functionalization stage. A 3 µL water droplet was deposited on the surface of the sample at a dosing rate of 600 µL/min, and the water contact angle (WCA) was calculated. All the measurements were carried out in air at room temperature. For each analysis, a minimum of 10 measurements were performed, and the average was calculated. Droplet profiles were automatically detected and analyzed by fitting to the Young–Laplace equation in DSA3® software (Kruss).

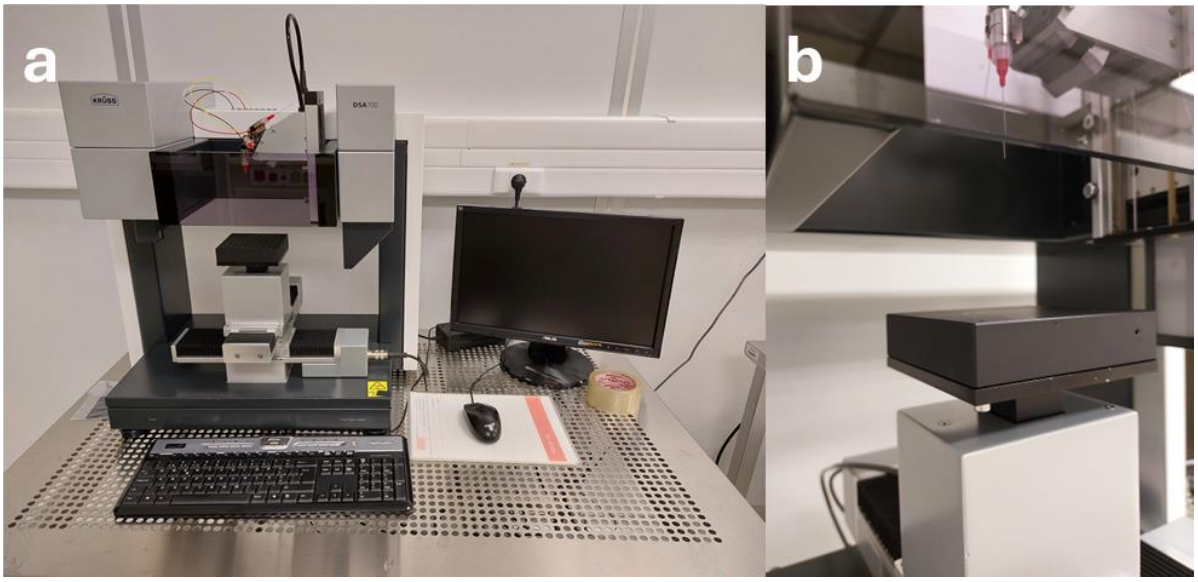


Figure 14: Water contact angle at INL's cleanroom. (a) Water Contact Angle setup. (b) Close up photograph of the stage and DI water syringe of the setup.

3.7 Field effect transistor measurements

A signal acquisition platform connected the PCB with the wire-bonded chips to the computer interface and traced the EG-GFET transfer curves. The in-house developed electronic platform has a microcontroller that controls the digital-to-analog converter (DAC), one regulated voltage source generating the gate voltage sweeps (V_{GS}), and another source that applies a constant source-drain voltage (V_{DS}) between the source and drain contacts of each device. The source-drain current (I_{DS}) is converted into a voltage by an analog-to-digital converter (ADC) before the digital data is sent to the computer via a USB connection. The transfer curve of each EG–GFET was measured after each functionalization process step by applying a V_{DS} = 15 mV and measuring I_{DS} in 500 V_{GS} steps between -0.3 and 0.7 V. The signal is the shift of the minimum conductance point, equated to the Dirac point (ΔV_{DIRAC}), relative to the baseline for each analyte concentration.

4. GLUCOSE SENSING VIA ELECTROLYTE-GATED GRAPHENE FIELD-EFFECT TRANSISTOR

In this chapter, we investigate the glucose sensing mechanism in electrolyte-gated graphene field-effect transistor sensors. The sensors were fabricated in INL's cleanroom by advanced photolithography processes. The graphene channel was functionalized for glucose sensing. After each step, we used Raman and XPS spectroscopies to verify the immobilization of glucose oxidase onto graphene. Following this characterization, the glucose sensing mechanism was explained and proved with different types of experiments. The last part of the chapter discusses the selectivity of the sensor and the detection of glucose in artificial tear solutions.

4.1 Functionalization and characterization of the graphene channel

The effectiveness and reliability of biosensing *via* EG-GFETs highly depend on the integrity of the functionalization processes applied to graphene. In our devices, the glucose-sensing mechanism relies on the immobilization of the GOx enzyme on graphene. We chose this specific enzyme for its high specificity to glucose and large turnover (*i.e.,* the number of substrate molecules that an enzyme can convert to the product of reaction per active site per unit time before the enzyme is fully saturated with the substrate, which is essentially an indication of the enzyme's catalytic efficiency) [159], [160], [161]. The process required to immobilize GOx on graphene is shown in Figure 15a. Considering that covalent modifications can alter graphene's electrical properties, a pyrene linker was chosen, PBASE, to anchor the enzyme onto graphene via an amine bond, which is facilitated by the nucleophilic substitution reaction of N-hydroxysuccinimide (NHS) [162]. Raman spectroscopy was used to assess the evolution of the morphologic and electronic properties of graphene in response to the functionalization processes. All the three spectra of Gr (as-transferred graphene), Gr/PBASE and Gr/PBASE/GOx show the typical features of high-quality, monolayer graphene, with an I_{2D}/I_G ratio of 2.30, 1.47 and 1.45, respectively (Figure 15a). In Gr/PBASE, new peaks at 1230.8 cm^{-1},1384.5 cm^{-1} and 1621.2 cm^{-1} appear, which can be assigned to the pyrene-based molecule [136], [163], [164]. The latter peak is attributed to the pyrene group resonance [165], proving that PBASE is stacked on graphene's surface. The D peak (~1342 cm^{-1}), absent in the Gr spectrum, is found to increase in Gr/PBASE due to the pyrene immobilization (via orbital

hybridization of the PBASE molecules with the graphene plane) [165]. Gr/PBASE/GOx shows a slight increase in the intensity of the D peak with respect to the previous stage. The Raman spectra of GOx as a powder and in a water solution was measured (Appendix I), which, to our knowledge, has not been previously reported. This was performed with the intent of identifying any GOx-related modes in the Gr/PBASE/GOx spectrum. The GOx spectra has two main regions of interest: 1100-1800 cm^{-1} and 2800-3100 cm^{-1}. We fitted the latter region (Appendix I), where the most intense and wide peak appears at 2932 cm^{-1}. By zooming in on the Gr/PBASE/GOx spectrum, a small and wide feature around 2950 cm^{-1} can be observed which could further corroborate the enzyme immobilization (no features exist in the corresponding Gr/PBASE spectral range – Appendix I). A detailed analysis of the G and 2D peak position and full width at half maximum (FWHM) in the three cases was performed. The distribution of the G and 2D peaks' FWHM for each case is shown in Appendix II. As a further aid to discriminate the emergence of charge doping and/or mechanical strain [166], [167]. The 2D *vs* G frequency plot (Figure 15c) and corresponding linear transformation plot (Figure 15d), which inform on potential variations in mechanical strain and charge density [168]. In this plot, higher (lower) charge density represents higher (lower) hole doping in graphene, whereas higher (lower) mechanical strain represents tensile (compressive) stress. The information about the FWHM of the functionalization process is shown in Appendix II. In Gr, the extracted values are centered at a G peak position of 1584.2 cm^{-1} (average FWHM 22 cm^{-1}) and a 2D peak position of 2667.5 cm^{-1} (average FWHM 40 cm^{-1}). Figure 15d shows a significant hole density, indicating the presence of p-type doping, as well as the presence of compressive stress, which can be both expected in CVD graphene transferred by PMMA wet method [168], [169]. In Gr/PBSE, G and 2D peak position values are centered at 1586.9 cm^{-1} (average FWHM 23 cm^{-1}) and 2671.6 cm^{-1} (average FWHM 40 cm^{-1}), resulting in ~ 3 and ~ 4 cm^{-1} blueshift, respectively. Figure 15d indicates a slight increase in the hole density of graphene, which would further confirm the stacking of pyrene molecules on graphene, due to its electron-withdrawing properties [164], [170], [171]. The observed minor increase of the tensile strain might result of the interaction between the immobilized pyrene molecules and graphene. Finally, in Gr/PBASE/GOx, G and 2D peak position values are centered at 15 .3 cm^{-1} (average FWHM 26 cm^{-1}) and 2671.7 cm^{-1} (average FWHM 42 cm^{-1}), correspondingly. There is a slight redshift of the G peak (1.3 cm^{-1}), while the 2D peak position remains unchanged. However, the $FWHM_{2D}$ and the $FWHM_{G}$ increase by 2 cm^{-1} and 3 cm^{-1}, respectively, often related to charge doping. Figure 15d shows a reduced hole density and further increase in tensile strain, which would confirm the binding of GOx to PBASE.

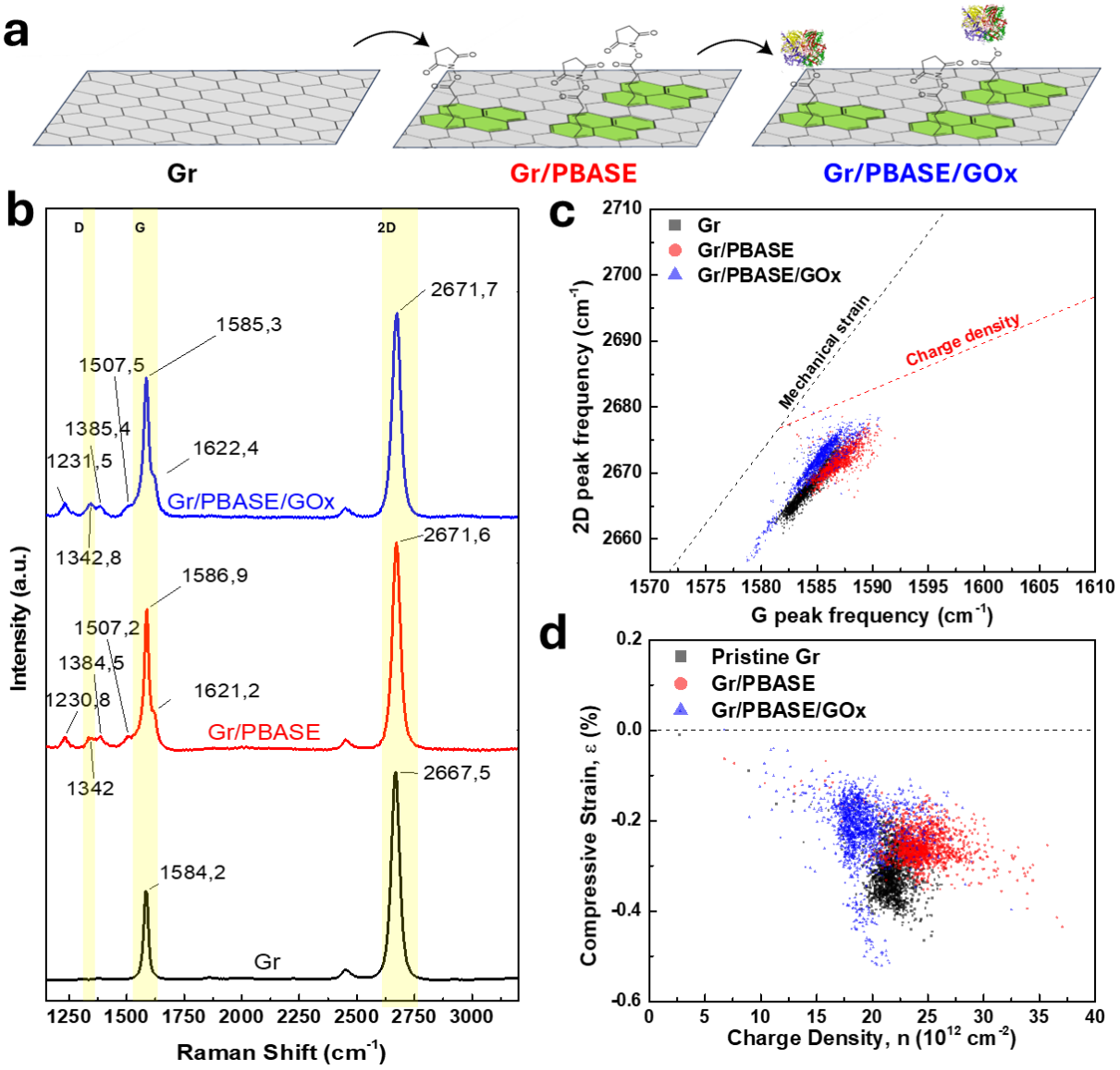


Figure 15: Detailed characterization of graphene's functionalization process for glucose detection. (a) Functionalization process. (b) Raman spectra of each stage involved in the immobilization of GOx molecules on graphene: pristine graphene (Gr, black), PBASE modification (Gr/PBASE, red) and GOx immobilization (Gr/PBASE/GOx, blue). Each spectrum is an average of 1500 measurements. (c) 2D vs G frequency plot of the 1500 measurements of Gr, Gr/PBASE and Gr/PBASE/GOx. (d) Mechanical strain (ε, %) vs charge (hole) density (n, 10^{12} cm^{-2}) plot of 1500 measurements for each functionalization step. The plot is a linear transformation of the 2D vs G frequency plot shown in Figure 15c.

The biofunctionalization was also analyzed by XPS. The C 1s and N 1s high-resolution spectra are shown in Figure 16a-b, respectively, while the survey spectra is reported in Appendix III. The immobilization of GOx on graphene was further confirmed by the significant increase in the N 1 s peak intensity, which increased from 0.9 at.% (relative atomic concentration) in Gr to 2.2 at.% in Gr/PBASE to 7.6 at.% in

Gr/PBASE/GOx (see Table 1). In the last two samples, the N 1 s peak is centered at approximately 400 eV, which is in close agreement with previous works on PBASE-functionalized graphene [172]. A small feature appears at approximately 398.5 eV, likely due to the formation of pyridinic rings [173] (potentially from side reactions involving PBASE). The C 1s fittings provide complementary information from the evolution of C-O/C-N, C=O, and C=OO/N-C=O components (Table 2), which appear in all samples in addition to the two typical features of CVD graphene (*i.e.*, the main asymmetric peak at 284.5 eV and the corresponding shake-up satellite at 290.9 eV, and the C-C sp^3 component). In particular, the C-O/C-N component increases from 11.7 at.% to 18.2 at.% (from Gr to Gr/PBASE/GOx) owing to the high amount of amine and amide functional groups in the PBASE/GOx structure. This component slightly shifts toward lower binding energies (from 286.1 to 285.9 eV), indicating that several C–N bonds appear with respect to C–O bonds. Similarly, C=O (272.2 eV) and C=OO/N-C=O components increase [174], with a shift in the second component toward a lower binding energy (from 288.8 to 288.5 eV) due to the greater presence of amide groups, further confirming the effective biofunctionalization of the graphene surface.

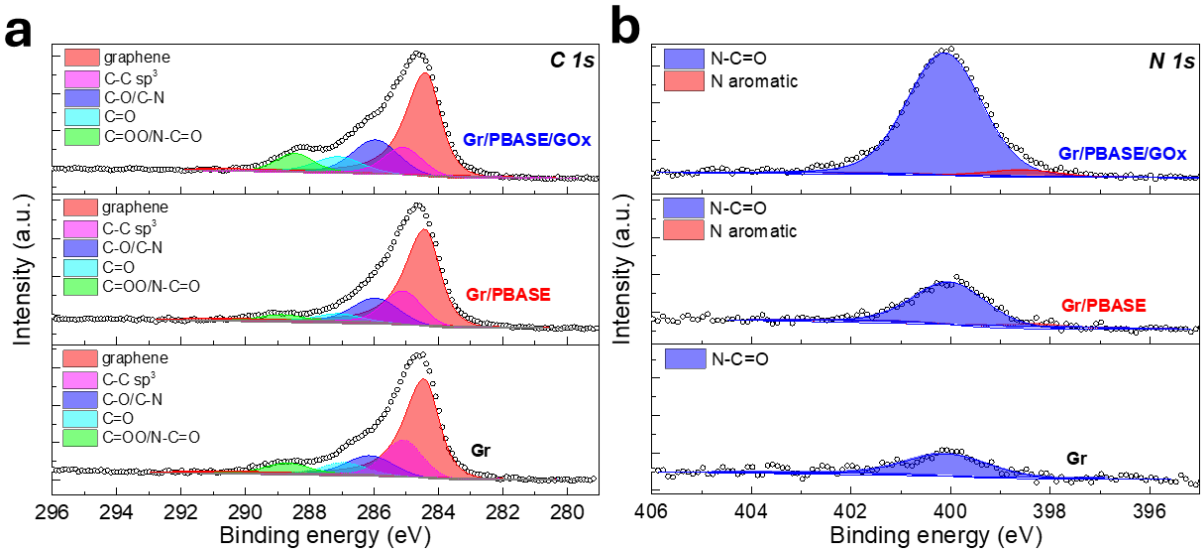


Figure 16: (a) Deconvoluted high-resolution C 1s and (b) N 1s spectra of Gr, Gr/PBASE and Gr/PBASE/GOx.

Table 1. Relative at. % of carbon, nitrogen, and oxygen calculated from C 1 s, N 1 s, and O 1 s high-resolution peaks, respectively, for the as-transferred graphene, Gr/PBASE, and Gr/PBASE/GOx samples.

Sample	C tot.	N tot.	O tot.
Gr	64.9 %	0.9 %	34.2 %
Gr/PBASE	68.1 %	2.2 %	29.7 %

Gr/PBASE/GOx	67.1 %	7.6 %	25.3 %

Table 2. Components used to fit the C 1 s spectra of the as-transferred graphene, Gr/PBASE, and Gr/PBASE/GOx samples. For each of them, the binding energy position in eV and the relative atomic concentration (at. %) are reported.

Sample	**C-C graphene**	**p-p* graphene**	**C-C**	**C-O/C-N**	**C=O**	**C=OO/N-C=O**
Gr	284.5; 55.0 %	290.9; 2.2 %	284.9; 19.0 %	286.1; 11.7 %	287.1; 6.4 %	288.8; 5.7 %
Gr/PBASE	284.5; 56.7 %	290.9; 2.3 %	285.0; 18.2 %	285.9; 14.6 %	287.1; 4.1 %	288.9; 3.1 %
Gr/PBASE/GOx	284.5; 51.2 %	290.9; 2.0 %	285.0; 12.7 %	285.9; 18.2 %	287.2; 8.2 %	288.5; 7.7 %

The described micro-fabrication of the EG-GFETs utilized in this work are described in Appendix IV. To achieve a biosensing system based on EG-GFETs, both the graphene FET channel and the gold (Au) gates need to be properly functionalized. The complete EG-GFETs functionalization method is depicted in Figure 17a and consists of three steps: 1) Au gates passivation with a thin self-assembled monolayer (SAM) of DDT, an Au blocking agent, to prevent non-specific interaction of biological sample and restrict the functionalization to the graphene channel; 2) the immobilization of GOx (already represented in Figure 15a; 3) ethanolamine (ETA) incubation to block any remaining active free ester groups from PBASE after enzyme binding, further reducing potential sources of non-specific binding and detection.

Each functionalization stage is verified with electrical measurements by plotting the transfer curves (Figure 17b) and measuring the Dirac point shift (ΔV_{DIRAC}) with respect to the previous functionalization step (Figure 17c). Before any functionalization stage (Gr), the sensors are measured to provide a baseline for the shifts of the next stage. Shifts from the baseline transfer curve measurements indicate that charge carrier redistribution in the graphene channel is due to electrostatic potential changes from surface modification. Initially, the V_{DIRAC} value is located at positive gate voltage values (+0.45 V), indicating unintentional p-type doping (Stage 0). Adding DDT to the sensors (Stage 1) causes the V_{DIRAC} to shift by ~ -310 mV owing to the formation of a self-assembled monolayer covering the gold electrode, creating an excess of positive charges in the solution from the dipole moment reorientation of the alkanethiols [32]. Graphene doping level is not altered, as confirmed by Raman spectroscopy G vs 2D frequency plot and respective linear

transformation (Appendix V). The functionalization of graphene is then achieved with PBASE (Stage 2). We observe only a slight shift of approximately +30 mV, indicating additional graphene p-type doping upon π–π stacking [175]. This small variation of the V_{DIRAC} can be explained by a doping competition between pyrene molecules and the solvent used to dilute them. Dimethyl solvents (*e.g.*, DMF, DMSO) have been reported to n-dope graphene [175],[176]. This was further proved by Raman spectroscopy, which shows that G and 2D peak blueshift (Appendix V) after incubation with bare DMSO (corresponding to a decrease in hole density; Appendix V). Additionally, at the PBASE functionalization stage, both the electron and hole branches of the transfer curve become slightly less steep, indicating a small decrease in the mobility of both types of carriers. The NHS ester group of PBASE remains free to form a covalent bond with the biorecognition probe. GOx is immobilized on graphene (Stage 3) by binding to the free ester group of PBASE. The immobilization of the enzyme results in a V_{DIRAC} shift of -30 mV, in agreement with the Raman shift indicating n-type doping. Finally, ETA (Stage 4) causes the V_{DIRAC} to shift by -5 mV.

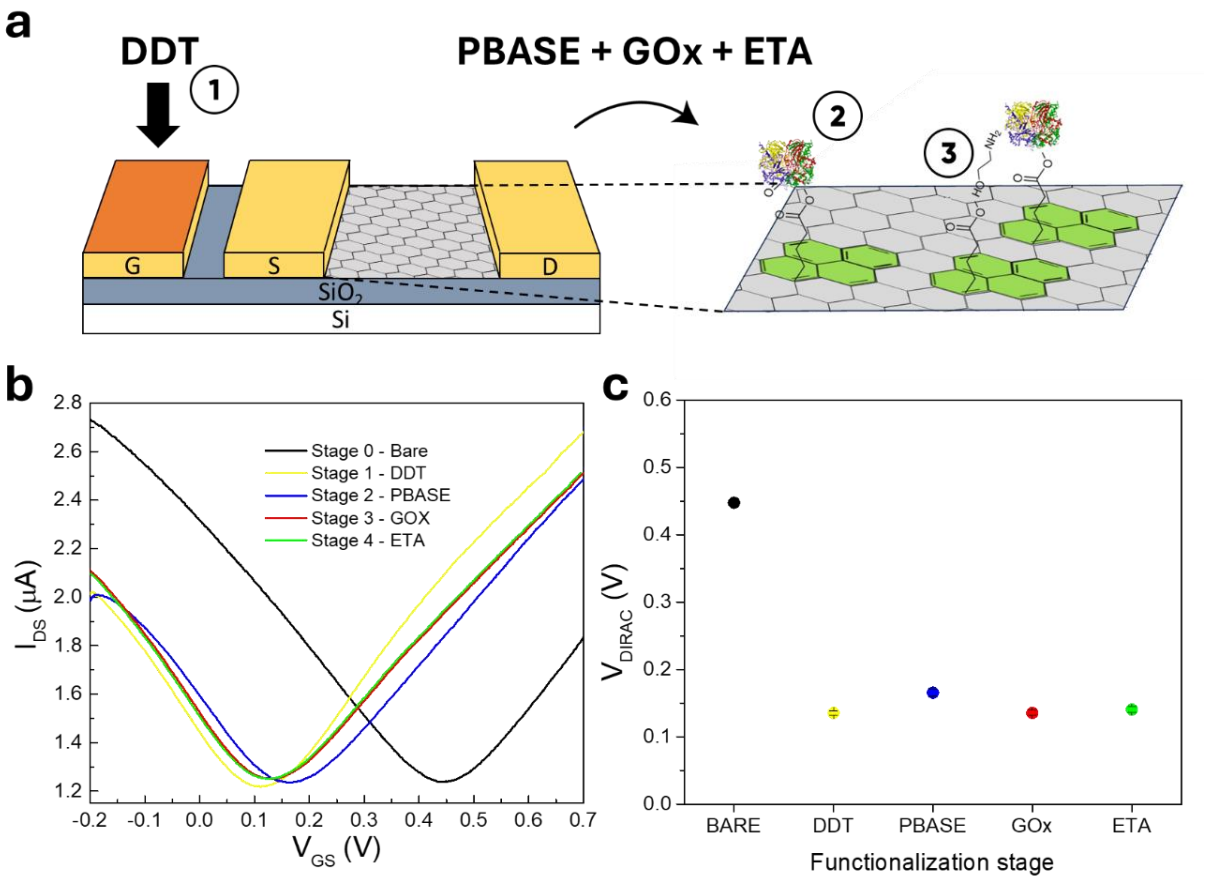


Figure 17: Functionalization and characterization of electrolyte-gated graphene field-effect transistors (EG-GFETs) for glucose detection. (a) Schematic of an EG-GFET and the total functionalization process involved in graphene

modification for glucose sensing: 1) DDT - Au gate passivation. 2) PBASE - non-covalent modification with pyrene linkers + GOx - immobilization of the biorecognition element, GOx. 3) ETA - blocking of unreacted sites of PBASE. (b) Transfer curves of one EG-GFET measured after each functionalization stage and (c) their respective average value of the V_{DIRAC} for 50 transistors (data is represented in mean ± standard error mean (sem)).

4.2 Analysis of the glucose sensing mechanism

Once fully functionalized (Gr/PBASE/GOx/ETA), the EG-GFET devices were tested for glucose sensing (Figure 18a). A first V_{DIRAC} shift of +26 ± 4 mV occurs at 1 aM and then the values continue to increase with the glucose concentration for six orders of magnitude, with a sensitivity of 10.6 mV/decade. The trend reaches a plateau at 1 pM (ΔV_{DIRAC} ~ 100 mV), which remain rather constant up to 1 mM (Appendix VI, red circles). The corresponding transfer curves are reported in Figure 18b. These results demonstrate a marked p-type doping effect due to increasing glucose concentration in fully functionalized devices. For a more comprehensive analysis, we have also tested partially functionalized devices to understand the sensing mechanism. The Gr and Gr/PBASE devices behave very differently in the same glucose concentration range (Figure 18a). The first, apparent difference is that the V_{DIRAC} shifts are negative in both cases, demonstrating n-type doping. Also, no clear trend is visible for concentrations < 10 fM. At higher concentrations, the values tend to stabilize or change marginally (Appendix VI). Both these results are different from what was previously obtained, as the clear n-type doping was not obtained and instead unpredictability was seen throughout the concentrations. Simulations via density functional theory method demonstrated that glucose can absorb on pristine graphene, inducing electron transfer and n-type doping [177]. However, in the case of Gr/PBASE, the doping effect becomes weaker since the PBASE layer can interfere with the electron transfer. The Gr/PBASE/GOx/ETA devices were analyzed by Raman spectroscopy in the 1 nM-1 mM glucose concentration range (Figure 18c). The 2D and G peak positions upshift significantly at 1 nM and then increase marginally at higher concentrations. At 1 mM, the two peaks upshift by +6.6 ± 0.5 cm^{-1} and +8.6 ± 0.5 cm^{-1} (with respect to the pristine case at 0 M), respectively. We evaluated the corresponding contributions of both mechanical strain and hole doping (Appendix VII), which further confirmed the p-type doping effect of glucose on the fully functionalized device.

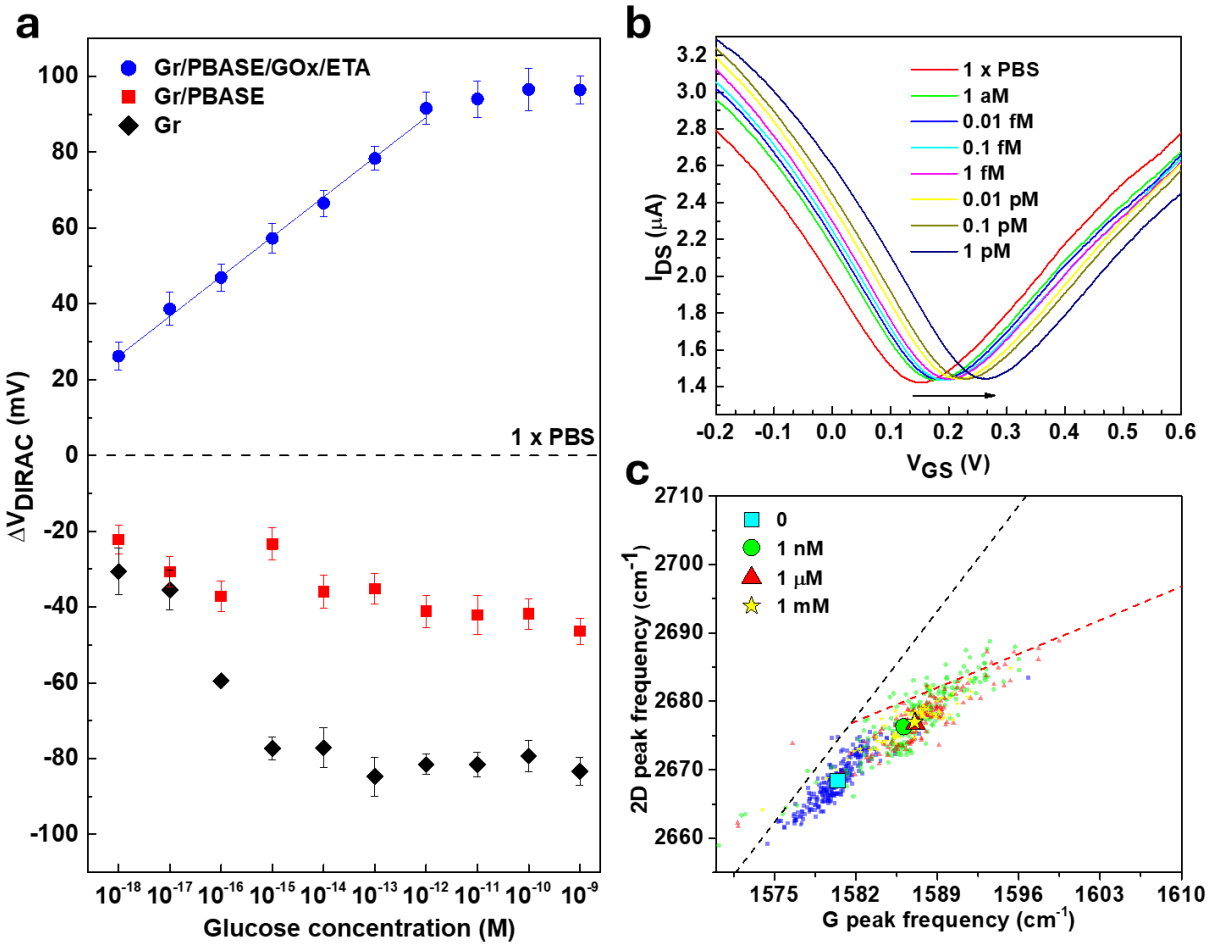


Figure 18: Glucose sensing via EG-GFETs and Raman spectroscopy in 1x PBS. (a) Comparison of the ΔV_{DIRAC} as a function of glucose concentration for Gr*, Gr*/PBASE and Gr*/PBASE/GOx/ETA. In the latter, V_{DIRAC} positively shifts as the glucose concentration increases, resulting in p-type doping with the lowest reported glucose LOD of 1 aM. The negative control tests show the opposite response. The data are presented as mean ± sem. (b) Transfer curve trend of one transistor for the different glucose concentrations in the linear range (1 aM-1 pM). (c) 2D vs G frequency plot of Gr/PBASE/GOx/ETA with varying glucose concentration (1 nM-1 mM). For each concentration, a distribution of the peaks position within 300 measurements (over a total area of 300 μm^2) is displayed with the corresponding average point. *The surface was treated with DDT to passivate the Au electrodes.

Building on the experimental findings, we propose an interpretation of the underlying sensing mechanism. In solution, GOx catalyzes the oxidation of glucose and yields two byproducts: gluconic acid and H_2O_2. This two-step catalysis involves the transfer of electrons from glucose to the enzyme's prosthetic group, typically a flavin adenine dinucleotide (FAD) cofactor. FAD oxidizes glucose into gluconolactone and gets reduced to $FADH_2$ (Equation 1). Gluconolactone is hydrolyzed in the presence of water to form gluconic

acid (Equation 2). The FAD subunit is regenerated from $FADH_2$ through the reduction of O_2 to H_2O_2 (Equation 3). Upon regeneration, FAD continues to oxidize glucose, resulting in cyclic interactions for continuous H_2O_2 and gluconic acid production.

$$GOx\ (FAD) + glucose \rightarrow GOx\ (FADH_2) + gluconolactone \quad (1)$$

$$gluconolactone + H_2O \rightarrow gluconic\ acid \quad (2)$$

$$GOx\ (FADH_2) + O_2 \rightarrow GOx\ (FAD) + H_2O_2 \quad (3)$$

Considering these chemical reactions, we propose that the p-type doping occurring in the devices could stem from the interaction between H_2O_2 and the functionalized graphene. In similar sensing systems, H_2O_2 typically undergoes a voltage-driven decomposition, which releases molecular oxygen, protons and free electrons [162], [178], [179]:

$$H_2O_2 \rightarrow O_2 + 2H^+ + 2e^- \quad (4)$$

In principle, free electrons should transfer to graphene (especially at defect sites, like vacancies) and induce n-type doping [180]. We tested this hypothesis by exposing the Gr and Gr/PBASE/GOx/ETA devices to increasing H_2O_2 concentrations Figure 19a.

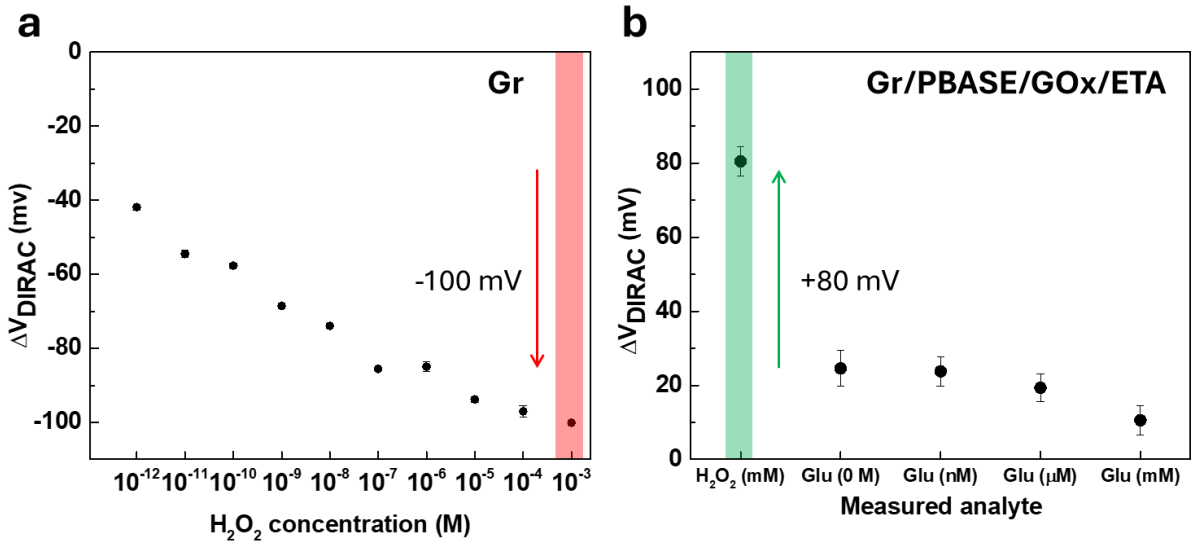


Figure 19: H_2O_2 measurements on EG-GFETs. (a) 1 µM-1mM H_2O_2 influence on V_{DIRAC} of bare graphene surfaces (only DDT passivation). The sensor shows n-type doping. (b) 1 mM H_2O_2 measured on Gr/PBASE/Gox/ETA, showing p-type doping. On the same sensor, after washing with 1 x PBS (Glu 0 M), glucose (Glu nM-Glu mM) was measured, with no variation of the V_{DIRAC} with increasing concentrations. The same concentration of H_2O_2 (1 mM) exhibited

opposite behaviour for Gr and Gr/PBASE/GOx/ETA, confirming that glucose detection is based on the detection of H_2O_2.

The Gr devices do indeed exhibit consistent negative ΔV_{DIRAC} shifts at increasing concentrations when H_2O_2 is added (up to -100 mV at 1 mM, Figure 19a). By contrast, the Gr/PBASE/GOx/ETA devices show positive V_{DIRAC} shifts, up to +80 ± 4 mV at 1 mM, indicating strong p-type doping (Figure 19b). This could be explained by two reasons: i) the pyrene monolayer with bound enzymes can shield the graphene and mitigate the direct electron transfer; ii) in proximity of graphene, H_2O_2 might decompose into hydroxide (OH^-) ions [178], [181]. In slightly basic conditions (the PBS solution has pH = 7.4), the OH^- concentration can further increase and upshift the V_{DIRAC} by an accumulation of positive counter-ions from the electrolyte [182], [183]. We evaluated the response to glucose of the Gr/PBASE/GOx/ETA devices after direct exposure to H_2O_2 (see Section 4.4). As shown in Figure 19b, after washing away the H_2O_2 and cleaning the sensor's surface in PBS (corresponding to "Glu 0 M"), the device does not respond to glucose in the 1 nM-1 mM concentration range. This can be explained by an inhibitory effect of high concentration of H_2O_2 on the catalytic activity of GOx [184], which in turn would also clarify the plateau in the response to glucose of the regular EG-GFET devices after 1 pM (Figure 19a).

4.3 Investigation of the sensor selectivity

To assess the selectivity of the sensors, we tested their response to lactate (a compound produced by glycolysis [185]) and ascorbic acid in the same concentration range of glucose (Appendix VIII). Figure 20a compares the response of the sensors to glucose, lactate and ascorbic acid. Differently from the linear ΔV_{DIRAC} trend for glucose, the response to lactate and ascorbic acid exhibited a minor and random trend due to non-specific interactions or noise. To further confirm the selectivity and capacity of the sensors to detect glucose in different mediums and with different analytes, ascorbic acid and lactate were now mixed with glucose in a ratio of 1:1:1. Figure 20b shows a linear trend (3.9 mV/decade) and an LOD 1 aM. The sensors showed p-type doping with increasing concentrations of the analytes. The lower overall response and sensibility can be justified by the increasing concentrations of the interferents with increasing concentrations of glucose, which could be blocking potential reaction sites.

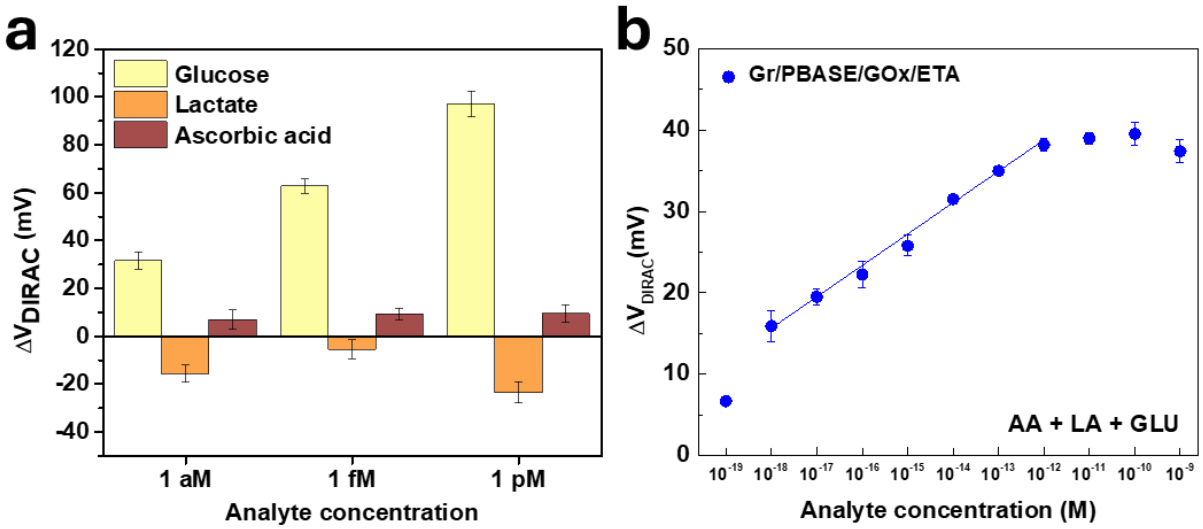


Figure 20: Selectivity of the EG-GFETs with Gr/PBASE/GOx/ETA configuration. (a) Comparison of the sensors' response to glucose and lactate in 1 x PBS, showing linear and erratic trends, respectively. (b) Calibration curve of the ΔV_{DIRAC} as a function of glucose, ascorbic acid and lactate concentrations in 1 x PBS, in a ratio of 1:1:1, showcasing the sensitivity and selectivity of the sensors in a complex medium.

The selectivity for glucose was further evaluated in a simulated biological fluid (*i.e.*, an undiluted commercial artificial tear), to test the potential clinical application of the sensors. As shown in Figure 21, the ΔV_{DIRAC} shifts exhibit a clear and consistent response across the tested concentration range, with a linear trend (4.9 mV/decade) and a remarkable LOD of 100 aM. The sensors exhibit p-type doping with increasing concentrations of glucose for six orders of magnitude (until saturating at 0.1 nM, with a ΔV_{DIRAC} ~ 45 mV). The reduction in sensitivity might be explained by the composition of the artificial tear, which contains several analytes (electrolytes, buffers, acids) at high concentration that can hinder the direct interaction between glucose and GOx.

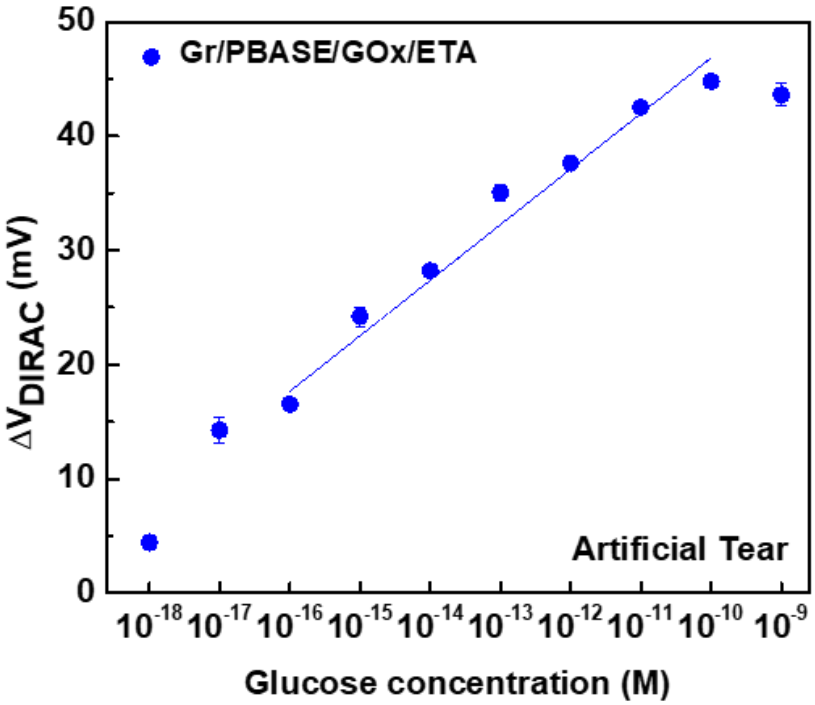


Figure 21: Selectivity of the EG-GFETs with Gr/PBASE/GOx/ETA configuration. Calibration curve of the ΔV_{DIRAC} as a function of glucose concentrations in an artificial tear, showcasing the sensitivity and selectivity of the sensors in a complex medium.

Our sensors reached the aM level, which is 14 orders of magnitude lower than the lowest reported for configurations based on Gr/PBASE/GOx [186], [187]. Such LOD level is also at least three orders of magnitude lower than that ever reported for the best-performing glucose sensors (fM level) [188]. Devices enabling aM-level detection of glucose could pave the way for next-generation non-invasive glucose monitoring. Several sensing strategies have been developed to achieve high sensitivity and low LOD for glucose sensing (Table 3). These glucose sensors are generally categorized into two types: non-enzymatic and enzymatic. Non-enzymatic sensors can leverage the catalytic activity of different electrode systems, having achieved LODs up to the nM range [189], [190], [191]. Fiber-based sensors pushed beyond this limit and reached LOD in the pM-fM range by using tilted fiber Bragg grating combined with surface plasmonic resonance [188], [192], [193]. Enzymatic sensors, particularly those using GOx, can reach top-level sensitivity and selectivity by perfecting the enzyme immobilization through functional materials, such as Nafion, liquid crystals, nanowires, nanorods and graphene derivatives [105], [107], [186], [187], [194], [195], [196], [197], [198], [199], [200], [201], [202], [203]. These systems have achieved LODs in the nM-pM level. Our sensors reached the aM level, which is 14 orders of magnitude lower than the

lowest reported for configurations based on Gr/PBASE/GOx [186], [187]. Such LOD level is also at least three orders of magnitude lower than that ever reported for the best-performing glucose sensors (fM level) [188]. Devices enabling aM-level detection of glucose could pave the way for next-generation non-invasive glucose monitoring.

Table 3. State-of-the-art glucose sensing, considering their sensing system, detection method, LOD, linear range, sensitivity and selectivity.

Type	Sensing system	Detection method	LOD	Linear range	Sensitivity	Selectivity	Ref
Non-Enzymatic	Cu-Gr-COOH-Au electrode	CV and chronoamperometry	7.96 nM	0.1 μM-5.48 mM	1142 μA mM^{-1} cm^{-2}	Yes	[189]
	CuO-NiO-MFs/FTO	AM	1 nM	3 M-0.51 mM	3165.53 A mM^{-1} cm^{-2}	Yes	[190]
	Gr/Cu Electrode	AM	0.5 μM	0.5 μM–4.5 mM	NR	Yes	[191]
	TFBG-SPR-AuNPs-PMBA	SPR	295 pM	1 nM-10 mM	NR	Yes	[192]
	TFBG/GO/PBA	SPR	1 fM	1 fM–10 pM	NR	NR	[188]
Enzymatic	PET/CNTs/GOx	Accumulation mode and AM	4.7 ± 1.4 nM	4 nM–5 μM	0.33 ± 0.04 nC/nM	NR	[194]
	TFBG/GO/EDC-NHS/GOx	SPR	1 mM	0 mM–8 mM	0.24 nm/mM	Yes	[195]
	CNT NEEs/GOx	AM	0.08 mM	0.08 mM-30 mM	NR	Yes	[196]

Silk/Gr/Silk-GOx	TC	0.1 mM	0.1 mM–10 mM	2.5 μA/mM	Yes	[105]
GCE-RGO-GOx	CV and AM	0.1 mM	0.1 mM–27 mM	1.85 μA mM^{-1} cm^{-2}	Yes	[197]
Gr/CNT/ZnO/GOx	CV	4.5 ±0.08 μM	10 μM-6.5 mM	5.362 (±0.072) μA mM^{-1} cm^{-2}	NR	[198]
AuNWs/GOx	CV	3 μM	10 μM–100 mM	7.2 mA mM^{-1} cm^{-2}	Yes	[199]
ZNA/GOx	Field emission	1 nM	1 nM-50 μM	NR	NR	[200]
PB-modified GCE/Nafion/GOx	AM	1 μM	1 μM–5 mM	NR	NR	[201]
PET/Gr/PBASE/GOx	TC	3.3 mM	3.3 mM-10.9 mM	NR	NR	[186]
Gr/PBASE/GOx	TC	0.1 mM	NR	NR	NR	[187]
Nafion/Pt-xGnP/GOx	AM	1 μM	1 μM-20 mM	61.5 ± 0.6 μA mM^{-1} cm^{2}	NR	[202]
Gr/PtNPs/Nafion/GOx-CHIT	TC	0.5 μM	0.5 μM-1 mM	173 mV/decade	Yes	[107]
UV-5CB/Au-grid/GOx	Optical Response	1 pM	1 pM-50 nM	NR	Yes	[203]
Gr/PBASE/GOx/ETA	TC	1 aM	1 aM-1 pM	10.6 mV/decade	Yes	This work

CV – Cyclic voltammetry; SPR – surface plasmonic resonance; AM – amperometry; TC – transconductance; TFBG – tilted fiber Bragg grating; GO – graphene oxide; PBA – pyrene-1-boric acid; AuNPs – gold nanoparticles; PMBA – p-mercaptophenylboronic acid; PB – Prussian blue; MFs – microfibers; FTO – fluorine tin oxide; GCE – glass carbon electrode; PET – polyethylene terephthalate; ZNA – ZnO nanorod arrays; EDC – 1-ethyl-3-(3-dimethylaminopropyl) carbodiimide; AuNWs – gold nanowires; CNT – carbon nanotubes; xGnP – exfoliated graphite nanoplatelets; UV-5CB – UV-treated 4-cyano-4'-pentylbiphenyl; NEEs – nanoelectrode ensembles; NR – not reported.

4.4 Conclusion

The comprehensive characterization of the functionalization steps of the graphene channel using Raman spectroscopy and X-ray photoelectron spectroscopy confirmed the correct immobilization of glucose oxidase. This allowed us to better understand the changes made on graphene at each step. Furthermore, the V_{DIRAC} monitoring through these steps, including the addition of DDT required to passivate the gold electrodes, and ethanolamine to block the unreacted PBASE sites, confirmed the successful functionalization of the transistor. The analysis of the glucose sensing mechanism in the EG-GFETs highlighted distinct behaviors across fully and partially functionalized devices. The fully functionalized Gr/PBASE/GOx/ETA devices demonstrated a strong p-type doping effect, with a sensitivity of 10.6 mV/decade and a detection limit as low as 1 aM. The p-type doping effect originates from the increase concentration OH^- which results in the accumulation of positive counter ions from the electrolyte. This marked p-type doping was further confirmed by Raman spectroscopy, which showed significant upshifts in the 2D and G peak positions, with increasing glucose concentrations, indicating hole doping. In contrast, partially functionalized devices, such as Gr and Gr/PBASE, displayed negative V_{DIRAC} shifts, indicative of n-type doping. This discrepancy can be explained by the electron transfer effect that glucose has on the bare graphene surface, while the reduced response from the Gr/PBASE devices suggests that PBASE acts like a "shielding" layer and weakens this effect. The experimental results showed that H_2O_2 causes a negative shift on bare Gr likely due to electron transfer effect and a positive shift on fully functionalized transistors. Moreover, the sensor's response to glucose was found to be hindered after high concentrations of H_2O_2, possibly due to the inhibitory effect on GOx's catalytic activity, thus explaining the plateau observed in glucose detection at concentrations above 1 pM. Finally, experimental tests were conducted to test the selectivity of the sensor for glucose against interfering analytes. An ultra-low limit of

detection of 1 aM with a sensitivity of 3.9 mV/decade was achieved, when sensing in the presence of lactate and ascorbic acid. Glucose detection on an artificial tear resulted in a limit of detection of 100 aM with a sensitivity of 4.9 mV/decade.

5. TOWARDS GLUCOSE SENSING IN GRAPHENE-BASED CONTACT LENSES

In this chapter, we explore the various challenges that needed to be solved to transfer CVD graphene to contact lenses. After an optimization phase, we designed a novel approach to facilitate and scale up the transfer process, thus achieving a higher throughput. Following this optimization, we developed a protocol to functionalize the graphene coating for glucose sensing. To assess the effectiveness of this protocol, we employed multiple characterization techniques including Raman spectroscopy, water contact angle measurements, and ultraviolet-visible spectroscopy.

5.1 Graphene integration in contact lenses

CVD graphene has been extensively explored in the biosensing field due to its biocompatibility and cost-effectiveness. In contact lens technology, its optical transparency provides additional benefits. While a method for transferring graphene onto lenses has been established, it is always essential to verify its quality after fabricating graphene-coated contact lenses. The current transfer method still presents challenges that could lead to damage, requiring careful assessment. Typically, OM is used for a quick evaluation of the graphene's quality, ensuring that no cracks or damage have occurred during the transfer process (Figure 22a-b). As this technique doesn't provide high resolution, it is often challenging to visualize finer details of the graphene's structure. To achieve higher resolution imaging, SEM was employed to characterize the lens. Since they are naturally curved, a method was developed to flatten them without compromising their properties and ensuring accurate imaging. The lenses were placed on top of a glass coverslip and carefully cut into four different zones to maximize the surface area and facilitate flattening (Appendix IX). To visualize the impact of graphene, characterization was initially performed on a bare lens (Figures 22c-d), revealing the material's morphology. In contrast, Figures 22e-f show the graphene-coated lens, where notable differences are observed. The addition of graphene results in a darker color, with visible nucleation sites (darker spots) and clear continuity in the graphene film. This imaging confirmed that the graphene coat remained intact despite the flattening method. The white particles observed are likely residues from the transfer process or dust particles that may have contaminated the sample during handling.

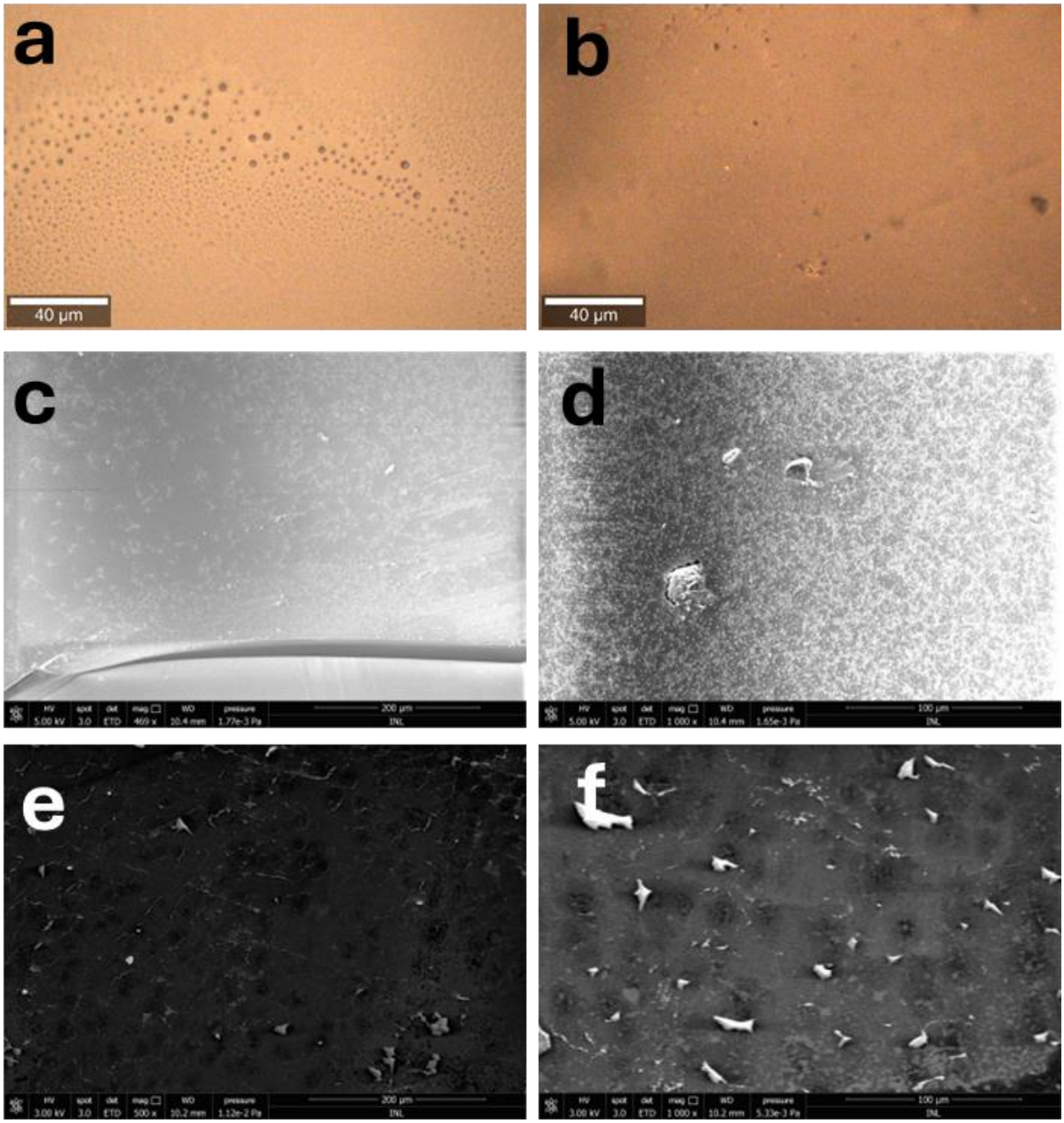


Figure 22: (a-b) OM imaging of a bare and a graphene-coated CL, respectively. (c-d) SEM imaging of bare CLs with 469x and 1000x magnification, respectively. (e-f) SEM imaging of graphene-coated CLs with 500x and 1000x magnification, respectively.

Raman spectroscopy is also an important tool to characterize the graphene-coated lenses as it provides valuable information about the quality and number of layers of the graphene. During these measurements, it is important to consider the influence of the template used to support the lens, as it may impact the final spectrum. To avoid misinterpretation, it is essential to identify the features of both the template and the lenses. When the CL is characterized with the template in place (Figure 23b), most

of the template peaks disappear. This suggests that the template does not interfere with the Raman spectrum of the lens. Although small bumps are present throughout the spectrum, these will not be considered as they have very low intensities and only the most prominent ones will (1452 cm^{-1}, 2906 cm^{-1} and 2963 cm^{-1}).

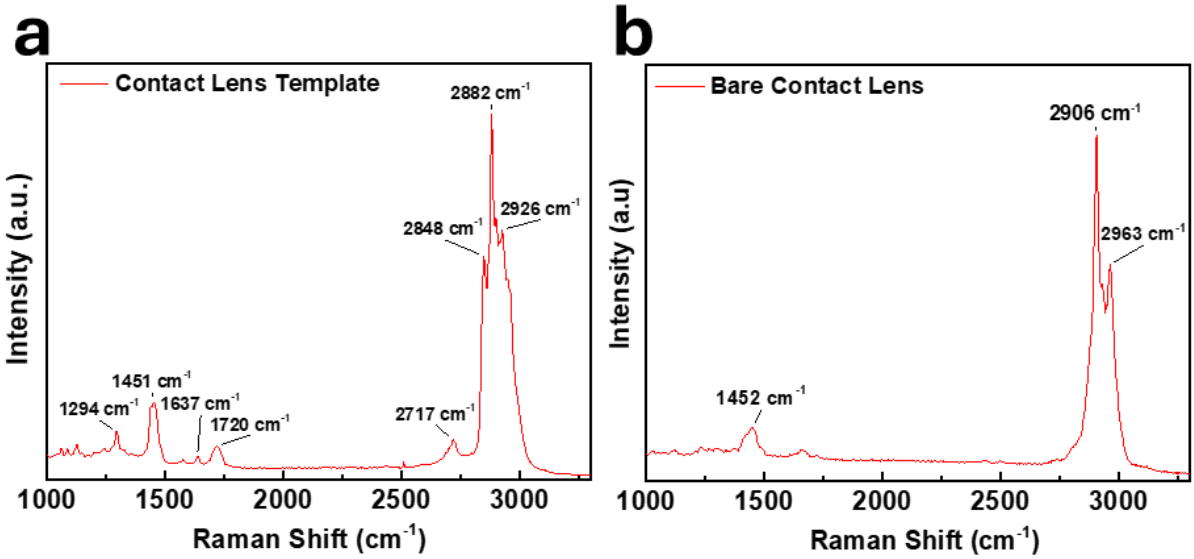


Figure 23: Raman Spectrum of (a) the template utilized as support and (b) a bare CL.

Figure 24a shows an optical image of the graphene-coated lens. It is possible to see nucleation sites (brighter spots) of the graphene which, as expected, gives multi-layered signal (Figure 24b). Figure 24b shows that the graphene is of high quality, due to the high ratio between the 2D and G peak, with very few defects given by the low intensity of the 1350 cm^{-1}. The 2D peak and G peak of the graphene are highlighted with yellow and blue strips, respectively. It is also evident the contribution of the lenses to the spectrum with a small peak around 1450 cm^{-1} and two peaks around 2907 cm^{-1} and 2964 cm^{-1}.

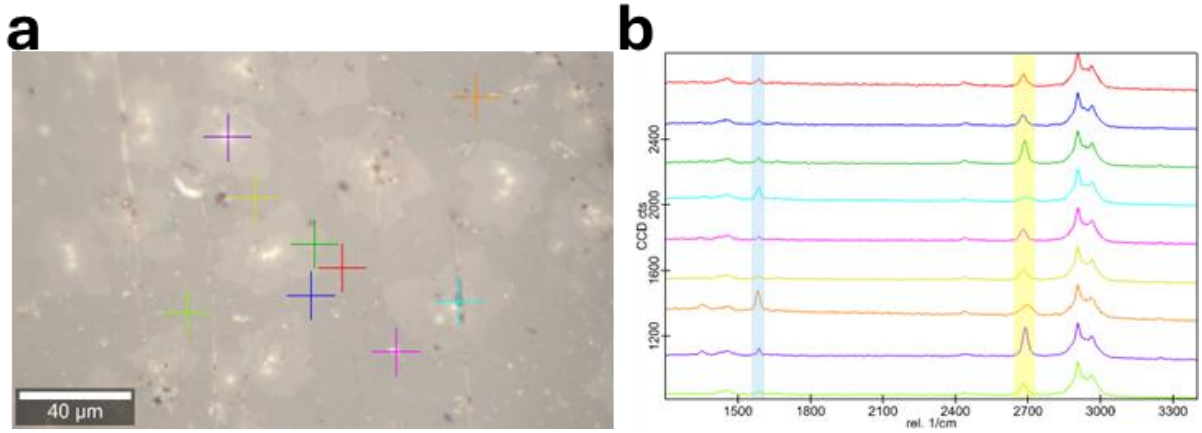


Figure 24: Graphene coated CL. (a) Optical Image (b) Raman Spectrums corresponding to the crosses marked on (a).

In the previous work, the durability of the graphene was evaluated where the lens was stored for 6 months, during which the graphene film remained intact, but another important detail to check is how this solution where the CL was stored might affect other characteristics of the graphene film. Figure 25a shows the 2D vs G plot of the as-transferred graphene-coated CL, alongside a second measurement taken after it being stored solution for one day. When analyzing the linear transformation plot, a shift in the charge density from 23.3 (10^{12} cm^{-2}) to 18.1 (10^{12} cm^{-2}) is noticeable (Figure 25b). The shift indicates that the solution may have played a role in removing some of the impurities or residues, leading to a reduction in the charge density.

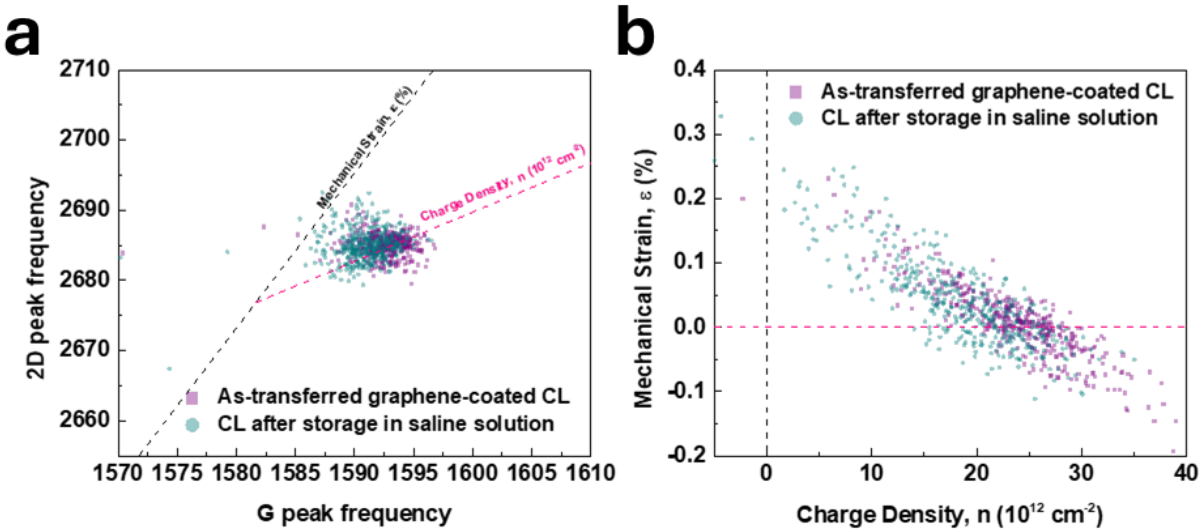


Figure 25: (a) 2D vs G frequency plot of the 500 measurements of graphene-coated CL before and after being stored in CL solution for 1 day. (The before and after corresponding to the purple and dark cyan, respectively). (b) Mechanical strain (ε, %) vs charge (hole) density (n, 10^{12} cm^{-2}) plot of the measurements done in (a). The plot is a linear transformation of the 2D vs G frequency plot shown in Figure 25a.

Wet transfer upscale

One of the main challenges with the current method for transferring graphene is the size of the graphene/Cu foil, which needs to be cut into approximately 2x2 cm squares to match the diameter of the lens. If the foil is cut too large, the graphene may break during the scooping process due to the stress applied to the top of the CL when lifting the film in the final wet transfer step. Another challenge lies in the extreme precision required during the scooping process to ensure complete coverage of the entire CL surface. Any areas left uncovered would lead to damage when removing the PMMA in acetone. Figure 26 illustrates this problem with three graphene-coated lenses placed in an acetone bath to remove the PMMA. Upon removal from the bath, it becomes evident which lenses were not fully covered with

graphene (indicated by the blue arrow). This lack of coverage may be due to either imprecision during the scooping step or cracks introduced during the transfer process. On the other hand, CLs with complete graphene coverage (indicated by the red arrows) were effectively protected from acetone.

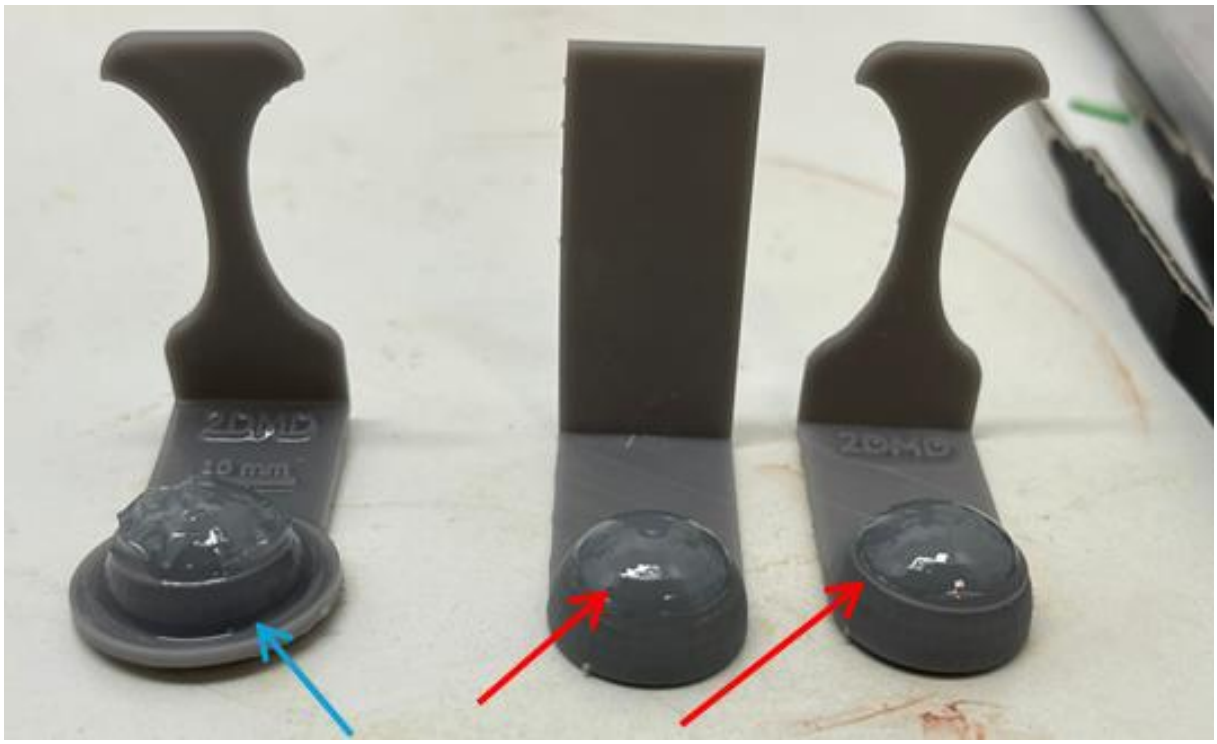


Figure 26: Three different lenses after polymer removal, where the one indicated with the blue arrow was not fully covered with graphene and the two indicated by the red arrow were fully covered.

To address these challenges, a new template was designed. Figure 27a shows the template, which includes four semi-spherical structures, designed in AutoCAD and 3D-printed in grey resin. This new holder features spikes surrounding each semi-spherical structure to help shape and cut the PMMA/Gr film. The inset in Figure 27a shows the template with four CLs after the graphene scooping process. The spikes assist in shaping the graphene into a spherical form, preventing the film from rupturing due to the strain that would otherwise occur from excess graphene. During the scooping process, the spikes generate friction on the PMMA/Gr film, slowing its descent and ensuring a softer contact between the film and the CL, which helps to avoid damage. Figure 27b shows a map of one zone in one of the CLs transferred, demonstrating the continuity and preservation of the graphene's characteristics using this new method. Figure 27c presents the average spectra of Raman maps showing averages from 10 different zones across the four CLs. With the introduction of this new template, the transfer process has

become more efficient. The size of the graphene/copper (Gr/Cu) foil is no longer a limiting factor. Moreover, the precision required to achieve a perfect transfer has been significantly reduced.

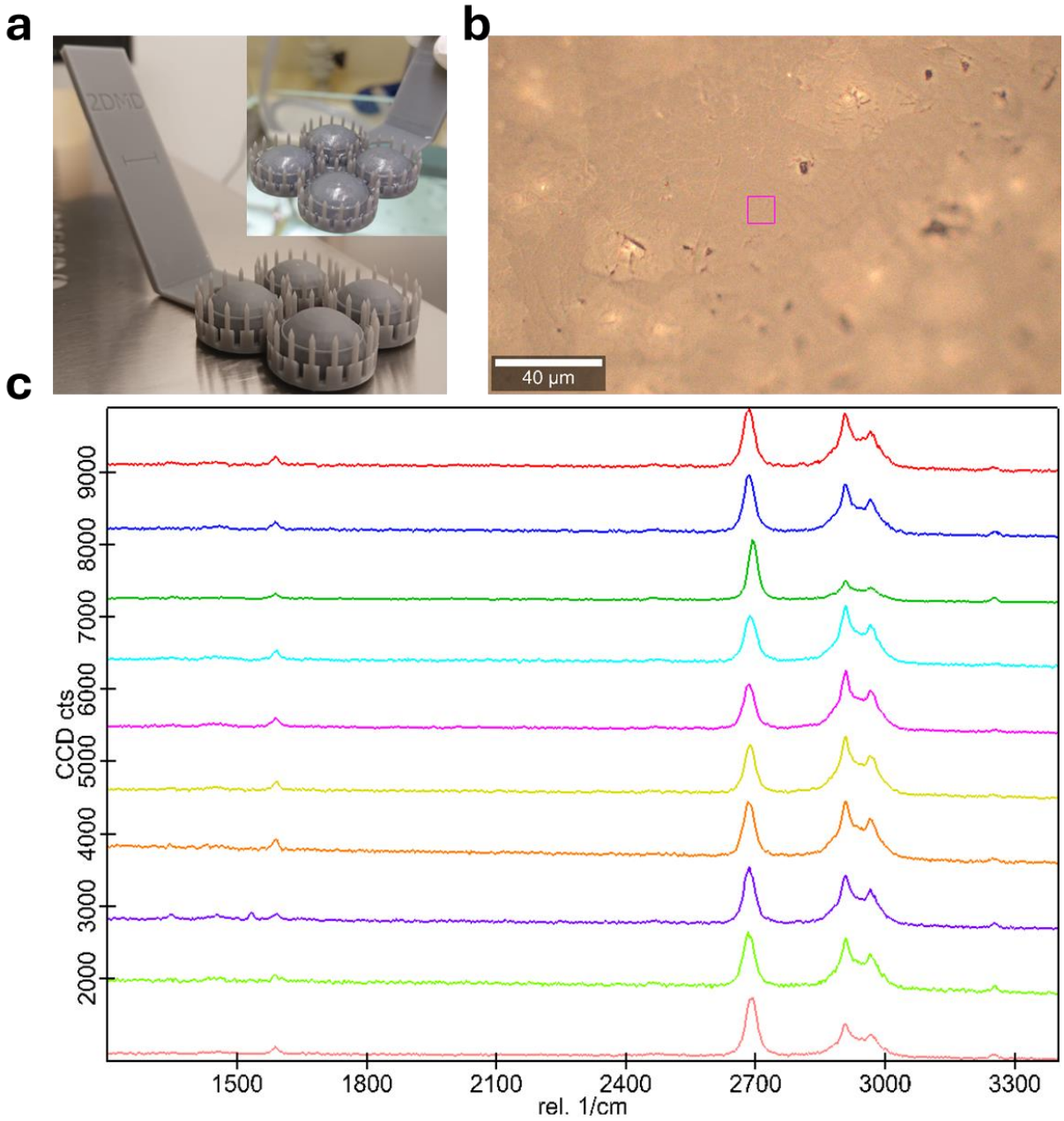


Figure 27: (a) 3D-printed template designed to optimize the transfer process (inset: graphene-coated CLs after transfer). (b) Optical image of the graphene (c) Average Raman Spectrum of 10 maps taken on the four different graphene-coated CLs.

Conductivity measurements

To further assess the quality and continuity of the graphene film after it was transferred to the lens, conductivity measurements would be ideal. Although tungsten needles were previously used for this

purpose, they were unsuccessful as they directly contacted the graphene, damaging it and resulting in unreliable measurements. To address this, an alternative approach was adopted, inspired by a published study [132], where silver paste was used as electrodes (Figure 28). Contrary to their results, no reliable measurements could be obtained as the silver paste proved to be toxic to the graphene-coated lens, as it pierced through the graphene, decomposed the CL material beneath it, and even affected the template.



Figure 28: Graphene-coated CL with four electrodes made of silver paste.

A different approach was then attempted, where gold (Au) was deposited onto the graphene using sputtering before the wet transfer process. To shape the electrodes, a shadow mask was placed on top of the graphene/copper (Gr/Cu) foil, thereby avoiding the use of polymers and patterning techniques that could complicate the process and introduce contaminants. Kapton tape was used to cover half of the mask as electrodes with different thicknesses were to be tested, 10nm and 30nm, because it was uncertain how this parameter would affect the graphene when transferring it (Figure 52a-b, Appendix X). Figure 52c (Appendix X) shows the Au electrodes after sputtering and the PMMA/Au electrode/Gr/CL right after scooping. No visible cracks were observed during the scooping step. After finishing the transfer process, conductivity measurements were done. Figure 52d-e (Appendix X) shows the setup utilized for these measurements using tungsten needles. Despite the presence of Au electrodes, which facilitate needle contact and prevent damage, the measured resistance was extremely high, in the order of MΩ. OM and Raman Spectroscopy were used to analyze the quality of the graphene near the Au electrodes.

Figure 53a (Appendix XI) shows an optical image of the 10nm deposited Au electrode/graphene-graphene interface, where clear discontinuity is visible. The 30nm Au electrodes also caused the same discontinuities on the interface with measurements showing that the graphene got damaged (Figure 53b-c Appendix XI). Figure 53d (Appendix XI) displays the graphene between the four electrodes, confirming that the graphene only cracked at the interface with the Au electrodes. This result is attributed to the strain induced by the electrodes during the wet transfer process. Unlike graphene, Au is not flexible which causes the graphene underneath to tear when transferred into the curve surface. To further confirm that the cracks and discontinuities were caused by the tension during the transfer, a transfer was conducted to flattened lens. The conductivity test showed a resistance between 5kΩ and 12kΩ. Figure 29 shows the setup for the measurement. This method enabled us to assess the conductivity of graphene on top of the CL, though replicating these measurements without flattening the CL remains a challenge.

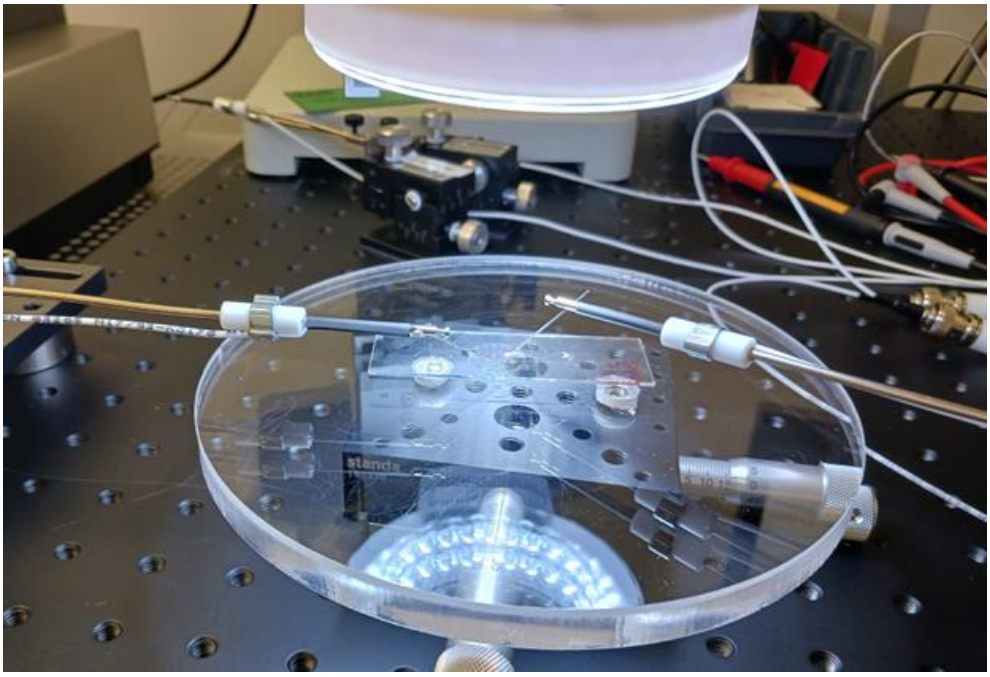


Figure 29: Setup for the measurement of the graphene conductivity with Au electrodes on top of a flattened CL.

Transmission and permeability measurement

The effect of the graphene film on the lenses was addressed as it is important to understand what changes could be caused to its intrinsic properties, such as its light transmission and permeability. It is known that single-layer graphene has an absorbance of about 2.3% of light in the visible wavelength range [51]. To test how our graphene affected the transmittance when transferred to CLs, UV-vis was utilized. For these measurements a bare and a graphene-coated CL were flattened on a glass coverslip. Figure 30a presents

the transmittance of both samples in the visible range, while Figure 30b highlights the difference between their spectra. In the 700 nm to 500 nm range, a transmittance difference of approximately 3% is observed, whereas in the 500 nm to 380 nm range, a decrease in transmittance is noted. This result further suggest that the integration of graphene into lenses will not affect clear vision during use.

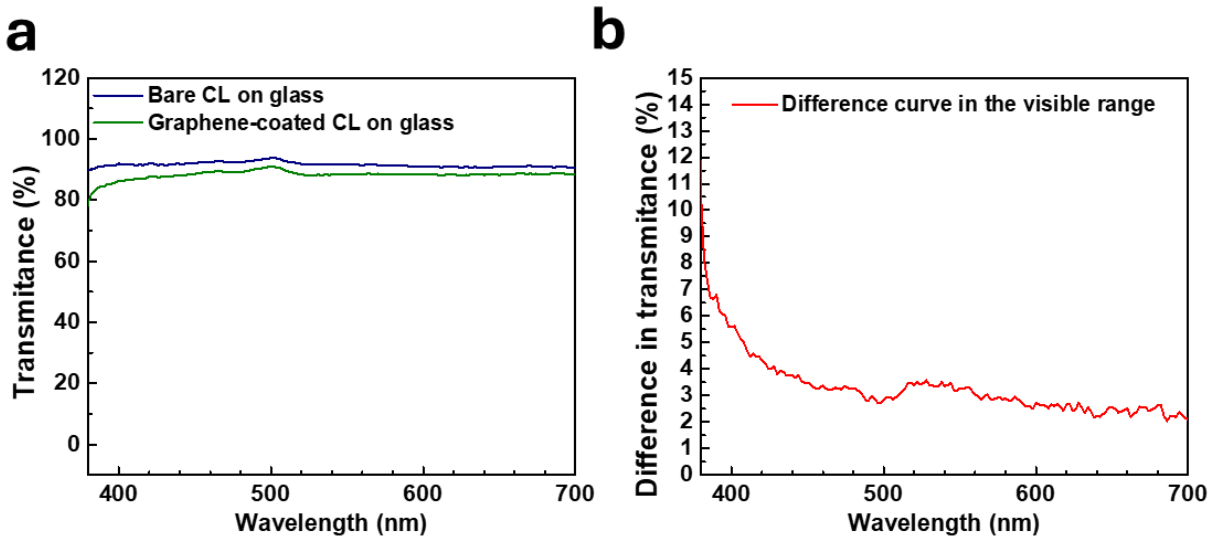


Figure 30: (a) Comparison of the optical transmittance between a graphene-coated CL and a bare CL and (b) Difference in percentage between both.

The permeability test was conducted, similar to the one done on a previous study [132], as it shown that graphene-coated CLs could have benefits for people with dry eye syndrome. In their study, two different vials with DI water were covered with bare and a graphene-coated CL, respectively. To prevent any leakages, adhesive tape was used to seal the vials. In a similar manner, silicone elastomer (Dowsil 3140 RTV) was spread on the border of each vial, as the adhesive tape was proved to not be effective, leaving opened zones as the CL dried. For the experiment, the two vials were placed on top of a hot plate at 38°, as shown in Figure 31a. Figure 31b shows the weight of each vial before and a duration of 7 days, indicating a clear trend but with no significant difference. The total weight loss for the vial sealed with a bare and graphene-coated CL were 0.6814 and 0.6718, respectively. The difference between both is not significant, suggesting that graphene does not negatively affect the permeability of the lens.

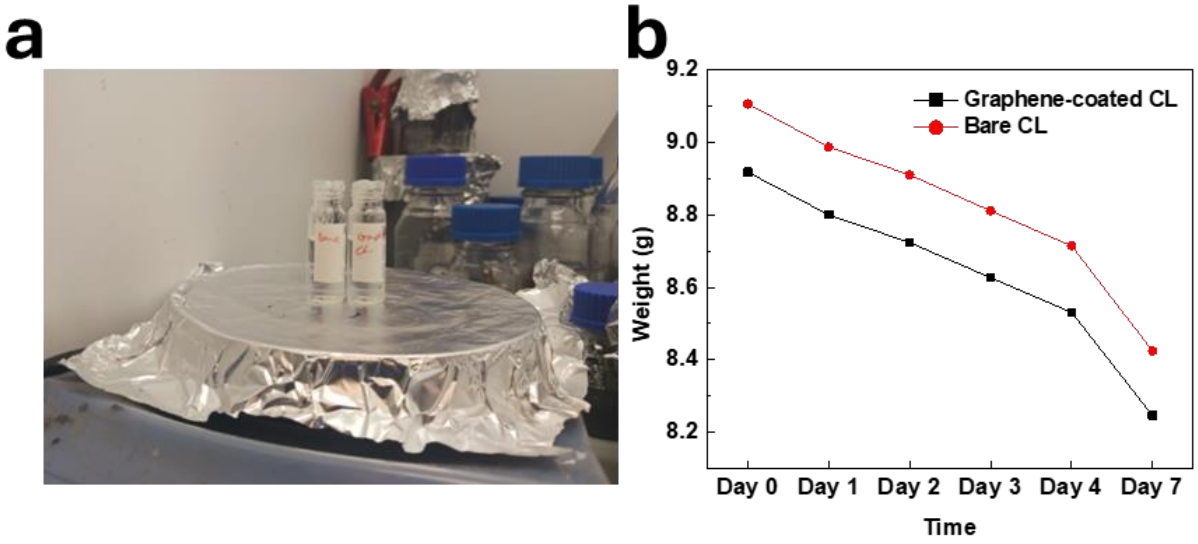


Figure 31: (a) Setup for the dehydration experiment. (b) Comparison of the weight loss between the vials sealed with a bare and a graphene-coated CL.

5.2 Graphene functionalization for glucose sensing

A key focus of this thesis was the development of a protocol to immobilize the enzyme on graphene-coated lenses, step toward the future integration of biosensing capabilities into contact lenses. Since contact lenses are typically made of silicon hydrogels, they are particularly sensitive to certain solvents. The conventional functionalization method often requires strong solvents, which could potentially damage the lens material. To address this challenge, various incubation methods were tested with different solvents. Initial functionalization attempts were performed using a small vial (Figure 32a), while later attempts were carried out using a CL container (Figure 32b). The incubation process was initially tested with DMF, a solvent commonly used for PBASE, but it was unsuccessful due to its high toxicity. DMSO was then considered as a substitute, but it also led to significant issues, such as the lens collapsing inwards when immersed in a PBASE solution (1 mM in DMSO). Additionally, a problem arose with the vial's walls causing the CLs to adhere to them, which may cause further damage to the graphene film.

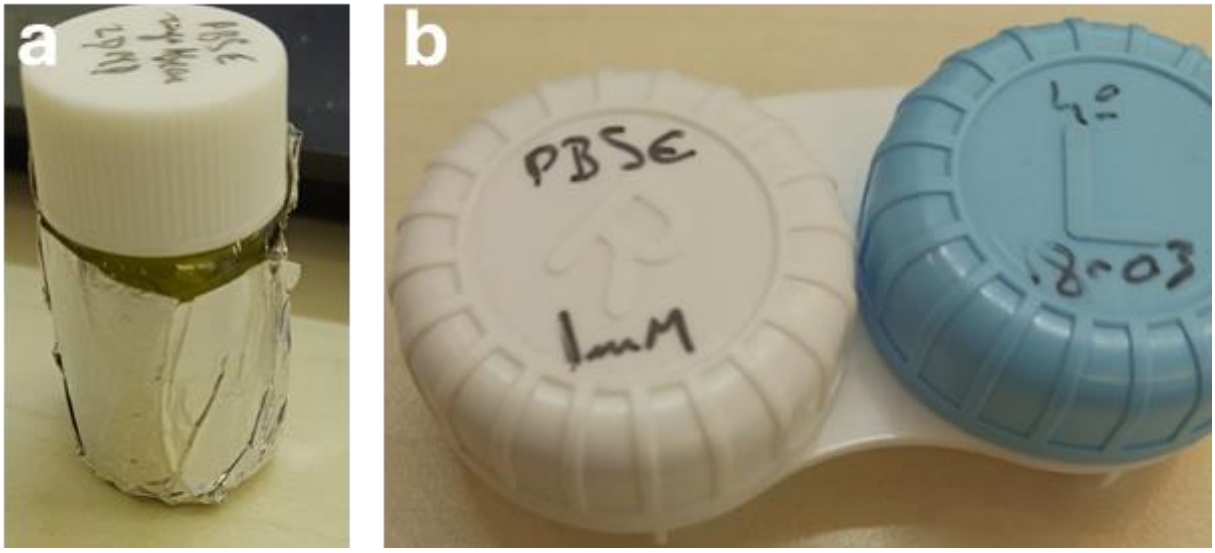


Figure 32: (a) Vial and (b) CL container utilized for functionalization.

Although the lens collapsed and became damaged, it was able to regain its original form after being placed in the saline solution used for storage. Figure 33 shows the graphene-coated CL after being incubated for 4 and 24 hours in the PBSE solution. These incubation times were selected because, unlike the conventional method of placing the solution directly on the graphene, in this experiment, the graphene-coated lens had to float on the solution. This alteration in the incubation approach raised concerns about whether it would result in poor interaction between the linker and the graphene, as this method had never been attempted before. Despite the lens being recoverable, as expected, the continuity of the graphene film was largely compromised during incubation. This process led to visible discontinuities and cracks in the graphene, with some areas of the film completely detached from the CL.

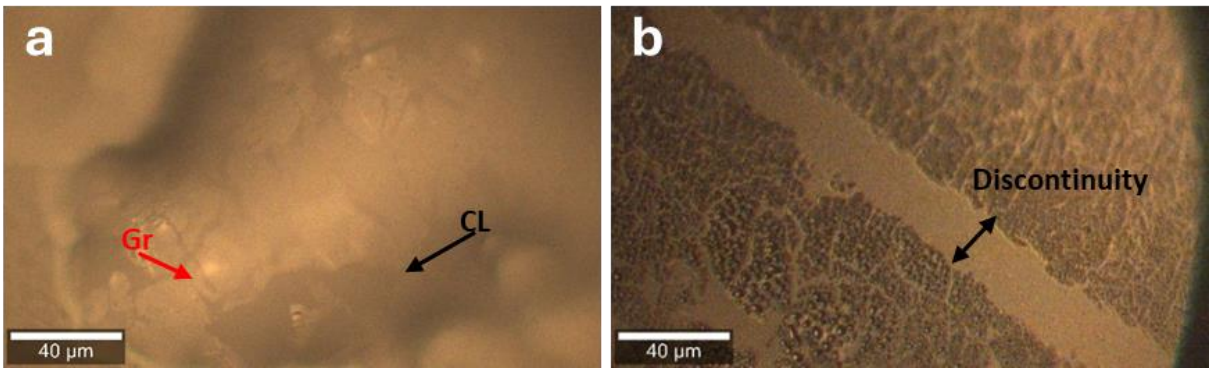


Figure 33: Microscopic images of the graphene after PBASE incubation.

Nevertheless, Raman spectroscopy was performed on the graphene patches on the CLs to assess the success of the functionalization process. Figure 34a-b presents the characterization of the PBASE using varying laser powers, up to 16 mW, for the two different incubation times, 4 and 24 hours respectively. After analyzing the data, it was clear that despite using high laser power, it was not possible to determine if the CL had been successfully functionalized with the linker, as its characteristic peaks did not appear. The high laser intensities used led to graphene damage, and to prevent any further burning effects in future characterizations, a control test was conducted. In this test, a CL was used to identify the maximum power the material could withstand. Multiple laser powers were tested, and it became evident that the burning effect appeared at laser intensities around 10 mW.

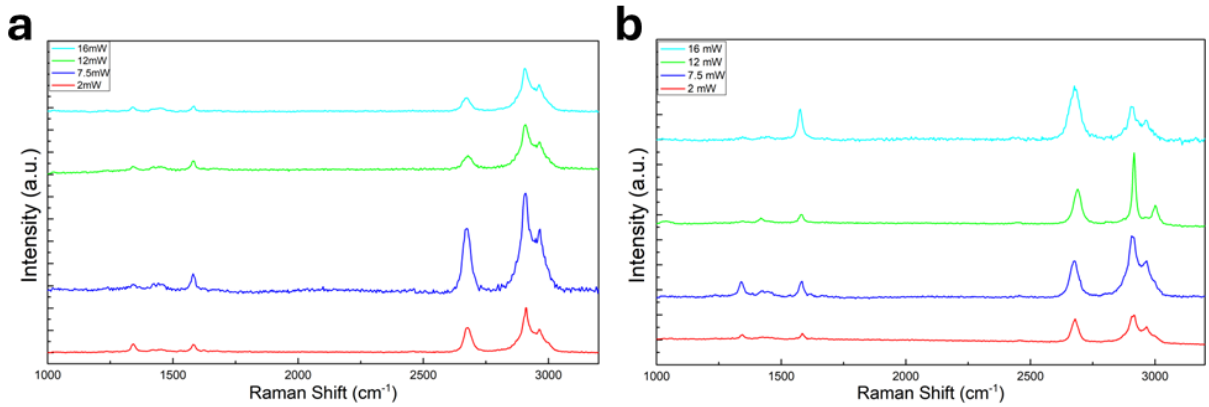


Figure 34: Raman Spectrum at different laser powers after (a) 4h incubation and (b) 1 day.

Although the signature PBASE peaks were not observed, it was hypothesized that the peaks from the CL itself might be interfering with the signal, as they contributed significantly to the spectrum. To further investigate, the incubation with GOx was carried out to detect any changes in the Raman spectra. After the 4-hour PBASE incubation, the CL was left to incubate in a 2 mL GOx solution for 24 hours. Figure 35a displays a microscopic image of the graphene on the CL surface, which, as anticipated, shows visible damage to the CL material. Figure 35b shows a small peak around 1231 cm^{-1}, which corresponds to the PBASE functionalization, suggesting that the linker coverage on the graphene was not uniform likely due to the damage caused during the functionalization process. Additionally, it became necessary to consider potential interactions between the container material and the solution, which could hinder proper functionalization. In conclusion, maintaining the continuity and quality of the graphene film is pivotal, and

further efforts must be made to eliminate any interactions between the PBASE solution and secondary materials.

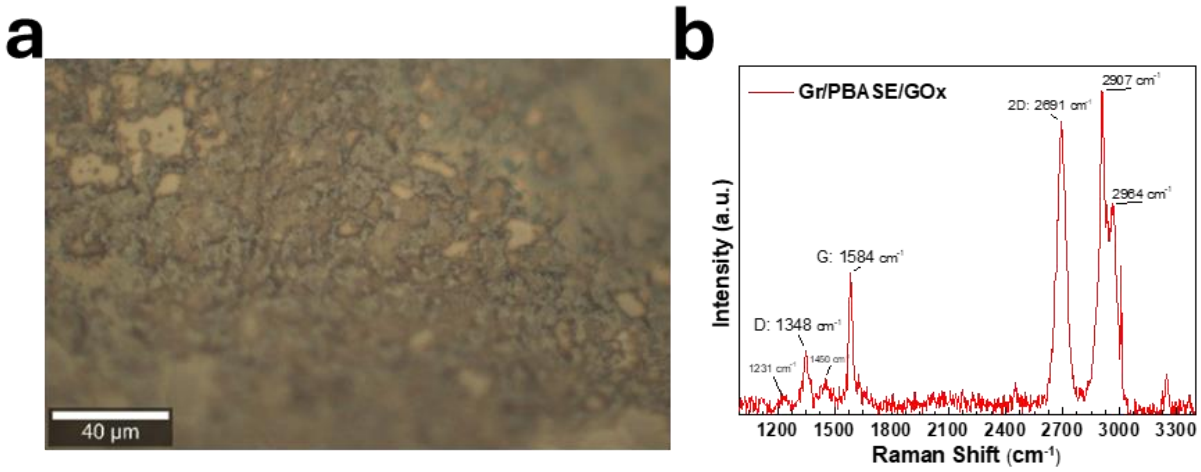


Figure 35: (a) Optical image of the graphene after GOx incubation and (b) Raman Spectrum.

5.2.1 Optimization procedure

To address the aforementioned issues, a new template similar to the one shown in Figure 26 was designed in AutoCAD and 3D printed in grey resin, specifically intended for integration with a vial (Figure 36a-b). It has the same radius as the lens ensuring full contact with the inner surface while leaving the graphene-coated side exposed. Additionally, it prevents possible unknown interactions with unwanted materials that may have occurred with the previous method and reduces the amount of solution needed to fully submerge the lens. To use this template, the graphene-coated lens is first placed on the semi-spheric part of the template (Figure 36c). Next, the required amount of solution (2 ml) is poured on the vial and the template with the lens is placed on top, acting as a lid (Figure 36d). Finally, the vial is gently flipped to ensure that the solution submerges the CL completely (Figure 36e).

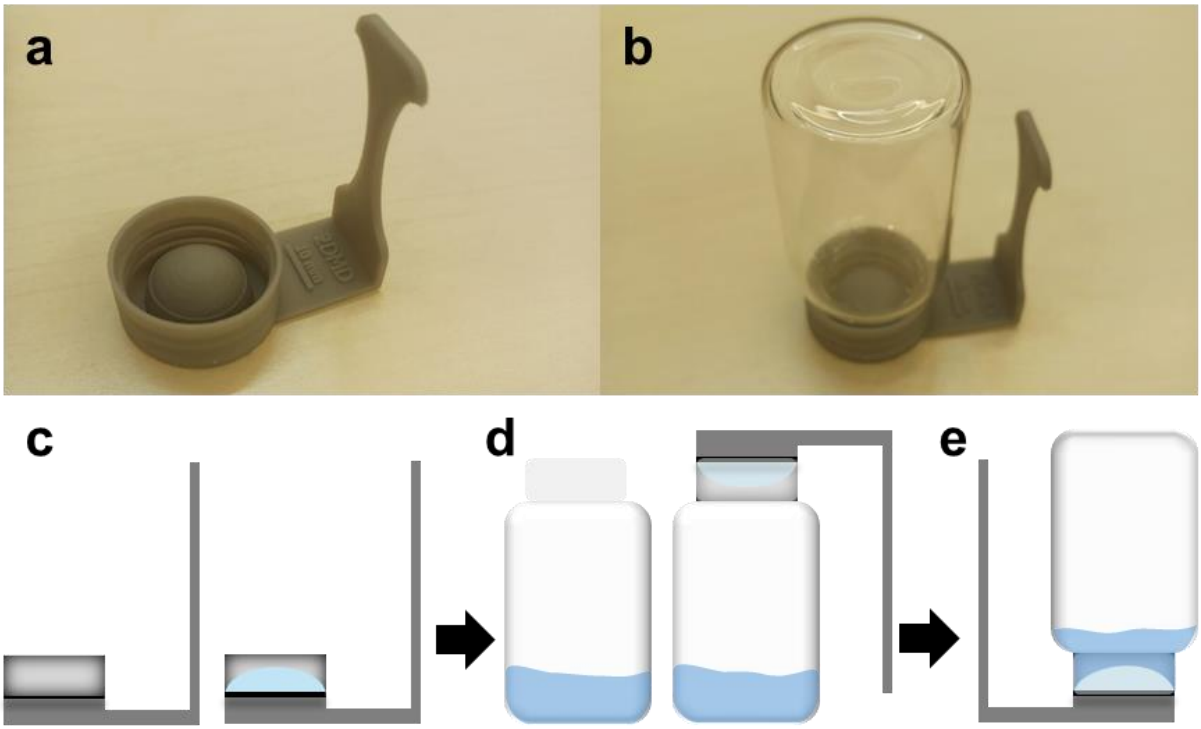


Figure 36: Template design for the functionalization of graphene on the CL surface (a) without the vial and (b) with the vial. The process for the functionalization is depicted from (c) to (e).

As the solvent was previously shown to be highly reactive, a dilution of DMSO with DI water was tested. The first experiment aimed to determine the optimal ratio between DMSO and DI water to prevent damage to the CLs and the graphene. Two different ratios, 3:1 and 1:1, were tested with a 2-hour incubation time. Neither dilution caused visible damage to the graphene or the CL. A problem arose when attempting to dilute the PBASE solution (in DMSO) with DI water: a white foam-like layer formed on the surface of the solution. This indicated that diluting PBASE in DMSO with water would lead to a reaction, potentially hindering proper immobilization. As a result, a control test was conducted where DMSO was applied directly to the CL. This also served to assess whether DMSO could induce any defects in the graphene during functionalization with PBASE. The CL was submerged in a DMSO solution for 2 hours, the standard incubation time for PBASE. Figures 37a-b show the graphene-coated CL before being submerged in DMSO, and Figures 37c-d show the same CL after the 2-hour incubation. By analyzing the optical images and Raman spectroscopy, it was concluded that, with the help of the template, the continuity and quality of the graphene were maintained. The template ensured that the inner side of the CL was in full contact

with the support, while the graphene on the outer side acted as a shielding layer against the solvent, preventing any damage to the material.

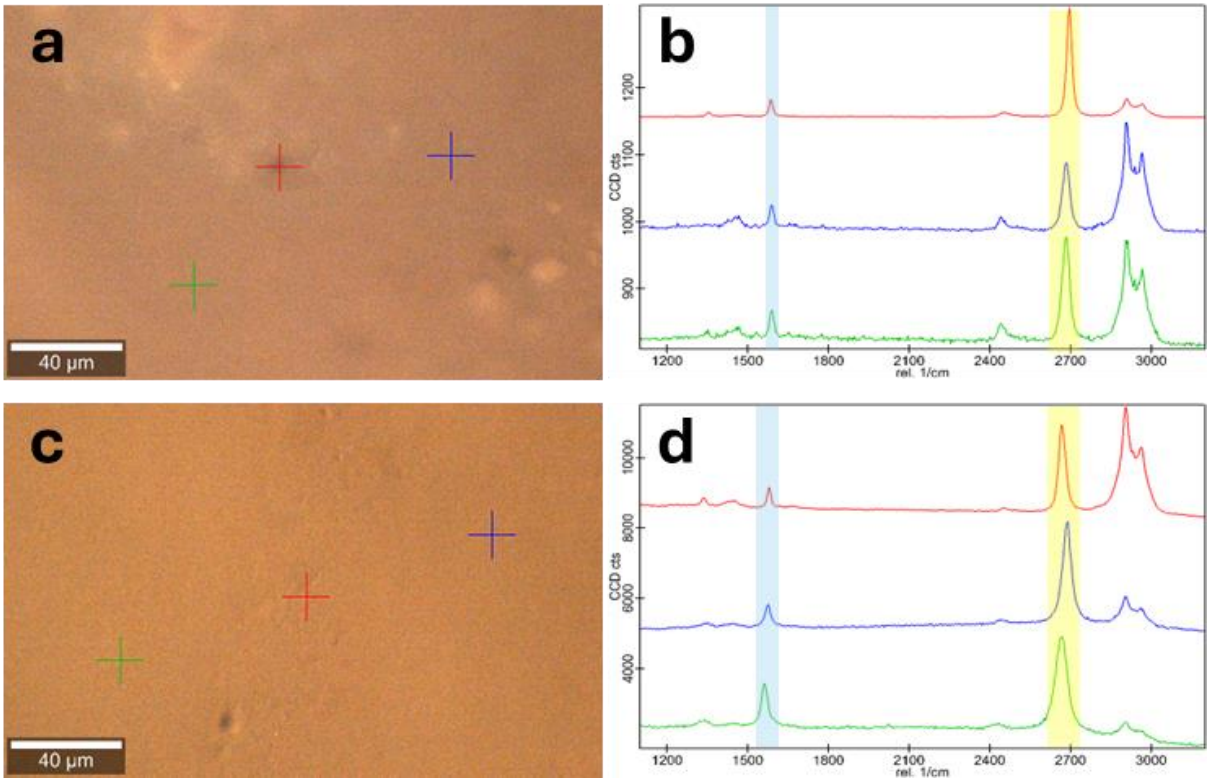


Figure 37: (a) Optical image of graphene-coated CL before being submerged in DMSO, with (b) its corresponding Raman spectra. (c) Optical image of graphene-coated CL after being submerged in DMSO, with (d) its corresponding Raman spectra.

The next step was to use the PBASE solution, but the same white foam appeared when it came into contact with the lens, likely due to the saline solution present on the surface. To address this issue, the lens was placed in the template and left to dry at room temperature for 1 hour to ensure that all the saline solution was removed before proceeding. After incubating for 2 hours on PBASE solution (10 mM in DMSO), the lens was first cleaned with DMSO followed by DI water. The cleaning was done with the lens still on the template and gently drop casting the liquids. Appendix XII displays two panels with Raman spectra taken from three random positions on the graphene-coated CL before and after functionalization. Notably, the appearance of a peak around 1234 cm^{-1} and the characteristic defect peaks were observed, both of which are associated with the PBASE immobilization. After successfully immobilizing the linker, a solution of glucose oxidase (20 mg in 2 ml of DI water) was used to immobilize the enzyme. From the previous chapter the Raman peaks of GOx were already known, and a challenge arises when analyzing

the functionalization as the peaks from the GOx and the CL overlap, making it difficult to conclusively determine successful immobilization. Additionally, since graphene is on a curved surface, comparing the shifts in the 2D and G peaks across just a few spectra could be misleading. The shifts may not only be due to functionalization but also could result from the mechanical strain induced by the curvature of the lens in different positions. Similarly to the method used for the characterization of graphene on a flat surface in the previous chapter, Raman maps were done, to distinguish the shift caused by mechanical strain and charge doping. Figure 38a shows an optical image of one of the areas selected for a Raman map (10 μm x 10 μm). Despite the curved surface of the lens, it was possible to obtain small maps without losing focus. For regions farther from the top, smaller maps were taken to avoid losing focus due to the lens curvature. Figure 38b shows the average of all Raman spectrums taken in the functionalization process. All the three spectra of Gr (as transferred), Gr/PBASE and Gr/PBASE/GOx show the typical features of high-quality, monolayer graphene, with a I_{2D}/I_G ratio of 5.28, 1.78 and 1.78, respectively. For comparison, graphene was also transferred onto a Si/SiO_2 substrate to conduct a parallel characterization, ensuring that any potential misinterpretation of the results could be avoided. The FWHM of the 2D peak slightly decreases from 30.61 cm^{-1} in Gr to 29.73 cm^{-1} in Gr/PBASE/GOx. On the other hand, an increase is observable on the G peak, going from 16.18 cm^{-1} for Gr to 19.26 cm^{-1} Gr/PBASE/GOx, similarly to the behavior of the graphene on the flat substrate (Appendix XIII). Figure 38c shows the plot of the 2D vs G peak positions of pristine graphene on both the lens and Si/SiO_2 substrate. It is noticeable that the shifts caused by each functionalization step display the same trend. Specifically, a blueshift is observed on the G and 2D peak in the PBASE step, indicating an increase in charge density as shown in Figure 38d, which further confirms that the pyrene molecules stacked on top of the graphene. A small redshift of the graphene peaks is observed when immobilizing GOx, indicating a decrease in charge density. These changes in the 2D and G peak positions confirm the successful binding of GOx to PBASE. A continuous increase in mechanical strain through the steps might be due to the interaction of the molecules with the graphene. The average values of each peak position and the peak shift caused by each step of the functionalization are shown in Appendix XIV, as well as the charge density and mechanical strain values.

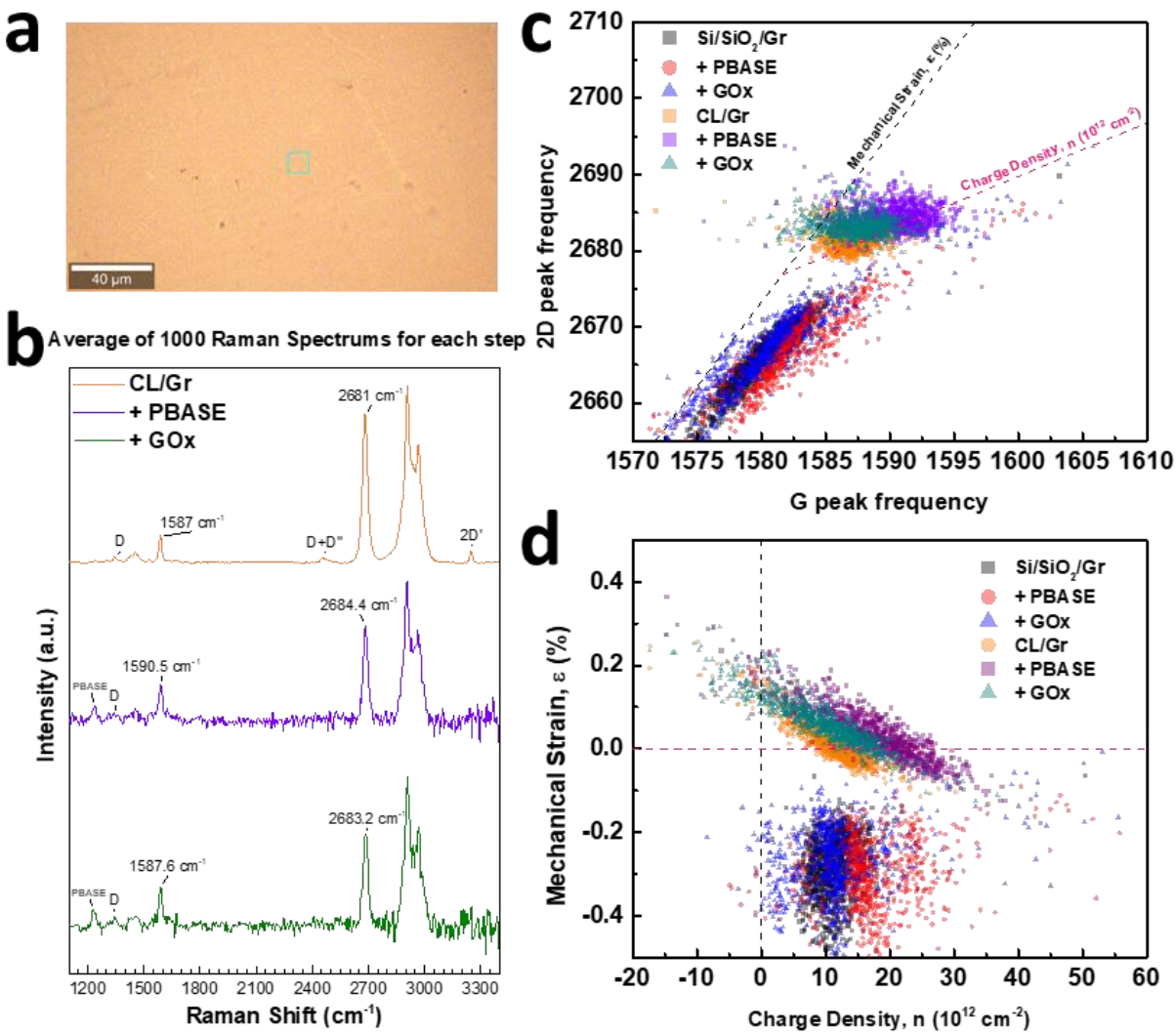


Figure 38: (a) Microscope Image of the graphene-coated lens and highlighted area of a map taken. (b) Raman spectra of each stage involved the immobilization of GOx molecules on graphene: pristine graphene (Gr, orange), PBASE modification (Gr/PBASE, violet) and GOx immobilization (Gr/PBASE/GOx, olive). Each spectrum is an average of 1000 measurements. (c) 2D vs G frequency plot of the 1000 measurements of Gr, Gr/PBASE and Gr/PBASE/GOx in both CL and Si/SiO_2. (The Gr, Gr/PBASE and Gr/PBASE/GOx of Si/SiO_2 correspond to the black, red and blue, respectively). (d) Mechanical strain (ε, %) vs charge (hole) density (n, 10^{12} cm^{-2}) plot of the measurements for each functionalization step in each substrate. The plot is a linear transformation of the 2D vs G frequency plot shown in Figure 38c.

Further analysis of the plots in Figure 38c-d reveals that the charge density on the lens is less uniform compared to the Si/SiO_2 substrates, with the data points being more dispersed. This discrepancy between the two surfaces may be attributed to the semi-spherical shape of the CL. Additionally, the initial mechanical strain values for the graphene on the CL differ from those on the Si/SiO_2 substrates.

Specifically, the graphene-coated lens exhibits an initial tensile strain, whereas the graphene on the Si/SiO_2 substrate shows compressive strain. Initially, it was thought that this difference might be due to the curved surface applying strain to the graphene, but Raman analysis on a flattened CL after graphene coating showed similar mechanical strain values to those observed on the graphene before flattening the lens. To rule out the possibility that graphene had retained the strain from the curved, a bare CL was first flattened on a coverslip, and then the graphene was transferred. Figure 39 presents the frequency plot of the 2D and G peaks of the graphene-coated CL under different conditions. The mechanical strain values of approximately ~0.0249% suggest that the observed difference between the graphene on the CL and Si/SiO_2 substrates. We hypothesized that this effect could be related to intrinsic characteristics of the substrates (*e.g.,* surface charge and flexibility) rather than the curvature of the lens as originally suspected.

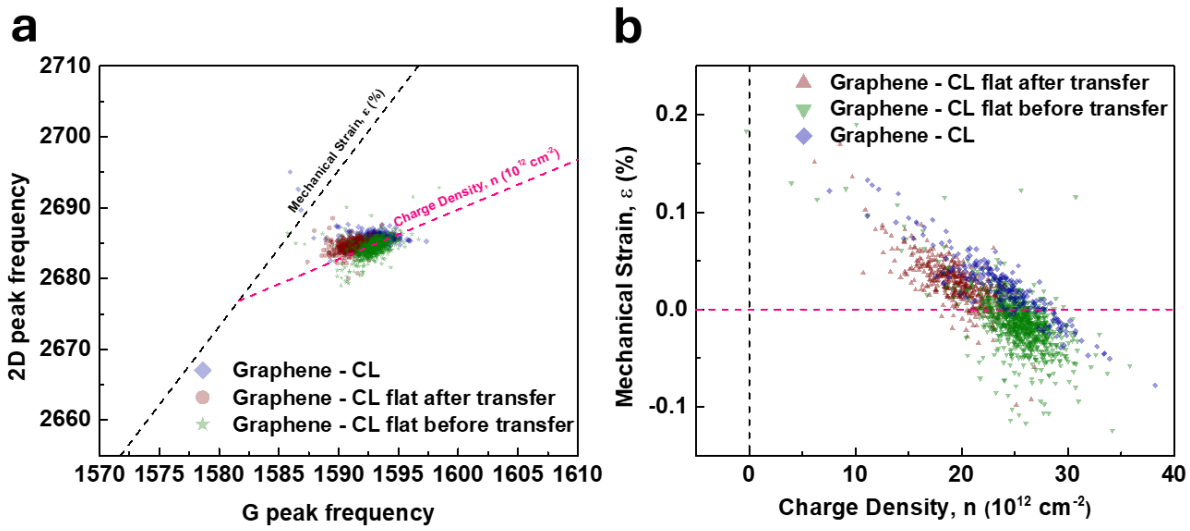


Figure 39: (a) 2D vs G frequency plot and (b) linear transformation with respect to the charge density and mechanical strain of 3 sets of points corresponding to Gr/CL. Each set of points are a combination of at least 500 measurements.

With a method for functionalizing the graphene-coated CLs now developed, it becomes possible to evaluate their hydrophilicity throughout all the steps of the functionalization process with GOx, using water contact angle (WCA) measurements. To establish a reference for the wettability of the CVD graphene, functionalization steps were performed in parallel using Si/SiO_2 substrates. For this type of measurement, the lens needs to be flattened to ensure accurate results. One potential issue encountered during measurement was the uncontrolled dehydration of the CL due to exposure to air. This could lead to

alterations in the contact angle, thus affecting the accuracy of the results. Figure 40 shows the WCA measurements of a bare CL, labeled as 'Baseline,' as well as two subsequent measurements taken at different times following the baseline. After two weeks and one month, the hydrophilic properties of the CL were maintained, with a contact angle around 30 degrees regardless of the time that had passed. The inset of Figure 40 displays one of these measurements, confirming that the CL surface was flat, and the droplet remained unaffected during the test.

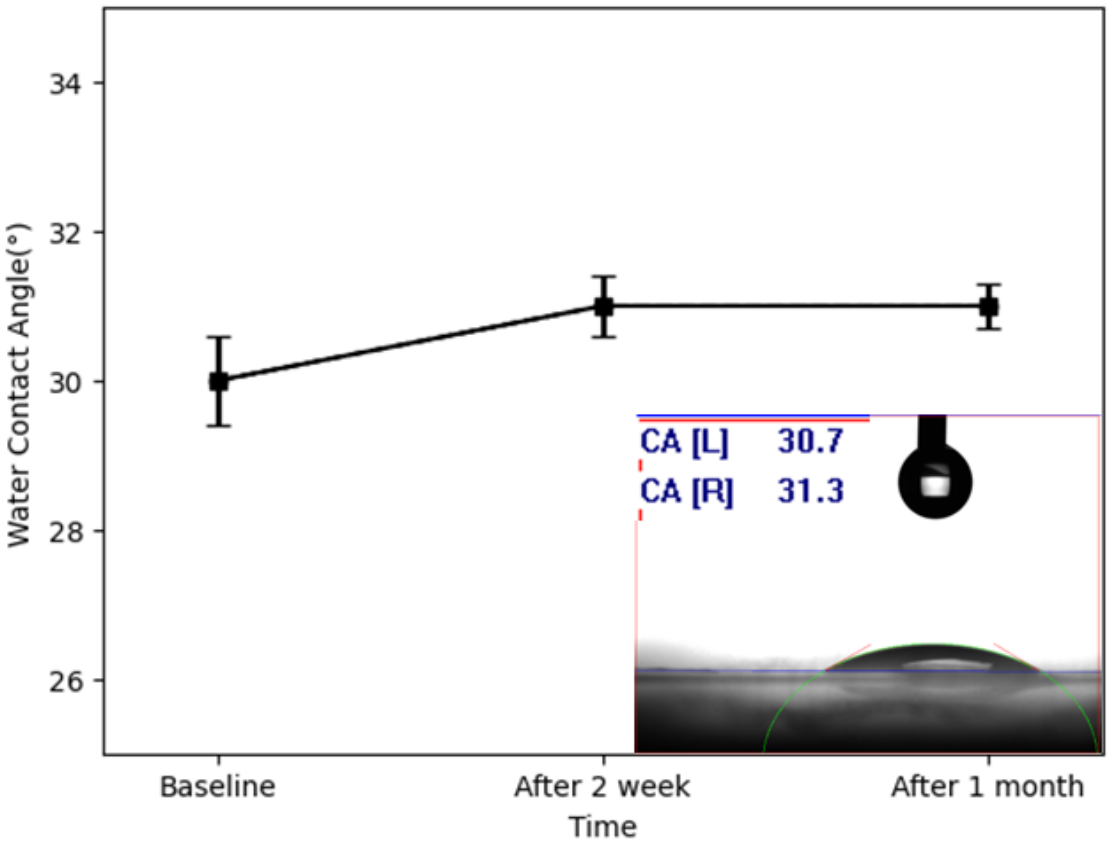


Figure 40: Average WCA measurements over time (inset: one of the measurements).

For the characterization of the functionalization steps, one CL was utilized for each step. Figure 41 shows the WCA measurements in each step starting from the bare lens. It is possible to see that the graphene had a big impact on the wettability characteristics, increasing the WCA by 59° in respect to the bare lens (Figure 41a). The immobilization of PBASE caused a decrease of ~14° and the further immobilization of GOx caused an increase of ~5° compared to the PBASE step. As these results were never shown, we proceeded to the characterization of the functionalization process using a Si/SiO_2 substrate. Figure 41b depicts the evolution of the WCA after the functionalization stages. The WCA of Gr (82.07°) increases by ~ 9° with respect to the Si/SiO_2 substrate (73.53°). The PBASE brings the WCA to lower values, 77.41°,

as expected by NHS-ester ligands upon surface immobilization [136]. The immobilization of GOx, a natively hydrophilic molecule, significantly decreased the WCA by ~23°. Furthermore, charge doping (either n- or p-type) has been shown to increase the wettability of graphene [204], [205], which would also sustain the successive decreases of graphene's WCA after functionalization with PBASE and GOx. Contrary to Si/SiO_2 substrate, an increase by ~4° was seen in the last functionalization step of the CL. This discrepancy can be attributed to the fact that it is not feasible to take the three measurements using the same graphene-coated CL. Once the CL is flattened on top of a coverslip, it would require submerging it in a solution to ensure the graphene is fully covered. However, this would cause the CL to detach, potentially damaging both the graphene and the CL material itself. This experiment were not repeated because we obtained always different graphene contact angles, and even though they were similar the small differences could lead to inconclusive results.

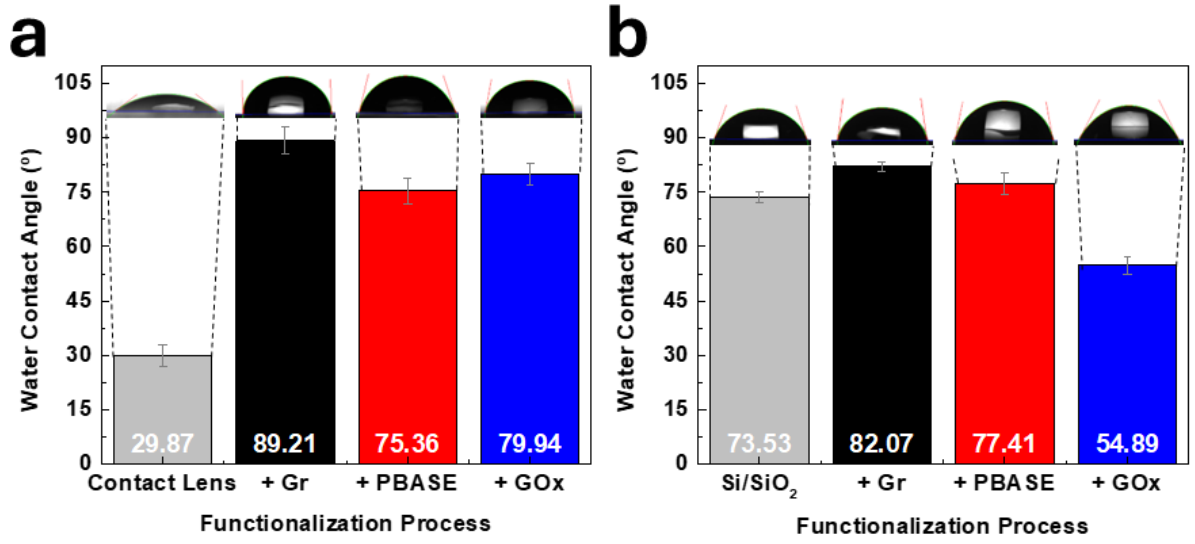


Figure 41: WCA characterization of the functionalization process (a) in CLs and (b) Si/SiO_2 substrate.

To further confirm the proper functionalization on the graphene, UV-vis spectroscopy was employed. Using the template for the functionalization process, a fully functionalized graphene-coated lens was submerged in a solution of 5 ml of glucose (1mM, in PBS 1X). After 5 minutes the solution was transferred to another vial so we could insert it on the UV-vis. As a reference, the original glucose solution (1mM, PBS 1X) was used, this approach would allow for the monitoring of any optical changes that could indicate the interaction between the functionalized graphene and glucose. Figure 42a displays the molecular absorption spectrum in the range of 200 nm–270 nm, which can be attributed to byproducts of the interaction between glucose and GOx. To investigate whether the observed peak originated from H_2O_2, an experiment was conducted where different concentrations of H_2O_2 were diluted in PBS, using PBS as

a reference (Appendix XV), which goes according with literature [206]. This experiment confirmed the contribution of H_2O_2 to the spectrum. Calibration curves were created to quantify the amount of H_2O_2 produced in the glucose-GOx reaction. Figure 42b shows various molecular absorption curves obtained by drop-casting different volumes of H_2O_2 (30%) into 3 ml of glucose (1 mM in 1X PBS). Upon comparing both graphs, the curve in Figure 42a closely resembles the one generated by adding 2.5 µL of H_2O_2, further confirming the presence and activity of the enzyme on the graphene-coated CL. Other byproducts from the glucose-GOx reaction might also contribute to the spectrum shown in Figure 42a, which could potentially lead to misleading results. Thus, additional experiments will be required to identify and quantify the other molecules involved in the reaction. Figure 42b correlates well with the graph in Appendix XV, as when adding 1 µL of H_2O_2 to the 3 ml solution (resulting in a concentration of 0.01%) yields a similar spectrum to the one corresponding to a concentration of 0.01%. The last volume measured (3.5 µL) corresponds to a concentration of 0.035%, making the results coherent as the spectrums fall within the concentration range of 0.01% to 0.05%.

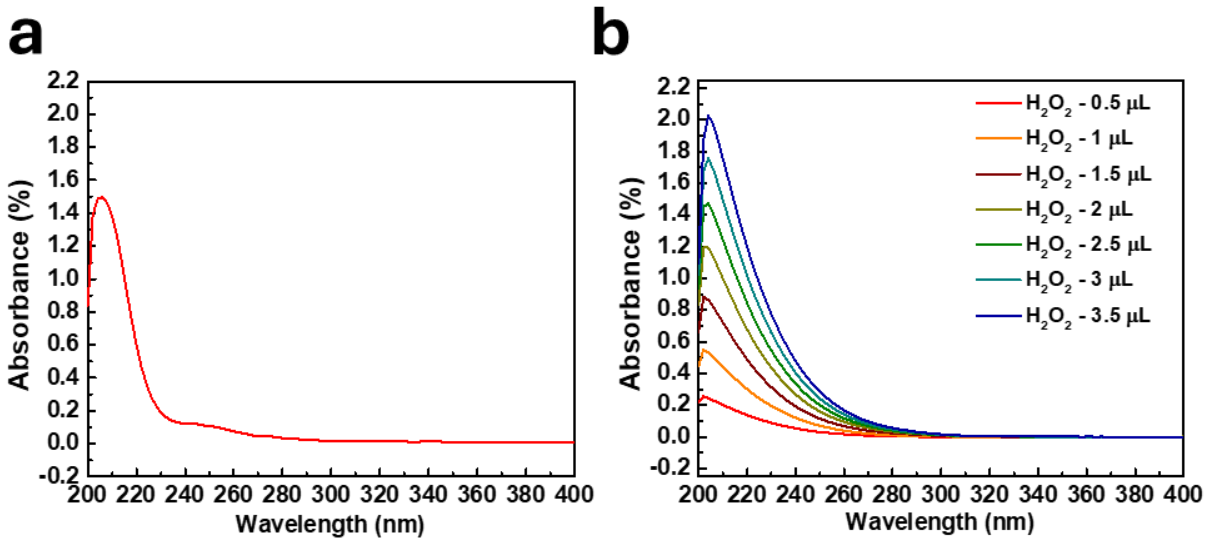


Figure 42: (a) Molecular absorption spectrum of 1 mM glucose solution after reacting with the fully functionalized CL. (b) Molecular absorption spectrum different concentrations of H_2O_2. In both spectrums glucose (1 mM in 1 x PBS) was utilized as reference.

5.3 Conclusion and future outlook

In this chapter, we explored the integration of monolayer CVD graphene in contact lenses. Different characterization techniques were used to evaluate the characteristics of graphene and potential

modifications induced during the fabrication method. This includes an assessment of the quality, morphology, continuity, number of layers and any potential chemical modification. The initial transfer procedure often resulted in defective graphene coating due to the difficulty of transferring graphene to 3D surfaces. These issues arise from the high precision required to scoop out the PMMA/Gr from the water to the lenses, while making sure that the whole surface is covered by graphene. The size of the PMMA/Gr also influences the outcome of the transfer. If film size is not correctly dimensioned to match the lens diameter, excessive tension may happen during scooping, increasing the risk of rupture upon contact with the lens. To solve these issues, the transfer process was specifically optimized. A sample holder was designed in AutoCAD and 3D-printed with synthetic resin to facilitate the graphene transfer to the lenses while scaling up the number of transfers, making it an easier and less time-consuming procedure. A method to assess the electrical properties of graphene was attempted by sputtering gold electrodes directly onto the graphene film, avoiding complex lithography techniques that could introduce contamination and affect the measurements. Following the integration of the graphene coating in the contact lenses, we studied the functionalization protocol needed for glucose detection. An additional sample holder dedicated to liquid experiment was designed and 3D-printed. This setup allows us to fully submerge the graphene-coated lens in a controlled liquid environment to chemically modify graphene without deteriorating the hydrogel lens. The successful immobilization of glucose oxidase was proved by Raman spectroscopy. Finally, the reaction of glucose with the fully functionalized lens was verified using ultraviolet-visible spectroscopy, by confirming the presence of hydrogen peroxide. Although an attempt was made to quantify the amount produced, the contributions from the other byproducts of the reaction must be taken into account for a definitive measurement.

Within the timeframe of this project, a way to directly correlate the response of the functionalized graphene on contact lenses to glucose with the V_{DIRAC} shifts observed in EG-GFETs during the glucose detection was out of reach. Future work should thus attempt to bridge this gap. In our view, two main routes might be explored. (i) Further experiments on EG-GFETs sensing under different conditions (*e.g.*, pH and temperature) would extend the current understanding of the detection mechanism. (ii) Accelerated experiments with a blink simulator would provide useful information on the mechanical stability and durability of the graphene coating in simulated conditions. (iii) Detailed UV-Vis measurements tracking the additional byproducts of the glucose-GOx reaction (*e.g.*, gluconolactone and gluconic acid) would aid an exact quantification of the H_2O_2 concentration produce during the detection, potentially leading to a fruitful correlation with the V_{DIRAC} shifts observed in analogous conditions in the EG-GFETs. In the future,

these additional experiments could pave the way to the realization of graphene-based disposable contact lenses, which could predictively react to specific concentration of glucose in tears while worn and then measure by a portable device once removed.

REFERENCES

[1] A. S. AlMajali, T. Richards, S. W. Yusuf, and B. Telgenkamp, "Vascular service provision during the COVID-19 pandemic worsened major amputation rates in socially deprived diabetic populations," *Front Endocrinol (Lausanne)*, vol. 15, p. 1304436, 2024.

[2] H. Tsutsui, G. Tanaka, and K. Kondo, "Diabetes Mellitus," in *Social Determinants of Health in Non-communicable Diseases: Case Studies from Japan*, K. Kondo, Ed., Singapore: Springer Singapore, 2020, pp. 73–86. doi: 10.1007/978-981-15-1831-7_8.

[3] A. D. Association, "Diagnosis and classification of diabetes mellitus," *Diabetes Care*, vol. 33, no. Supplement_1, pp. S62–S69, 2010.

[4] D. Bruen, C. Delaney, L. Florea, and D. Diamond, "Glucose sensing for diabetes monitoring: recent developments," *Sensors*, vol. 17, no. 8, p. 1866, 2017.

[5] P. Gong *et al.*, "Optical fiber sensors for glucose concentration measurement: A review," *Opt Laser Technol*, vol. 139, p. 106981, 2021.

[6] J. Kim, M. Khan, and S.-Y. Park, "Glucose sensor using liquid-crystal droplets made by microfluidics," *ACS Appl Mater Interfaces*, vol. 5, no. 24, pp. 13135–13139, 2013.

[7] S. Viswanathan *et al.*, "Graphene–protein field effect biosensors: glucose sensing," *Materials Today*, vol. 18, no. 9, pp. 513–522, 2015.

[8] H. Teymourian, A. Barfidokht, and J. Wang, "Electrochemical glucose sensors in diabetes management: an updated review (2010–2020)," *Chem Soc Rev*, vol. 49, no. 21, pp. 7671–7709, 2020.

[9] G. Wang *et al.*, "Non-enzymatic electrochemical sensing of glucose," *Microchimica Acta*, vol. 180, pp. 161–186, 2013.

[10] L. Wei *et al.*, "Ultrasensitive Non-Enzymatic glucose sensors based on hybrid reduced graphene oxide and carbonized silk fabric electrodes decorated with Cu Nanoflowers," *J Electrochem Soc*, vol. 167, no. 12, p. 127501, 2020.

[11] M. Q. Guo, H. S. Hong, X. N. Tang, H. D. Fang, and X. H. Xu, "Ultrasonic electrodeposition of platinum nanoflowers and their application in nonenzymatic glucose sensors," *Electrochim Acta*, vol. 63, pp. 1–8, 2012.

[12] P. Karami, A. Babapoor, B. M. Shoghi, and A. M. Johari, "Comparison of Electrochemical Enzymatic and Non-enzymatic Glucose Sensors Based on Literature Review," 2021.

[13] H. Zhu, L. Li, W. Zhou, Z. Shao, and X. Chen, "Advances in non-enzymatic glucose sensors based on metal oxides," *J Mater Chem B*, vol. 4, no. 46, pp. 7333–7349, 2016.

[14] N. Miya, L. F. E. Machogo-Phao, and B. Ntsendwana, "Exploring Copper Oxide and Copper Sulfide for Non-Enzymatic Glucose Sensors: Current Progress and Future Directions," *Micromachines (Basel)*, vol. 14, no. 10, p. 1849, 2023.

[15] H. Lee, Y. J. Hong, S. Baik, T. Hyeon, and D. Kim, "Enzyme-based glucose sensor: from invasive to wearable device," *Adv Healthc Mater*, vol. 7, no. 8, p. 1701150, 2018.

[16] I. Kim, C. Kim, D. Lee, S. W. Lee, G. Lee, and D. S. Yoon, "A bio-inspired highly selective enzymatic glucose sensor using a red blood cell membrane," *Analyst*, vol. 145, no. 6, pp. 2125–2132, 2020.

[17] L. Johnston, G. Wang, K. Hu, C. Qian, and G. Liu, "Advances in biosensors for continuous glucose monitoring towards wearables," *Front Bioeng Biotechnol*, vol. 9, p. 733810, 2021.

[18] B. Solnica, J. W. Naskalski, and J. Sieradzki, "Analytical performance of glucometers used for routine glucose self-monitoring of diabetic patients," *Clinica Chimica Acta*, vol. 331, no. 1–2, pp. 29–35, 2003.

[19] A. Shlomowitz and M. D. Feher, "Anxiety associated with self monitoring of capillary blood glucose," *British Journal of Diabetes*, vol. 14, no. 2, pp. 60–63, 2014.

[20] D. K. Sen and G. S. Sarin, "Tear glucose levels in normal people and in diabetic patients.," *Br J Ophthalmol*, vol. 64, no. 9, p. 693, 1980.

[21] D. B. Sacks *et al.*, "Guidelines and recommendations for laboratory analysis in the diagnosis and management of diabetes mellitus," *Clin Chem*, vol. 69, no. 8, pp. 808–868, 2023.

[22] J. D. Lane, D. M. Krumholz, R. A. Sack, and C. Morris, "Tear glucose dynamics in diabetes mellitus," *Curr Eye Res*, vol. 31, no. 11, pp. 895–901, 2006.

[23] I. S. Kim, H. T. Kim, E.-J. Kim, and E. J. Lee, "A comparative study of the concentration of salivary and blood glucose in normal and diabetic subjects," *Biomedical Science Letters*, vol. 19, no. 2, pp. 105–111, 2013.

[24] A. C. U. Vasconcelos, M. S. M. Soares, P. C. Almeida, and T. C. Soares, "Comparative study of the concentration of salivary and blood glucose in type 2 diabetic patients," *J Oral Sci*, vol. 52, no. 2, pp. 293–298, 2010.

[25] A. Béraud, M. Sauvage, C. M. Bazán, M. Tie, A. Bencherif, and D. Bouilly, "Graphene field-effect transistors as bioanalytical sensors: Design, operation and performance," *Analyst*, vol. 146, no. 2, pp. 403–428, 2021.

[26] M. Abrantes *et al.*, "Ultrasensitive dopamine detection with graphene aptasensor multitransistor arrays," *J Nanobiotechnology*, vol. 20, no. 1, Dec. 2022, doi: 10.1186/s12951-022-01695-0.

[27] J. Peña-Bahamonde, H. N. Nguyen, S. K. Fanourakis, and D. F. Rodrigues, "Recent advances in graphene-based biosensor technology with applications in life sciences," *J Nanobiotechnology*, vol. 16, pp. 1–17, 2018.

[28] Y. Song, Y. Luo, C. Zhu, H. Li, D. Du, and Y. Lin, "Recent advances in electrochemical biosensors based on graphene two-dimensional nanomaterials," *Biosens Bioelectron*, vol. 76, pp. 195–212, 2016.

[29] Y. Bai, T. Xu, and X. Zhang, "Graphene-based biosensors for detection of biomarkers," *Micromachines (Basel)*, vol. 11, no. 1, p. 60, 2020.

[30] I. Fakih *et al.*, "Selective ion sensing with high resolution large area graphene field effect transistor arrays," *Nat Commun*, vol. 11, no. 1, p. 3226, 2020.

[31] G. Wu *et al.*, "Graphene field-effect transistors for the sensitive and selective detection of Escherichia coli using pyrene-tagged DNA aptamer," *Adv Healthc Mater*, vol. 6, no. 19, p. 1700736, 2017.

[32] M. Abrantes *et al.*, "Ultrasensitive dopamine detection with graphene aptasensor multitransistor arrays," *J Nanobiotechnology*, vol. 20, no. 1, p. 495, 2022.

[33] R. C. Tseng, C. C. Chen, S. M. Hsu, and H. S. Chuang, "Contact-lens biosensors," Aug. 13, 2018, *MDPI AG*. doi: 10.3390/s18082651.

[34] M. Elsherif, R. Moreddu, F. Alam, A. E. Salih, I. Ahmed, and H. Butt, "Wearable Smart Contact Lenses for Continual Glucose Monitoring: A Review," *Front Med (Lausanne)*, vol. 9, 2022, doi: 10.3389/fmed.2022.858784.

[35] J. Kim, E. Cha, and J. U. Park, "Recent Advances in Smart Contact Lenses," Jan. 01, 2020, *Wiley-Blackwell*. doi: 10.1002/admt.201900728.

[36] J. Kim *et al.*, "Wearable smart sensor systems integrated on soft contact lenses for wireless ocular diagnostics," *Nat Commun*, vol. 8, 2017, doi: 10.1038/ncomms14997.

[37] H. Seo *et al.*, “Smart Contact Lenses as Wearable Ophthalmic Devices for Disease Monitoring and Health Management,” Oct. 11, 2023, *American Chemical Society*. doi: 10.1021/acs.chemrev.3c00290.

[38] J. Xu, X. Tao, X. Liu, and L. Yang, “Wearable Eye Patch Biosensor for Noninvasive and Simultaneous Detection of Multiple Biomarkers in Human Tears,” *Anal Chem*, vol. 94, no. 24, pp. 8659–8667, Jun. 2022, doi: 10.1021/acs.analchem.2c00614.

[39] H. Seo *et al.*, “Smart Contact Lenses as Wearable Ophthalmic Devices for Disease Monitoring and Health Management,” Oct. 11, 2023, *American Chemical Society*. doi: 10.1021/acs.chemrev.3c00290.

[40] N. Thomas, I. Lähdesmäki, and B. A. Parviz, “A contact lens with an integrated lactate sensor,” *Sens Actuators B Chem*, vol. 162, no. 1, pp. 128–134, Feb. 2012, doi: 10.1016/j.snb.2011.12.049.

[41] N. L. Kazanskiy, S. N. Khonina, and M. A. Butt, “Smart Contact Lenses—A Step towards Non-Invasive Continuous Eye Health Monitoring,” Oct. 01, 2023, *Multidisciplinary Digital Publishing Institute (MDPI)*. doi: 10.3390/bios13100933.

[42] X. Ma *et al.*, “Smart Contact Lenses for Biosensing Applications,” *Advanced Intelligent Systems*, vol. 3, no. 5, p. 2000263, 2021, doi: https://doi.org/10.1002/aisy.202000263.

[43] M. Yuan, R. Das, E. Mcglynn, R. Ghannam, Q. H. Abbasi, and H. Heidari, “Wireless Communication and Power Harvesting in Wearable Contact Lens Sensors,” *IEEE Sens J*, vol. 21, no. 11, pp. 12484–12497, Jun. 2021, doi: 10.1109/JSEN.2021.3055077.

[44] K. S. Novoselov *et al.*, “Electric Field Effect in Atomically Thin Carbon Films,” Kluwer, 2004. [Online]. Available: www.arXiv.org/quant-ph/

[45] A. K. Geim, “Graphene: Status and Prospects,” *Science (1979)*, vol. 324, no. 5934, pp. 1530–1534, Jun. 2009, doi: 10.1126/science.1158877.

[46] A. H. Castro Neto, F. Guinea, N. M. R. Peres, K. S. Novoselov, and A. K. Geim, “The electronic properties of graphene,” *Rev Mod Phys*, vol. 81, no. 1, pp. 109–162, Jan. 2009, doi: 10.1103/RevModPhys.81.109.

[47] F. Bonaccorso, Z. Sun, T. Hasan, and A. C. Ferrari, “Graphene photonics and optoelectronics,” *Nat Photonics*, vol. 4, no. 9, pp. 611–622, 2010, doi: 10.1038/nphoton.2010.186.

[48] P. Avouris, “Graphene: Electronic and photonic properties and devices,” Nov. 10, 2010. doi: 10.1021/nl102824h.

[49] D. G. Papageorgiou, I. A. Kinloch, and R. J. Young, "Mechanical properties of graphene and graphene-based nanocomposites," Oct. 01, 2017, *Elsevier Ltd*. doi: 10.1016/j.pmatsci.2017.07.004.

[50] C. Lee, X. Wei, J. W. Kysar, and J. Hone, "Measurement of the Elastic Properties and Intrinsic Strength of Monolayer Graphene," *Science (1979)*, vol. 321, no. 5887, pp. 385–388, 2008, doi: 10.1126/science.1157996.

[51] R. R. Nair *et al.*, "Fine Structure Constant Defines Visual Transparency of Graphene," *Science (1979)*, vol. 320, no. 5881, p. 1308, 2008, doi: 10.1126/science.1156965.

[52] M. Sang, J. Shin, K. Kim, and K. J. Yu, "Electronic and thermal properties of graphene and recent advances in graphene based electronics applications," Mar. 01, 2019, *MDPI AG*. doi: 10.3390/nano9030374.

[53] J. Wang, J. Song, X. Mu, and M. Sun, "Optoelectronic and photoelectric properties and applications of graphene-based nanostructures," Jun. 01, 2020, *Elsevier Ltd*. doi: 10.1016/j.mtphys.2020.100196.

[54] P. Avouris and F. Xia, "Graphene applications in electronics and photonics," Nov. 2012. doi: 10.1557/mrs.2012.206.

[55] X. Miao *et al.*, "High efficiency graphene solar cells by chemical doping," *Nano Lett*, vol. 12, no. 6, pp. 2745–2750, Jun. 2012, doi: 10.1021/nl204414u.

[56] P. You, Z. Liu, Q. Tai, S. Liu, and F. Yan, "Efficient Semitransparent Perovskite Solar Cells with Graphene Electrodes," *Advanced Materials*, vol. 27, no. 24, pp. 3632–3638, Jun. 2015, doi: 10.1002/adma.201501145.

[57] S. R. C. Vivekchand, C. Sekhar, A. Govindaraj, and R. Rao, "Graphene-based electrochemical supercapacitors," 2008.

[58] J. J. Yoo *et al.*, "Ultrathin planar graphene supercapacitors," *Nano Lett*, vol. 11, no. 4, pp. 1423–1427, Apr. 2011, doi: 10.1021/nl200225j.

[59] N. A. Kumar and J. B. Baek, "Doped graphene supercapacitors," *Nanotechnology*, vol. 26, no. 49, Nov. 2015, doi: 10.1088/0957-4484/26/49/492001.

[60] F. Xia, T. Mueller, Y. Lin, A. Valdes-Garcia, and P. Avouris, "Ultrafast graphene photodetector," *Nat Nanotechnol*, vol. 4, no. 12, pp. 839–843, 2009, doi: 10.1038/nnano.2009.292.

[61] C. H. Liu, Y. C. Chang, T. B. Norris, and Z. Zhong, "Graphene photodetectors with ultra-broadband and high responsivity at room temperature," *Nat Nanotechnol*, vol. 9, no. 4, pp. 273–278, 2014, doi: 10.1038/nnano.2014.31.

[62] A. Béraud, M. Sauvage, C. M. Bazán, M. Tie, A. Bencherif, and D. Bouilly, "Graphene field-effect transistors as bioanalytical sensors: Design, operation and performance," Jan. 21, 2021, *Royal Society of Chemistry*. doi: 10.1039/d0an01661f.

[63] C. N. R. Rao, A. K. Sood, K. S. Subrahmanyam, and A. Govindaraj, "Graphene: The new two-dimensional nanomaterial," Oct. 05, 2009. doi: 10.1002/anie.200901678.

[64] A. Ambrosi, C. K. Chua, A. Bonanni, and M. Pumera, "Electrochemistry of graphene and related materials," Jul. 23, 2014. doi: 10.1021/cr500023c.

[65] N. Kumar *et al.*, "Top-down synthesis of graphene: A comprehensive review," *FlatChem*, vol. 27, p. 100224, 2021, doi: https://doi.org/10.1016/j.flatc.2021.100224.

[66] X.-Y. Wang, A. Narita, and K. Müllen, "Precision synthesis versus bulk-scale fabrication of graphenes," *Nat Rev Chem*, vol. 2, no. 1, p. 0100, 2017, doi: 10.1038/s41570-017-0100.

[67] H. O. Pierson, *Handbook of chemical vapor deposition : principles, technology, and applications*. Noyes Publications, 1999.

[68] Y. Zhang, L. Zhang, and C. Zhou, "Review of chemical vapor deposition of graphene and related applications," *Acc Chem Res*, vol. 46, no. 10, pp. 2329–2339, Oct. 2013, doi: 10.1021/ar300203n.

[69] X. Li, L. Colombo, and R. S. Ruoff, "Synthesis of Graphene Films on Copper Foils by Chemical Vapor Deposition," *Advanced Materials*, vol. 28, no. 29, pp. 6247–6252, Aug. 2016, doi: 10.1002/adma.201504760.

[70] S. Bae *et al.*, "Roll-to-roll production of 30-inch graphene films for transparent electrodes," *Nat Nanotechnol*, vol. 5, no. 8, pp. 574–578, 2010, doi: 10.1038/nnano.2010.132.

[71] A. R. Ruiz Hernández, A. Gutierrez Cruz, and J. Campos-Delgado, "Chemical Vapor Deposition Synthesis of Graphene on Copper Foils." [Online]. Available: www.intechopen.com

[72] G. A. López and E. J. Mittemeijer, "The solubility of C in solid Cu," *Scr Mater*, vol. 51, no. 1, pp. 1–5, 2004, doi: https://doi.org/10.1016/j.scriptamat.2004.03.028.

[73] A. R. R. Hernández, A. G. Cruz, and J. Campos-Delgado, "Chemical Vapor Deposition Synthesis of Graphene on Copper Foils," in *Graphene*, M. Ikram, A. Maqsood, and A. Bashir, Eds., Rijeka: IntechOpen, 2022, p. Ch. 4. doi: 10.5772/intechopen.106058.

[74] X. Li *et al.*, "Large-area synthesis of high-quality and uniform graphene films on copper foils," *Science (1979)*, vol. 324, no. 5932, pp. 1312–1314, 2009, doi: 10.1126/science.1171245.

[75] M. Losurdo, M. M. Giangregorio, P. Capezzuto, and G. Bruno, "Graphene CVD growth on copper and nickel: Role of hydrogen in kinetics and structure," *Physical Chemistry Chemical Physics*, vol. 13, no. 46, pp. 20836–20843, Dec. 2011, doi: 10.1039/c1cp22347j.

[76] M. Saeed, Y. Alshammari, S. A. Majeed, and E. Al-Nasrallah, "Chemical Vapour Deposition of Graphene—Synthesis, Characterisation, and Applications: A Review," *Molecules*, vol. 25, no. 17, 2020, doi: 10.3390/molecules25173856.

[77] W. Liu, H. Li, C. Xu, Y. Khatami, and K. Banerjee, "Synthesis of high-quality monolayer and bilayer graphene on copper using chemical vapor deposition," *Carbon N Y*, vol. 49, no. 13, pp. 4122–4130, Nov. 2011, doi: 10.1016/j.carbon.2011.05.047.

[78] L. Sun *et al.*, "Chemical vapour deposition," Dec. 01, 2021, *Springer Nature*. doi: 10.1038/s43586-020-00005-y.

[79] L. Lin, B. Deng, J. Sun, H. Peng, and Z. Liu, "Bridging the Gap between Reality and Ideal in Chemical Vapor Deposition Growth of Graphene," Sep. 26, 2018, *American Chemical Society*. doi: 10.1021/acs.chemrev.8b00325.

[80] S. Bhaviripudi, X. Jia, M. S. Dresselhaus, and J. Kong, "Role of Kinetic Factors in Chemical Vapor Deposition Synthesis of Uniform Large Area Graphene Using Copper Catalyst," *Nano Lett*, vol. 10, no. 10, pp. 4128–4133, Oct. 2010, doi: 10.1021/nl102355e.

[81] Q. Yu *et al.*, "Control and characterization of individual grains and grain boundaries in graphene grown by chemical vapour deposition," *Nat Mater*, vol. 10, no. 6, pp. 443–449, 2011, doi: 10.1038/nmat3010.

[82] X. Liang *et al.*, "Toward clean and crackless transfer of graphene," *ACS Nano*, vol. 5, no. 11, pp. 9144–9153, Nov. 2011, doi: 10.1021/nn203377t.

[83] P. D. Cabral *et al.*, "Clean-room lithographical processes for the fabrication of graphene biosensors," *Materials*, vol. 13, no. 24, pp. 1–23, Dec. 2020, doi: 10.3390/ma13245728.

[84] M. A. Yoon, C. Kim, J. H. Kim, H. J. Lee, and K. S. Kim, "Surface Properties of CVD-Grown Graphene Transferred by Wet and Dry Transfer Processes," *Sensors*, vol. 22, no. 10, May 2022, doi: 10.3390/s22103944.

[85] H. Tan, "Advancements And Applications of Field-Effect Transistors in Modern Electronics," *Highlights in Science, Engineering and Technology*, vol. 81, pp. 318–322, Jan. 2024, doi: 10.54097/e52j3779.

[86] L. Hess, M. Seifert, and J. Garrido, "Graphene Transistors for Bioelectronics," *Proceedings of the IEEE*, vol. 101, pp. 1780–1792, Jul. 2013, doi: 10.1109/JPROC.2013.2261031.

[87] F. Torricelli *et al.*, "Electrolyte-gated transistors for enhanced performance bioelectronics," Dec. 01, 2021, *Springer Nature*. doi: 10.1038/s43586-021-00065-8.

[88] D. Wang, V. Noël, and B. Piro, "Electrolytic gated organic field-effect transistors for application in biosensors—A review," Feb. 25, 2016, *MDPI AG*. doi: 10.3390/electronics5010009.

[89] W. Zhou, X. Dai, and C. M. Lieber, "Advances in nanowire bioelectronics," *Reports on Progress in Physics*, vol. 80, no. 1, p. 16701, Nov. 2016, doi: 10.1088/0034-4885/80/1/016701.

[90] J. Rivnay, S. Inal, A. Salleo, R. M. Owens, M. Berggren, and G. G. Malliaras, "Organic electrochemical transistors," *Nat Rev Mater*, vol. 3, no. 2, p. 17086, 2018, doi: 10.1038/natrevmats.2017.86.

[91] A. Béraud, M. Sauvage, C. M. Bazán, M. Tie, A. Bencherif, and D. Bouilly, "Graphene field-effect transistors as bioanalytical sensors: Design, operation and performance," Jan. 21, 2021, *Royal Society of Chemistry*. doi: 10.1039/d0an01661f.

[92] P. K. Ang *et al.*, "A bioelectronic platform using a graphene-lipid bilayer interface," *ACS Nano*, vol. 4, no. 12, pp. 7387–7394, Dec. 2010, doi: 10.1021/nn1022582.

[93] "1923-debye-huckel-theory-1923-german-scan-1-high-exposure".

[94] W. Fu, L. Jiang, E. P. van Geest, L. M. C. Lima, and G. F. Schneider, "Sensing at the Surface of Graphene Field-Effect Transistors," Feb. 10, 2017, *Wiley-VCH Verlag*. doi: 10.1002/adma.201603610.

[95] R. Forsyth, A. Devadoss, and O. J. Guy, "Graphene field effect transistors for biomedical applications: Current status and future prospects," *Diagnostics*, vol. 7, no. 3, p. 45, 2017.

[96] F. Yan, M. Zhang, and J. Li, "Solution-gated graphene transistors for chemical and biological sensors," *Adv Healthc Mater*, vol. 3, no. 3, pp. 313–331, 2014.

[97] Y. Ohno, K. Maehashi, Y. Yamashiro, and K. Matsumoto, "Electrolyte-Gated Graphene Field-Effect Transistors for Detecting pH and Protein Adsorption," *Nano Lett*, vol. 9, no. 9, pp. 3318–3322, Sep. 2009, doi: 10.1021/nl901596m.

[98] Y. Ohno, K. Maehashi, Y. Yamashiro, and K. Matsumoto, "Electrolyte-gated graphene field-effect transistors for detecting ph and protein adsorption," *Nano Lett*, vol. 9, no. 9, pp. 3318–3322, Sep. 2009, doi: 10.1021/nl901596m.

[99] S. Szunerits, T. Rodrigues, R. Bagale, H. Happy, R. Boukherroub, and W. Knoll, "Graphene-based field-effect transistors for biosensing: where is the field heading to?," *Anal Bioanal Chem*, vol. 416, no. 9, pp. 2137–2150, 2024, doi: 10.1007/s00216-023-04760-1.

[100] E. Fernandes *et al.*, "Functionalization of single-layer graphene for immunoassays," *Appl Surf Sci*, vol. 480, pp. 709–716, Jun. 2019, doi: 10.1016/j.apsusc.2019.03.004.

[101] D. Kwong Hong Tsang *et al.*, "Chemically Functionalised Graphene FET Biosensor for the Label-free Sensing of Exosomes," *Sci Rep*, vol. 9, no. 1, Dec. 2019, doi: 10.1038/s41598-019-50412-9.

[102] Y. Ohno, S. Okamoto, K. Maehashi, and K. Matsumoto, "Direct electrical detection of DNA hybridization based on electrolyte-gated graphene field-effect transistor," *Jpn J Appl Phys*, vol. 52, no. 11 PART 1, Nov. 2013, doi: 10.7567/JJAP.52.110107.

[103] R. Campos *et al.*, "Attomolar label-free detection of dna hybridization with electrolyte-gated graphene field-effect transistors," *ACS Sens*, vol. 4, no. 2, pp. 286–293, Feb. 2019, doi: 10.1021/acssensors.8b00344.

[104] P. Laaksonen *et al.*, "Interfacial Engineering by Proteins: Exfoliation and Functionalization of Graphene by Hydrophobins," *Angewandte Chemie International Edition*, vol. 49, no. 29, pp. 4946–4949, 2010, doi: https://doi.org/10.1002/anie.201001806.

[105] X. You and J. J. Pak, "Graphene-based field effect transistor enzymatic glucose biosensor using silk protein for enzyme immobilization and device substrate," *Sens Actuators B Chem*, vol. 202, pp. 1357–1365, 2014, doi: https://doi.org/10.1016/j.snb.2014.04.079.

[106] G. E. Fenoy, W. A. Marmisollé, W. Knoll, and O. Azzaroni, "Highly sensitive urine glucose detection with graphene field-effect transistors functionalized with electropolymerized nanofilms," *Sensors & Diagnostics*, vol. 1, no. 1, pp. 139–148, 2022, doi: 10.1039/D1SD00007A.

[107] M. Zhang, C. Liao, C. H. Mak, P. You, C. L. Mak, and F. Yan, "Highly sensitive glucose sensors based on enzyme-modified whole-graphene solution-gated transistors," *Sci Rep*, vol. 5, no. 1, p. 8311, 2015, doi: 10.1038/srep08311.

[108] H. Yao, A. J. Shum, M. Cowan, I. Lähdesmäki, and B. A. Parviz, "A contact lens with embedded sensor for monitoring tear glucose level," *Biosens Bioelectron*, vol. 26, no. 7, pp. 3290–3296, Mar. 2011, doi: 10.1016/j.bios.2010.12.042.

[109] S. Kaur *et al.*, "Graphene electrodes for adaptive liquid crystal contact lenses," *Opt Express*, vol. 24, no. 8, p. 8782, Apr. 2016, doi: 10.1364/oe.24.008782.

[110] S. M. Shin, H. I. Park, and A. Y. Sung, "Analysis of Physical and Antibacterial Properties of Functional Silicone Hydrogel Ophthalmic Lenses Containing Graphene Groups," *Korean Journal of Materials Research*, vol. 33, no. 1, pp. 1–7, 2023, doi: 10.3740/MRSK.2023.33.1.1.

[111] R. Yin *et al.*, "Soft transparent graphene contact lens electrodes for conformal full-cornea recording of electroretinogram," *Nat Commun*, vol. 9, no. 1, Dec. 2018, doi: 10.1038/s41467-018-04781-w.

[112] J. F. Huang *et al.*, "A Hydrogel-Based Hybrid Theranostic Contact Lens for Fungal Keratitis," *ACS Nano*, vol. 10, no. 7, pp. 6464–6473, Jul. 2016, doi: 10.1021/acsnano.6b00601.

[113] D. T. Desai *et al.*, "In vitro and in vivo evaluation of cyclosporine-graphene oxide laden hydrogel contact lenses," *Int J Pharm*, vol. 613, Feb. 2022, doi: 10.1016/j.ijpharm.2021.121414.

[114] A. K. Schuster, C. Erb, E. M. Hoffmann, T. Dietlein, and N. Pfeiffer, "The diagnosis and treatment of glaucoma," *Dtsch Arztebl Int*, vol. 117, no. 13, pp. 225–234, Mar. 2020, doi: 10.3238/arztebl.2020.0225.

[115] S. Y. W. Liang, G. A. Lee, and D. Shields, "Self-tonometry in Glaucoma Management-Past, Present and Future," 2009, *Elsevier USA*. doi: 10.1016/j.survophthal.2009.04.006.

[116] Z. Liu *et al.*, "An Ultrasensitive Contact Lens Sensor Based On Self-Assembly Graphene For Continuous Intraocular Pressure Monitoring," *Adv Funct Mater*, vol. 31, no. 29, Jul. 2021, doi: 10.1002/adfm.202010991.

[117] J. Xu *et al.*, "Highly Transparent and Sensitive Graphene Sensors for Continuous and Non-invasive Intraocular Pressure Monitoring," *ACS Appl Mater Interfaces*, vol. 12, no. 16, pp. 18375–18384, Apr. 2020, doi: 10.1021/acsami.0c02991.

[118] Y. Zhang *et al.*, "High resolution non-invasive intraocular pressure monitoring by use of graphene woven fabrics on contact lens," *Microsyst Nanoeng*, vol. 5, no. 1, Dec. 2019, doi: 10.1038/s41378-019-0078-x.

[119] B. M. Harkness *et al.*, “Tear Proteins Altered in Patients with Persistent Eye Pain after Refractive Surgery: Biomarker Candidate Discovery,” *J Proteome Res*, vol. 23, no. 7, pp. 2629–2640, Jul. 2024, doi: 10.1021/acs.jproteome.4c00339.

[120] A. Hussain, Z. Sheikh, and M. Subramanian, “The Eye as a Diagnostic Tool for Alzheimer’s Disease,” Mar. 01, 2023, *MDPI*. doi: 10.3390/life13030726.

[121] M. Yazdani, K. B. P. Elgstøen, H. Rootwelt, A. Shahdadfar, Ø. A. Utheim, and T. P. Utheim, “Tear metabolomics in dry eye disease: A review,” Aug. 01, 2019, *MDPI AG*. doi: 10.3390/ijms20153755.

[122] S. Kaštelan *et al.*, “Tear Biomarkers and Alzheimer’s Disease,” Sep. 01, 2023, *Multidisciplinary Digital Publishing Institute (MDPI)*. doi: 10.3390/ijms241713429.

[123] S. Hagan, E. Martin, and A. Enríquez-de-Salamanca, “Tear fluid biomarkers in ocular and systemic disease: Potential use for predictive, preventive and personalised medicine,” Jul. 13, 2016, *BioMed Central Ltd.* doi: 10.1186/s13167-016-0065-3.

[124] A. Daily, P. Ravishankar, S. Harms, and V. S. Klimberg, “Using tears as a non-invasive source for early detection of breast cancer,” *PLoS One*, vol. 17, no. 4 April, Apr. 2022, doi: 10.1371/journal.pone.0267676.

[125] M. Ku *et al.*, “E N G I N E E R I N G Smart, soft contact lens for wireless immunosensing of cortisol,” 2020. [Online]. Available: https://www.science.org

[126] W. Zhang *et al.*, “Wearable Corneal Biosensors Fabricated from PEDOT Functionalized Sulfur-Doped Graphene for Use in the Early Detection of Myopia,” *Adv Mater Technol*, vol. 5, no. 12, Dec. 2020, doi: 10.1002/admt.202000682.

[127] M. X. Chu *et al.*, “Soft contact lens biosensor for in situ monitoring of tear glucose as non-invasive blood sugar assessment,” *Talanta*, vol. 83, no. 3, pp. 960–965, Jan. 2011, doi: 10.1016/j.talanta.2010.10.055.

[128] C. Chung, Y.-K. Kim, D. Shin, S.-R. Ryoo, B. H. Hong, and D.-H. Min, “Biomedical Applications of Graphene and Graphene Oxide,” *Acc Chem Res*, vol. 46, no. 10, pp. 2211–2224, Oct. 2013, doi: 10.1021/ar300159f.

[129] A. Gulzar *et al.*, “Bioapplications of graphene constructed functional nanomaterials,” Jan. 25, 2017, *Elsevier Ireland Ltd*. doi: 10.1016/j.cbi.2016.11.019.

[130] J. Park *et al.*, “A P P L I E D S C I E N C E S A N D E N G I N E E R I N G Soft, smart contact lenses with integrations of wireless circuits, glucose sensors, and displays,” 2018.

[131] J. Kim *et al.*, "Wearable smart sensor systems integrated on soft contact lenses for wireless ocular diagnostics," *Nat Commun*, vol. 8, 2017, doi: 10.1038/ncomms14997.

[132] S. Lee *et al.*, "Smart Contact Lenses with Graphene Coating for Electromagnetic Interference Shielding and Dehydration Protection," *ACS Nano*, vol. 11, no. 6, pp. 5318–5324, Jun. 2017, doi: 10.1021/acsnano.7b00370.

[133] M. Leonardi, E. M. Pitchon, A. Bertsch, P. Renaud, and A. Mermoud, "Wireless contact lens sensor for intraocular pressure monitoring: Assessment on enucleated pig eyes," *Acta Ophthalmol*, vol. 87, no. 4, pp. 433–437, Jun. 2009, doi: 10.1111/j.1755-3768.2008.01404.x.

[134] K. Choi and H. G. Park, "Smart Reinvention of the Contact Lens with Graphene," Jun. 27, 2017, *American Chemical Society*. doi: 10.1021/acsnano.7b03180.

[135] C.-D. Liao *et al.*, "Optimizing PMMA solutions to suppress contamination in the transfer of CVD graphene for batch production," *Beilstein Journal of Nanotechnology*, vol. 13, pp. 796–806, 2022, doi: 10.3762/bjnano.13.70.

[136] E. Fernandes *et al.*, "Functionalization of single-layer graphene for immunoassays," *Appl Surf Sci*, vol. 480, pp. 709–716, Jun. 2019, doi: 10.1016/j.apsusc.2019.03.004.

[137] "Under_the_Microscope".

[138] "Introduction, Basic Theory and Principles," in *Modern Raman Spectroscopy – A Practical Approach*, John Wiley & Sons, Ltd, 2004, ch. 1, pp. 1–21. doi: https://doi.org/10.1002/0470011831.ch1.

[139] C. N. R. Rao, A. K. Sood, K. S. Subrahmanyam, and A. Govindaraj, "Graphene: The new two-dimensional nanomaterial," Oct. 05, 2009. doi: 10.1002/anie.200901678.

[140] A. C. Ferrari and D. M. Basko, "Raman spectroscopy as a versatile tool for studying the properties of graphene," 2013, *Nature Publishing Group*. doi: 10.1038/nnano.2013.46.

[141] L. M. Malard, M. A. Pimenta, G. Dresselhaus, and M. S. Dresselhaus, "Raman spectroscopy in graphene," Apr. 2009. doi: 10.1016/j.physrep.2009.02.003.

[142] J. Hodkiewicz, "Characterizing Graphene with Raman Spectroscopy."

[143] Y. Hao *et al.*, "Probing layer number and stacking order of few-layer graphene by Raman Spectroscopy," *Small*, vol. 6, no. 2, pp. 195–200, Jan. 2010, doi: 10.1002/smll.200901173.

[144] J. F. Moulder, W. F. Stickle, P. E. ' Sobol, K. D. Bomben, and J. Chastain, "Handbook of X-ray Photoelectron Spectroscopy AReference Book of Standard Spectra for Identification and Interpretation of XPS Data."

[145] N. Fairley *et al.*, "Systematic and collaborative approach to problem solving using X-ray photoelectron spectroscopy," *Applied Surface Science Advances*, vol. 5, p. 100112, 2021.

[146] J. T. Korhonen, T. Huhtamäki, O. Ikkala, and R. H. A. Ras, "Reliable Measurement of the Receding Contact Angle," *Langmuir*, vol. 29, no. 12, pp. 3858–3863, Mar. 2013, doi: 10.1021/la400009m.

[147] M. Abe, "Contact Angle Measurement for Solid Surface," in *Measurement Techniques and Practices of Colloid and Interface Phenomena*, M. Abe, Ed., Singapore: Springer Singapore, 2019, pp. 129–135. doi: 10.1007/978-981-13-5931-6_18.

[148] L. A. Belyaeva and G. F. Schneider, "Wettability of graphene," May 01, 2020, *Elsevier B.V.* doi: 10.1016/j.surfrep.2020.100482.

[149] A. V Prydatko, L. A. Belyaeva, L. Jiang, L. M. C. Lima, and G. F. Schneider, "Contact angle measurement of free-standing square-millimeter single-layer graphene," *Nat Commun*, vol. 9, no. 1, p. 4185, 2018, doi: 10.1038/s41467-018-06608-0.

[150] L. A. Belyaeva, P. M. G. van Deursen, K. I. Barbetsea, and G. F. Schneider, "Hydrophilicity of Graphene in Water through Transparency to Polar and Dispersive Interactions," *Advanced Materials*, vol. 30, no. 6, p. 1703274, 2018, doi: https://doi.org/10.1002/adma.201703274.

[151] O. Leenaerts, B. Partoens, and F. M. Peeters, "Water on graphene: Hydrophobicity and dipole moment using density functional theory," *Phys Rev B Condens Matter Mater Phys*, vol. 79, no. 23, Jun. 2009, doi: 10.1103/PhysRevB.79.235440.

[152] F. Taherian, V. Marcon, N. F. A. van der Vegt, and F. Leroy, "What Is the Contact Angle of Water on Graphene?," *Langmuir*, vol. 29, no. 5, pp. 1457–1465, 2013, doi: 10.1021/la304645w.

[153] J. Rafiee *et al.*, "Wetting transparency of graphene," *Nat Mater*, vol. 11, no. 3, pp. 217–222, 2012, doi: 10.1038/nmat3228.

[154] C. J. Shih, M. S. Strano, and D. Blankschtein, "Wetting translucency of graphene," 2013, *Nature Publishing Group*. doi: 10.1038/nmat3760.

[155] L. A. Belyaeva, C. Tang, L. Juurlink, and G. F. Schneider, "Macroscopic and Microscopic Wettability of Graphene," *Langmuir*, vol. 37, no. 14, pp. 4049–4055, Apr. 2021, doi: 10.1021/acs.langmuir.0c02817.

[156] Z. Li *et al.*, "Effect of airborne contaminants on the wettability of supported graphene and graphite," *Nat Mater*, vol. 12, no. 10, pp. 925–931, Oct. 2013, doi: 10.1038/nmat3709.

[157] G. Hong *et al.*, "On the mechanism of hydrophilicity of graphene."

[158] A. Ashraf *et al.*, "Doping-Induced Tunable Wettability and Adhesion of Graphene," *Nano Lett*, vol. 16, no. 7, pp. 4708–4712, 2016, doi: 10.1021/acs.nanolett.6b02228.

[159] J. A. Bauer, M. Zámocká, J. Majtán, and V. Bauerová-Hlinková, "Glucose oxidase, an enzyme 'Ferrari': Its structure, function, production and properties in the light of various industrial and biotechnological applications," *Biomolecules*, vol. 12, no. 3, p. 472, 2022.

[160] G. B. Smejkal and S. Kakumanu, "Enzymes and their turnover numbers," *Expert Rev Proteomics*, vol. 16, no. 7, pp. 543–544, 2019.

[161] R. Roskoski, "Michaelis-Menten Kinetics," *xPharm: The Comprehensive Pharmacology Reference*, pp. 1–10, Jan. 2007, doi: 10.1016/B978-008055232-3.60041-8.

[162] J. Park *et al.*, "Soft, smart contact lenses with integrations of wireless circuits, glucose sensors, and displays," *Sci Adv*, vol. 4, no. 1, p. eaap9841, 2018.

[163] P. Leyton, J. S. Gómez-Jeria, S. Sanchez-Cortes, C. Domingo, and M. Campos-Vallette, "Carbon nanotube bundles as molecular assemblies for the detection of polycyclic aromatic hydrocarbons: surface-enhanced resonance Raman spectroscopy and theoretical studies," *J Phys Chem B*, vol. 110, no. 13, pp. 6470–6474, 2006.

[164] Y. Liu *et al.*, "Giant enhancement in vertical conductivity of stacked CVD graphene sheets by self-assembled molecular layers," *Nat Commun*, vol. 5, no. 1, p. 5461, 2014.

[165] G. Wu, X. Tang, M. Meyyappan, and K. W. C. Lai, "Doping effects of surface functionalization on graphene with aromatic molecule and organic solvents," *Appl Surf Sci*, vol. 425, pp. 713–721, 2017.

[166] K. L. Yang, J. O. Lee, H. Choo, and F. Yang, "Can Raman Shift Be Used To Characterize the Mechanical Property of Graphene?," *The Journal of Physical Chemistry C*, vol. 122, no. 42, pp. 24467–24474, 2018.

[167] Z. H. Ni, T. Yu, Y. H. Lu, Y. Y. Wang, Y. P. Feng, and Z. X. Shen, "Uniaxial strain on graphene: Raman spectroscopy study and band-gap opening," *ACS Nano*, vol. 2, no. 11, pp. 2301–2305, 2008.

[168] J. E. Lee, G. Ahn, J. Shim, Y. S. Lee, and S. Ryu, "Optical separation of mechanical strain from charge doping in graphene," *Nat Commun*, vol. 3, no. 1, p. 1024, 2012.

[169] G. B. Barin, Y. Song, I. de Fátima Gimenez, A. G. Souza Filho, L. S. Barreto, and J. Kong, "Optimized graphene transfer: Influence of polymethylmethacrylate (PMMA) layer concentration and baking time on graphene final performance," *Carbon N Y*, vol. 84, pp. 82–90, 2015.

[170] X. Dong, D. Fu, W. Fang, Y. Shi, P. Chen, and L. J. Li, "Doping single-layer graphene with aromatic molecules," *Small*, 2009.

[171] A. Das *et al.*, "Monitoring dopants by Raman scattering in an electrochemically top-gated graphene transistor," *Nat Nanotechnol*, vol. 3, no. 4, pp. 210–215, 2008.

[172] D. Kwong Hong Tsang *et al.*, "Chemically functionalised graphene FET biosensor for the label-free sensing of exosomes," *Sci Rep*, vol. 9, no. 1, pp. 1–10, 2019.

[173] S. N. Faisal *et al.*, "Pyridinic and graphitic nitrogen-rich graphene for high-performance supercapacitors and metal-free bifunctional electrocatalysts for ORR and OER," *RSC Adv*, vol. 7, no. 29, pp. 17950–17958, 2017.

[174] A. Silvestri *et al.*, "Ultrasensitive detection of SARS-CoV-2 spike protein by graphene field-effect transistors," *Nanoscale*, vol. 15, no. 3, pp. 1076–1085, 2023.

[175] G. Wu, X. Tang, M. Meyyappan, and K. W. C. Lai, "Chemical functionalization of graphene with aromatic molecule," in *2015 IEEE 15th International Conference on Nanotechnology (IEEE-NANO)*, IEEE, 2015, pp. 1324–1327.

[176] Y. Xia *et al.*, "Grafting Ink for Direct Writing: Solvation Activated Covalent Functionalization of Graphene," *Advanced Science*, vol. 9, no. 19, Jul. 2022, doi: 10.1002/advs.202105017.

[177] K. K. Singh, "A DFT studies on absorbing and sensing possibilities of glucose on graphene surface doped with Ag, Au, Cu, Ni & Pt atoms," *Biosens Bioelectron X*, vol. 13, p. 100287, 2023.

[178] A. Ahmadianyazdi, N. H. L. Nguyen, J. Xu, and V. Berry, "Glucose measurement via Raman spectroscopy of graphene: Principles and operation," *Nano Res*, vol. 15, no. 10, pp. 8697–8704, 2022.

[179] Y. H. Kwak *et al.*, "Flexible glucose sensor using CVD-grown graphene-based field effect transistor," *Biosens Bioelectron*, vol. 37, no. 1, pp. 82–87, 2012.

[180] V. A. Kislenko, S. V Pavlov, and S. A. Kislenko, "Influence of defects in graphene on electron transfer kinetics: The role of the surface electronic structure," *Electrochim Acta*, vol. 341, p. 136011, 2020.

[181] X. You and J. J. Pak, "Graphene-based field effect transistor enzymatic glucose biosensor using silk protein for enzyme immobilization and device substrate," *Sens Actuators B Chem*, vol. 202, pp. 1357–1365, 2014.

[182] P. Salvo *et al.*, "Graphene-based devices for measuring pH," *Sens Actuators B Chem*, vol. 256, pp. 976–991, 2018, doi: https://doi.org/10.1016/j.snb.2017.10.037.

[183] G. E. Fenoy, W. A. Marmisollé, O. Azzaroni, and W. Knoll, "Acetylcholine biosensor based on the electrochemical functionalization of graphene field-effect transistors," *Biosens Bioelectron*, vol. 148, p. 111796, 2020.

[184] P. F. Greenfield, J. R. Kittrell, and R. L. Laurence, "Inactivation of immobilized glucose oxidase by hydrogen peroxide," *Anal Biochem*, vol. 65, no. 1–2, pp. 109–124, 1975.

[185] J. E. Richards, M. A. Mazzeffi, M. S. Massey, P. Rock, S. M. Galvagno, and T. M. Scalea, "The bitter and the sweet: relationship of lactate, glucose, and mortality after severe blunt trauma," *Anesth Analg*, vol. 133, no. 2, pp. 455–461, 2021.

[186] Y. H. Kwak *et al.*, "Flexible glucose sensor using CVD-grown graphene-based field effect transistor," *Biosens Bioelectron*, vol. 37, no. 1, pp. 82–87, 2012, doi: https://doi.org/10.1016/j.bios.2012.04.042.

[187] Y. Huang, X. Dong, Y. Shi, C. M. Li, L.-J. Li, and P. Chen, "Nanoelectronic biosensors based on CVD grown graphene," *Nanoscale*, vol. 2, no. 8, pp. 1485–1488, 2010, doi: 10.1039/C0NR00142B.

[188] X. Chen *et al.*, "FM-Level Detection of Glucose Using a Grating Based Sensor Enhanced With Graphene Oxide," *Journal of Lightwave Technology*, vol. PP, p. 1, Jan. 2022, doi: 10.1109/JLT.2022.3174039.

[189] S. Wu, Y. Zhang, L. Liu, and W. Fan, "Conifer-like copper-carboxylated graphene nanocomposites modified electrode for sensitive nonenzymatic glucose biosensing with very low limit of detection," *Mater Lett*, vol. 276, p. 128253, 2020, doi: https://doi.org/10.1016/j.matlet.2020.128253.

[190] F. Cao, S. Guo, H. Ma, G. Yang, S. Yang, and J. Gong, "Highly sensitive nonenzymatic glucose sensor based on electrospun copper oxide-doped nickel oxide composite microfibers," *Talanta*, vol. 86, no. 1, pp. 214–220, Oct. 2011, doi: 10.1016/j.talanta.2011.09.003.

[191] J. Luo, S. Jiang, H. Zhang, J. Jiang, and X. Liu, "A novel non-enzymatic glucose sensor based on Cu nanoparticle modified graphene sheets electrode," *Anal Chim Acta*, vol. 709, pp. 47–53, 2012, doi: https://doi.org/10.1016/j.aca.2011.10.025.

[192] F. Wang *et al.*, "pM Level and Large Dynamic Range Glucose Detection Based on a Sandwich Type Plasmonic Fiber Sensor," *Journal of Lightwave Technology*, vol. 39, no. 12, pp. 3882–3889, 2021, doi: 10.1109/JLT.2020.3039776.

[193] M. Hernaez, B. Acevedo, A. G. Mayes, and S. Melendi-Espina, "High-performance optical fiber humidity sensor based on lossy mode resonance using a nanostructured polyethylenimine and graphene oxide coating," *Sens Actuators B Chem*, vol. 286, pp. 408–414, 2019.

[194] S. M. Oja, B. Feldman, and M. W. Eshoo, "Method for Low Nanomolar Concentration Analyte Sensing Using Electrochemical Enzymatic Biosensors," *Anal Chem*, vol. 90, no. 3, pp. 1536–1541, Feb. 2018, doi: 10.1021/acs.analchem.7b04075.

[195] B. Jiang *et al.*, "Label-free glucose biosensor based on enzymatic graphene oxide-functionalized tilted fiber grating," *Sens Actuators B Chem*, vol. 254, pp. 1033–1039, 2018, doi: https://doi.org/10.1016/j.snb.2017.07.109.

[196] Y. Lin, F. Lu, Y. Tu, and Z. Ren, "Glucose Biosensors Based on Carbon Nanotube Nanoelectrode Ensembles," *Nano Lett*, vol. 4, no. 2, pp. 191–195, Feb. 2004, doi: 10.1021/nl0347233.

[197] B. Unnikrishnan, S. Palanisamy, and S.-M. Chen, "A simple electrochemical approach to fabricate a glucose biosensor based on graphene–glucose oxidase biocomposite," *Biosens Bioelectron*, vol. 39, no. 1, pp. 70–75, 2013, doi: https://doi.org/10.1016/j.bios.2012.06.045.

[198] K.-Y. Hwa and B. Subramani, "Synthesis of zinc oxide nanoparticles on graphene–carbon nanotube hybrid for glucose biosensor applications," *Biosens Bioelectron*, vol. 62, pp. 127–133, 2014, doi: https://doi.org/10.1016/j.bios.2014.06.023.

[199] K. Dawson, M. Baudequin, and A. O'Riordan, "Single on-chip gold nanowires for electrochemical biosensing of glucose," *Analyst*, vol. 136, no. 21, pp. 4507–4513, 2011, doi: 10.1039/C1AN15279C.

[200] H. Liu, X. Qian, S. Wang, Y. Li, Y. Song, and D. Zhu, "Ultra-Sensitivity Glucose Sensor Based on Field Emitters," *Nanoscale Res Lett*, vol. 4, no. 10, p. 1141, 2009, doi: 10.1007/s11671-009-9372-0.

[201] A. A. Karyakin, O. V Gitelmacher, and E. E. Karyakina, "Prussian Blue-Based First-Generation Biosensor. A Sensitive Amperometric Electrode for Glucose," *Anal Chem*, vol. 67, no. 14, pp. 2419–2423, Jul. 1995, doi: 10.1021/ac00110a016.

[202] J. Lu, I. Do, L. T. Drzal, R. M. Worden, and I. Lee, "Nanometal-Decorated Exfoliated Graphite Nanoplatelet Based Glucose Biosensors with High Sensitivity and Fast Response," *ACS Nano*, vol. 2, no. 9, pp. 1825–1832, Sep. 2008, doi: 10.1021/nn800244k.

[203] S. Zhong and C.-H. Jang, "Highly sensitive and selective glucose sensor based on ultraviolet-treated nematic liquid crystals," *Biosens Bioelectron*, vol. 59, pp. 293–299, 2014, doi: https://doi.org/10.1016/j.bios.2014.03.070.

[204] S. Goniszewski, M. Adabi, O. Shaforost, S. M. Hanham, L. Hao, and N. Klein, "Correlation of p-doping in CVD Graphene with Substrate Surface Charges," *Sci Rep*, vol. 6, no. 1, p. 22858, 2016.

[205] A. Ashraf *et al.*, "Doping-induced tunable wettability and adhesion of graphene," *Nano Lett*, vol. 16, no. 7, pp. 4708–4712, 2016.

APPENDIX I

For the GOx peaks assessment, GOx in its powder form and dissolved in water was analysed in Raman Spectroscopy, as shown in Figure 43a. The main most intense peaks seen are around 2930 cm^{-1}, 1660 cm^{-1} and 1450 cm^{-1}. Figure 43b shows the fitting of the GOx peak. In Figure 43c is possible to see a slight bump in the 2900-3000 range when comparing the before and after the functionalization of PBASE/Gr with GOx.

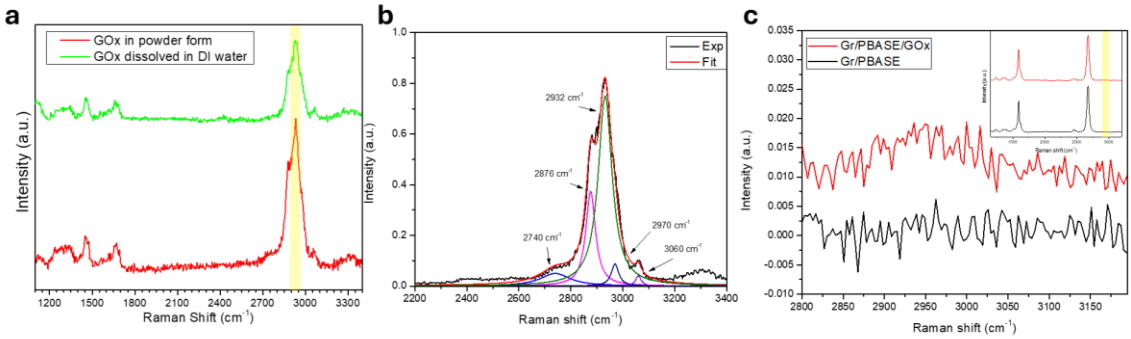


Figure 43: (a) Raman spectra of GOx: powder form and dissolved in DI water. (b) The 2800-3100 cm^{-1} range (highlighted by a yellow stripe in (a)) fitted with Lorentzian functions. (c) Gr/PBASE and Gr/PBASE/GOx spectra zoomed-in in the 2800-3100 cm^{-1} range, showing a small contribution at 2947 cm^{-1} in the Gr/PBASE/GOx spectrum, not visible in Gr/PBASE.

APPENDIX II

Figure 44 shows the change in FWHM of the graphene peaks in each step of the functionalization process on a Si/SiO_2 substrate. The FWHM of the 2D peak slightly decreases from 39.82 cm^{-1} in pristine graphene to 39.77 cm^{-1} in /PBASE/Gr and increases when adding GOx to 42.04 cm^{-1}. Regarding the G peak, an increase is noticeable, going from 21.65 cm^{-1} for pristine graphene to 26.04 cm^{-1}.

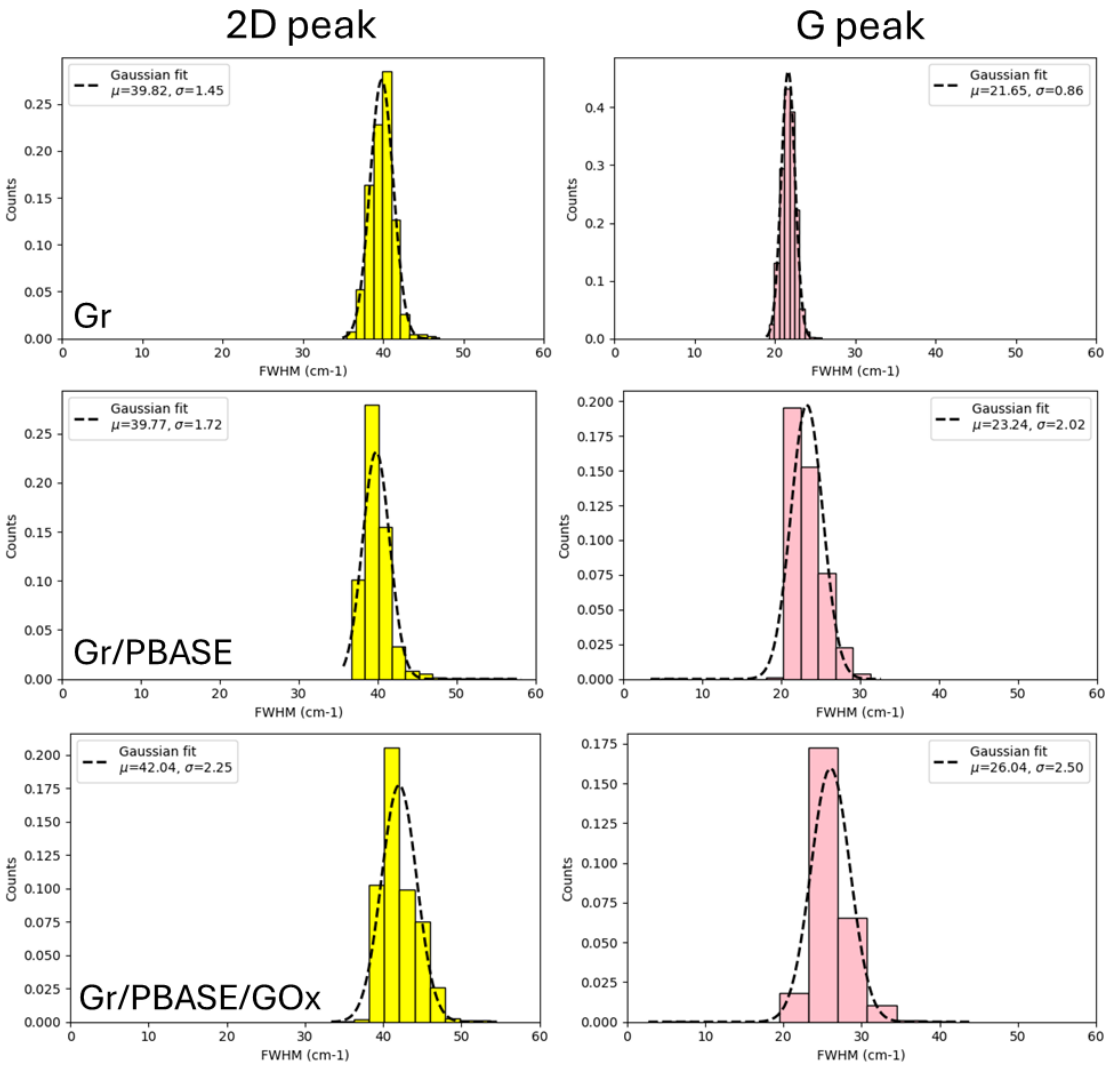


Figure 44: FWHM distribution of the 2D and G peaks of graphene for Gr, Gr/PBASE and Gr/PBASE/GOx on Si/SiO_2.

APPENDIX III

Figure 45 shows the XPS survey for each step of the functionalization process.

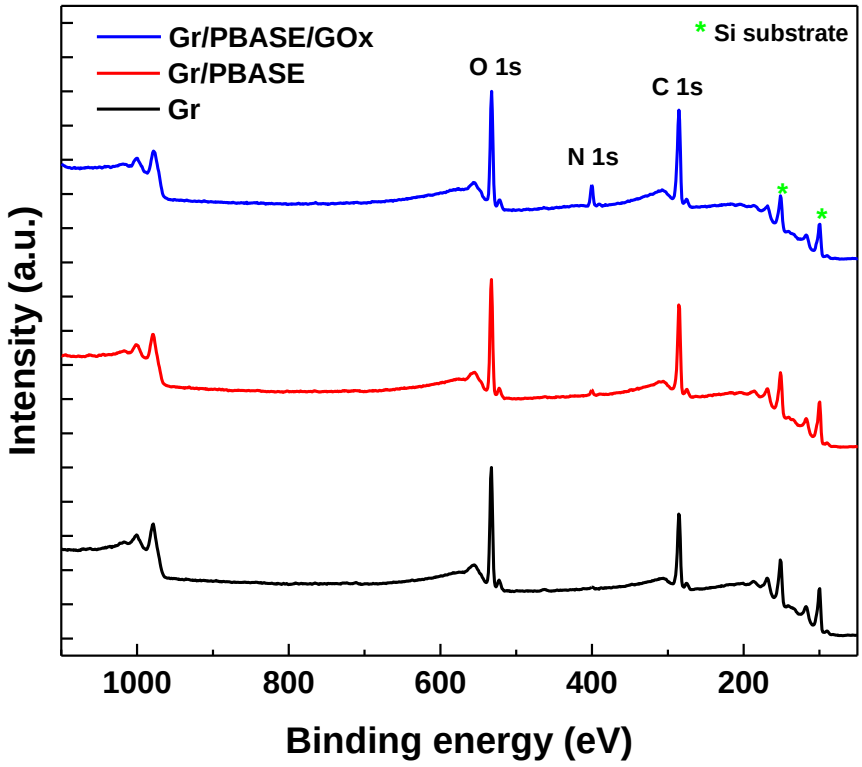


Figure 45: XPS survey spectra for Gr, Gr/PBASE and Gr/PBASE/GOx.

APPENDIX IV

Our electrolyte-gated graphene field-effect transistor chip microfabrication is described elsewhere [32]. Briefly, a 200 mm silicon (Si) wafer (p-type doped with boron, B) with 100 nm of thermal oxide sputter-coated with chromium (Cr, 3 nm) as the adhesion layer, gold (Au, 35 nm) as the conductive layer, and alumina (Al_2O_3, 100 nm) capping. The source, drain and gate Au electrodes were patterned through optical lithography and ion milling. A sacrificial layer (TiWN, 5 nm; AlSiCu, 100 nm; TiWN, 15 nm) was sputtered and patterned by lift-off, leaving only open the GFET channel areas to transfer the graphene. This sacrificial layer protected the wafer from potential contamination from graphene transfer processes. After transfer, the graphene was patterned by optical lithography and oxygen plasma etching, followed by wet etching of the sacrificial layer. A protective layer of Nickel (Ni, 100 nm) was sputtered and patterned by lift-off to work as a stopping layer for ion milling. The multistack passivation layers of SiO_2 (50 nm) and Si_3N_4 (50 nm) (total thickness of 300 nm) were then grown by plasma-enhanced CVD, patterned via optical lithography and etched to cover the entire sensor area except the graphene channel, the gold gate, and the contact pads. Finally, wet etching of Ni and Al_2O_3 was performed. The wafer was diced into 729 equal-sized 5 × 5 mm^2 chips (Figure 46a). Each chip consists of two gate electrodes and 32 graphene channels (EG-GFETs), each group of 16 with their drains connected to a common source (Figure 46b). The chip photoresist was dissolved in acetone and then cleaned with IPA and DI water. The chips were then glued onto a printed circuit board, wire bonded with gold wires and protected with a silicon elastomer.

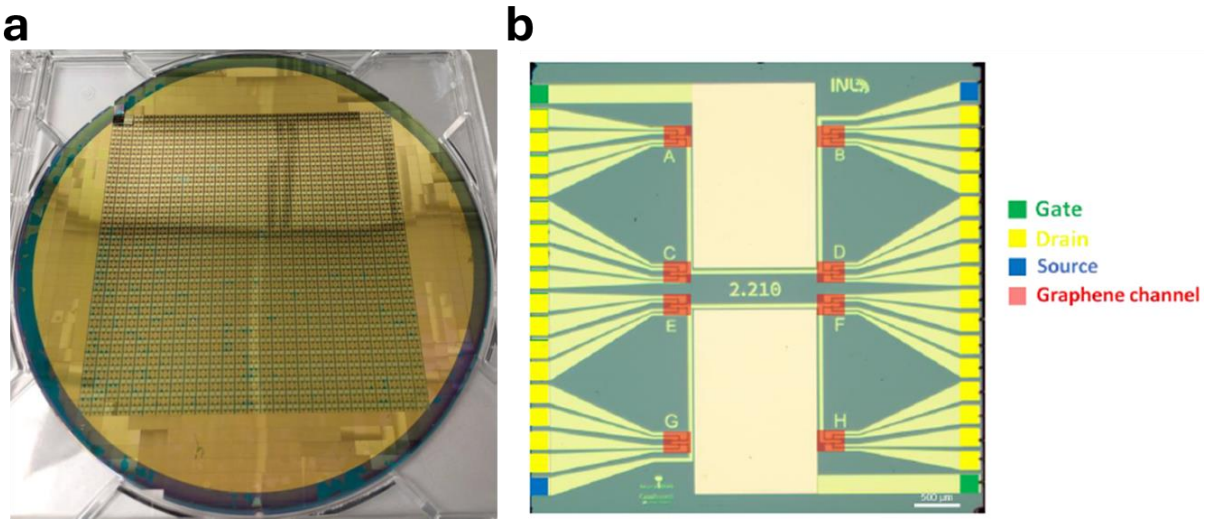


Figure 46: (a) EG-GFETs' finished wafer. (b) Layout of EG-GFETs' chip. Drains (yellow pads), sources (blue pads), gates (green pads) and graphene channels (red rectangles).

APPENDIX V

Figure 47a shows the variation of the graphene peaks after incubation with DDT and DMSO. The graphene used in both cases has 2D peak positioned at 2671.98 cm^{-1} and G peak at 1584.14 cm^{-1}. In the case of DDT incubation, both peaks are red shifted. The 2D peak shifted to 2665.36 cm^{-1} and the G peak to 1581.4 cm^{-1}. After the linear transformation, it's possible to conclude that this shift is not caused by the doping of graphene but due to the changes in the mechanical strain. Figure 47b shows that the compressive strain increases from -0.21% to -0.32%. When incubating with DMSO, both 2D and G peaks also redshifted to 2662.89 cm^{-1} and 1579.65 cm^{-1}, respectively. Similarly to DDT, an increase in tensile strain was observed but with a decrease in charge density from 15.23 (10^{12} cm^{-2}) to 13.47 (10^{12} cm^{-2}).

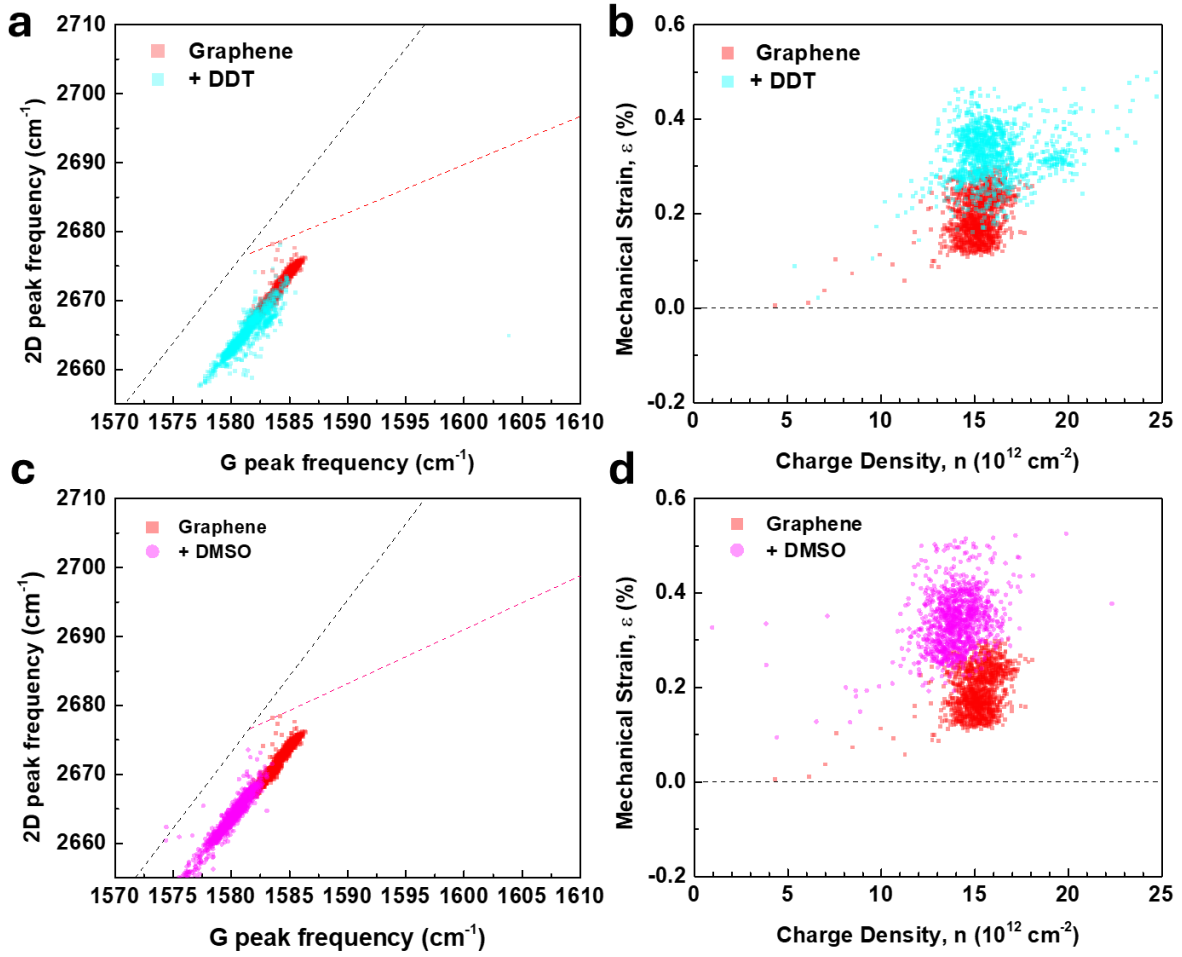


Figure 47: Variation of 2D and G modes frequency after Au passivation with DDT molecules. Visualization on (a) 2D vs G frequency plot and on (b) mechanical strain vs charge density plot. Variation of 2D and G modes frequency after Gr incubation with DMSO. Visualization on (a) 2D vs G frequency plot and on (b) mechanical strain vs charge density plot. All data shown are a combination of 1500 measurements for each step.

APPENDIX VI

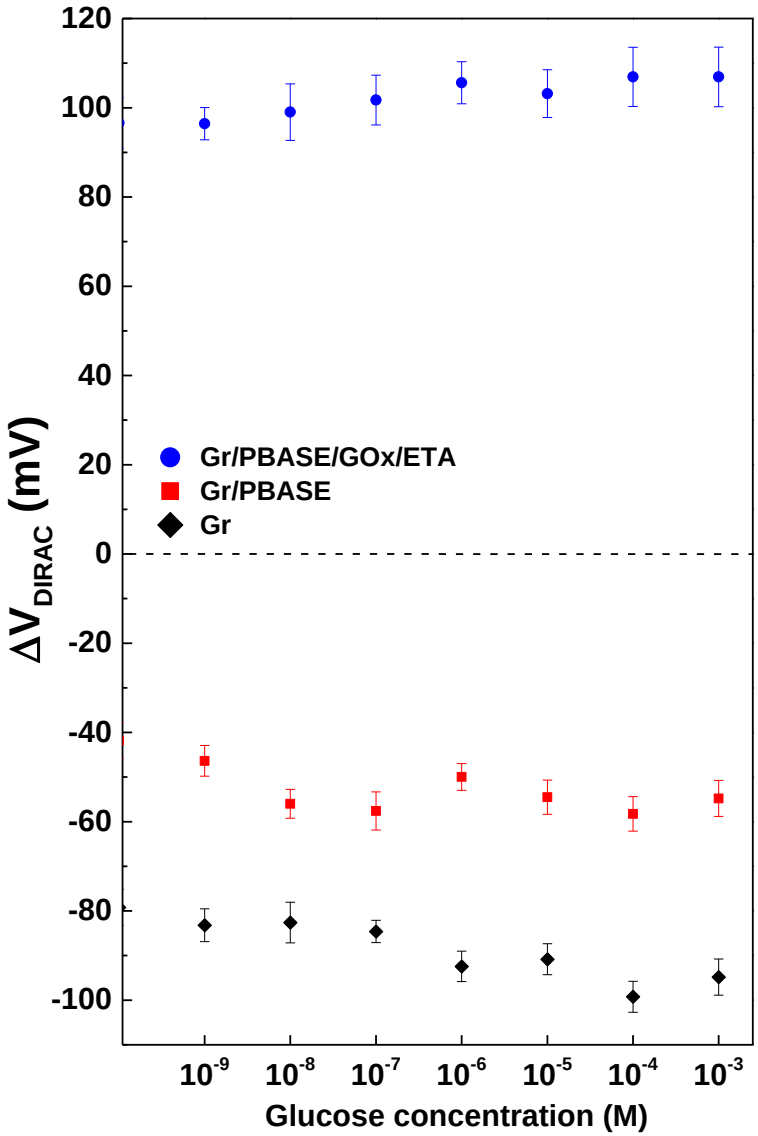


Figure 48: Calibration curves for Gr*, Gr/PBASE and Gr/PBASE/GOx/ETA in nM-mM (saturation) range. The three cases show almost no variation with an increase in glucose concentration.

APPENDIX VII

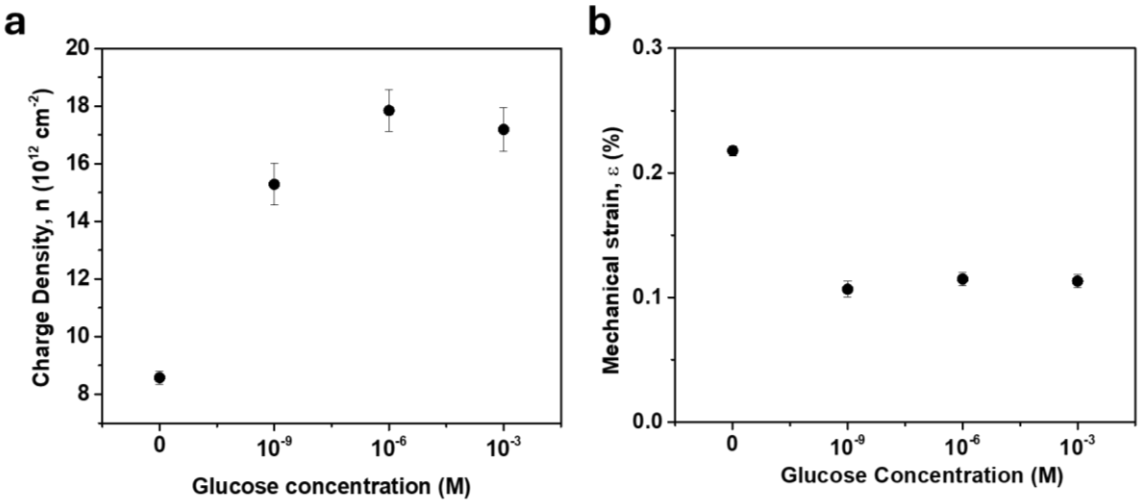


Figure 49: Corresponding (a) charge density and (b) mechanical strain calibration curves extracted from 2D and G position values of Figure 40c. At 1 mM, there is an overall increase in hole concentration of ~9 x 10^{12} cm^{-2}. The mechanical strain varies minimally between concentrations (1 nM-1 mM, with a ~ 0.1% increase in compressive strain only after 1 nM was detected.

APPENDIX VIII

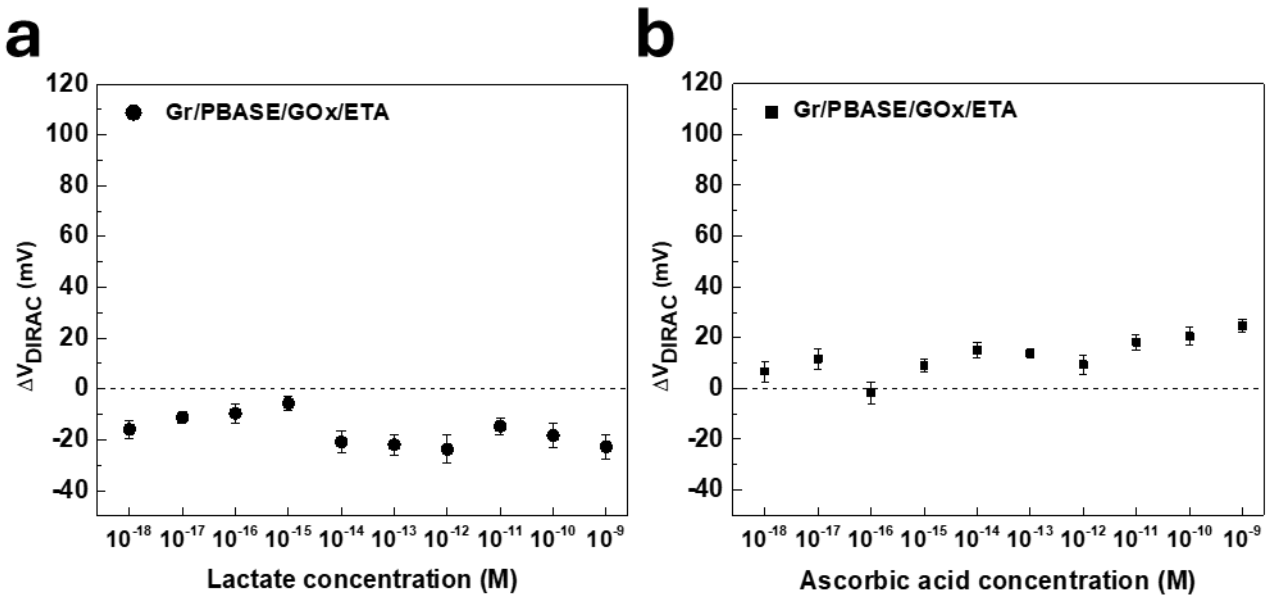


Figure 50: Calibration curve of (a) lactate sensing and (b) ascorbic acid on EG-GFETs in Gr/PBASE/GOx/ETA configuration within the same concentration range as glucose (aM-nM). As opposed to glucose, the sensors had an erratic behavior in response to lactate, proving the selectivity to glucose.

APPENDIX IX

In order to make the characterization of the CL which required a flat surface, the CL had to be flattened without damaging it. Figure 51 shows the one CL after being flattened of a glass coverslip with the black arrows pointing to where the cuts were made to achieve it.

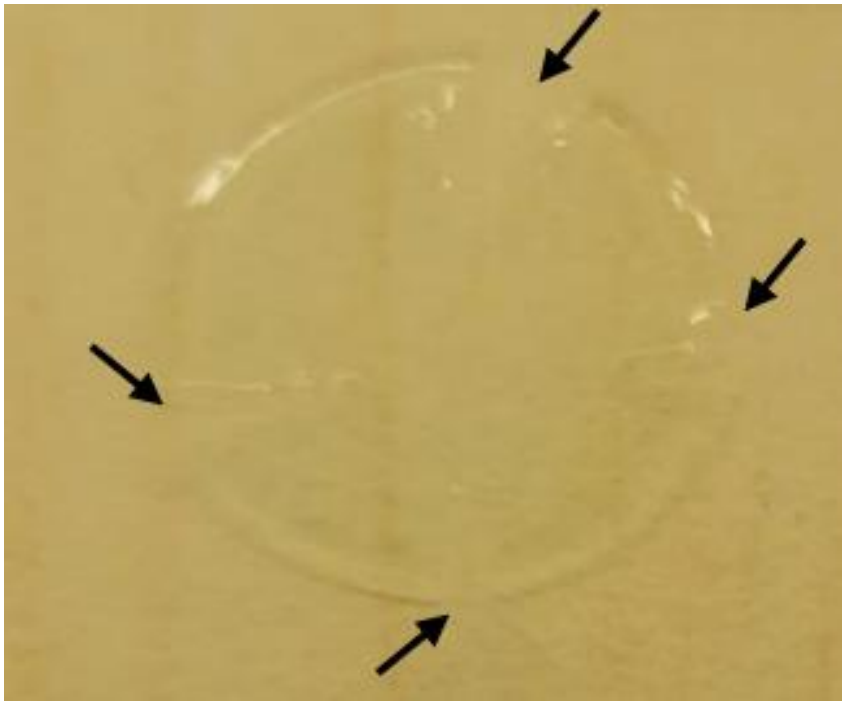


Figure 51: CL after being cut in four different zones pointed by the black arrows and flattened on a glass coverslip between the Au electrodes.

APPENDIX X

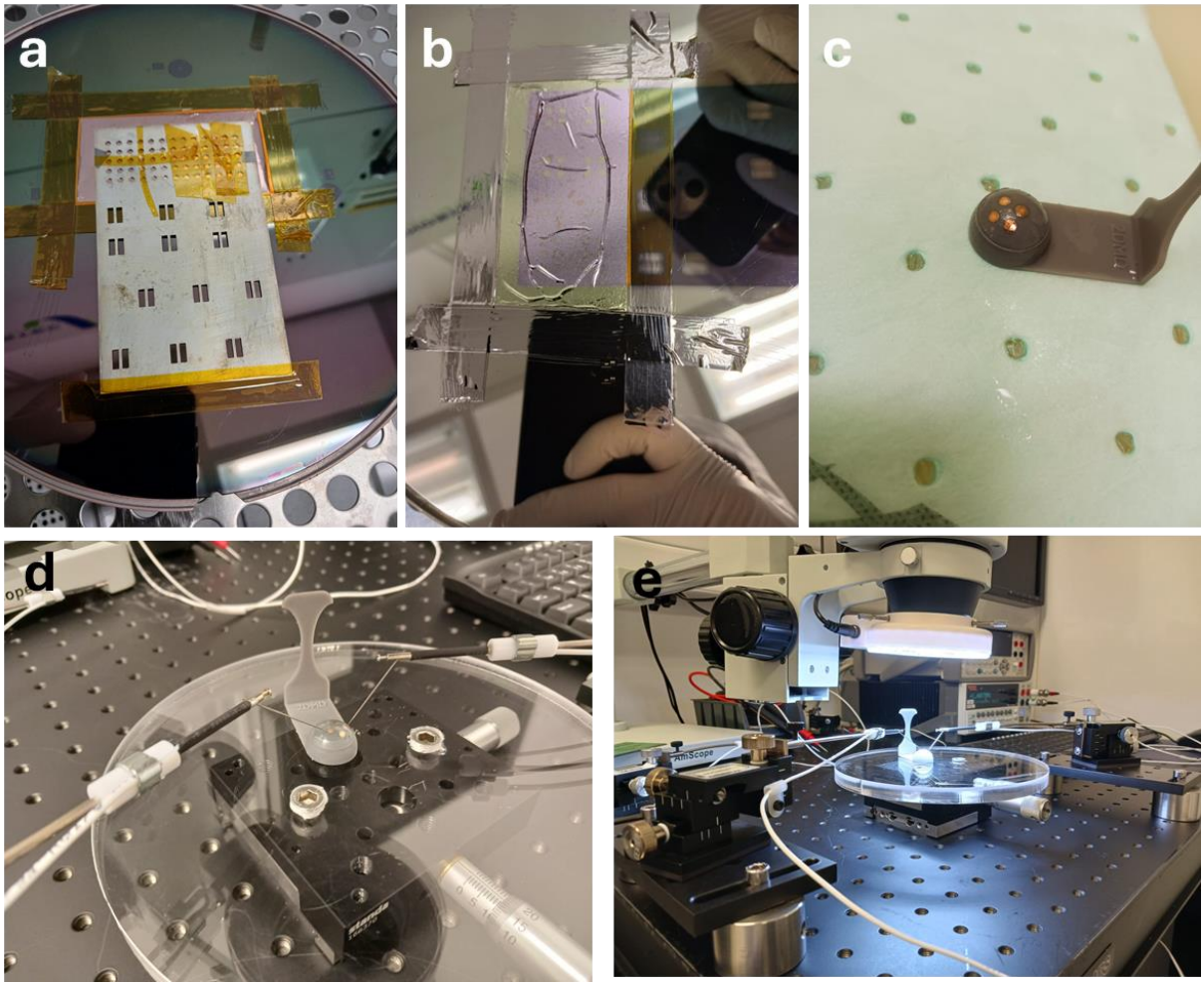


Figure 52: (a) Shadow mask on top of graphene before the sputtering of Au (b) Gr/Cu foil after the sputtering of Au (c) Photograph of the Au electrode/Gr/CL after scooping. (d) Setup of the probe station in the cleanroom. (e) Photographs during the conductivity measurement of the CL using a template as support.

APPENDIX XI

Figure 53a-b shows an optical image near one of the electrodes with 10nm and 30nm thickness, respectively. Figure 53c is the Raman spectra of the crosses shown on Figure 53b, indicating that the graphene got damaged. Figure 53d shows the zone where a map was taken and the Raman spectrum of an average of 225 points.

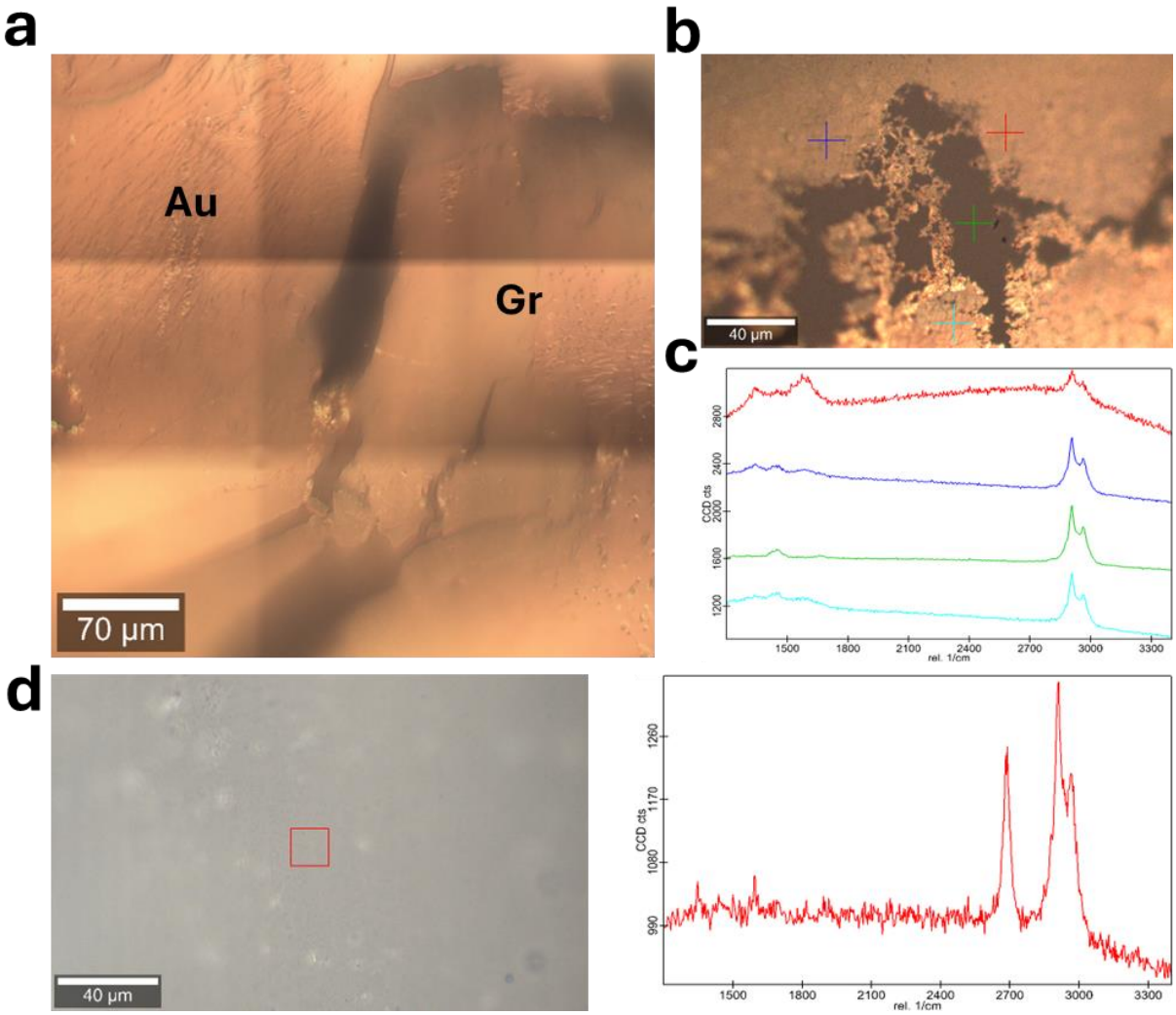


Figure 53: (a) Optical image of the interface between the 10nm Au electrode/Gr-Gr and (b) Optical image of the interface between the 30nm Au electrode/Gr-Gr and (c) Raman Spectra in the indicated crosses in (b).

APPENDIX XII

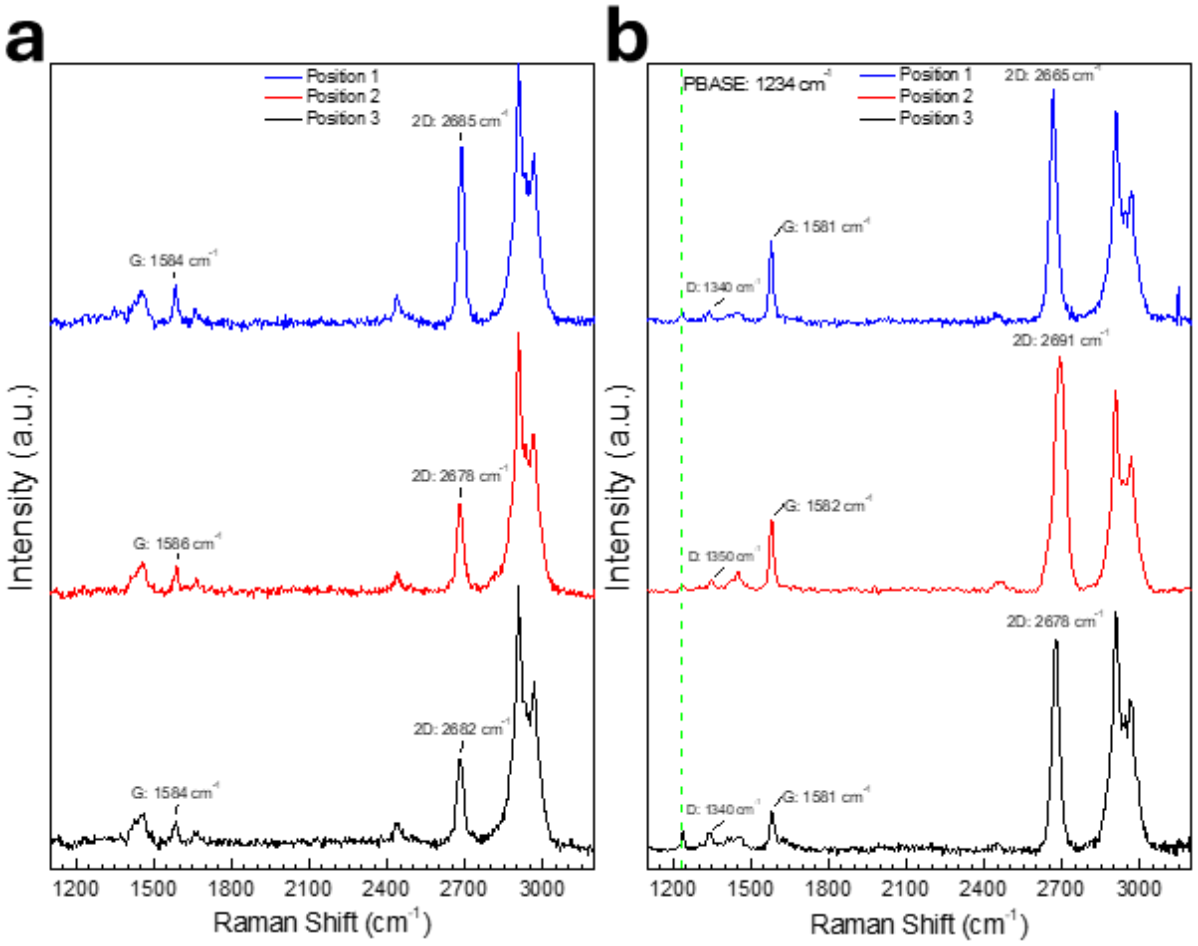


Figure 54: Raman Spectra of the CL (a) before and (b) after the PBASE functionalization in three random positions on the CL.

APPENDIX XIII

Figure 55 shows the change in FWHM of the graphene peaks in each step of the functionalization process on the CL.

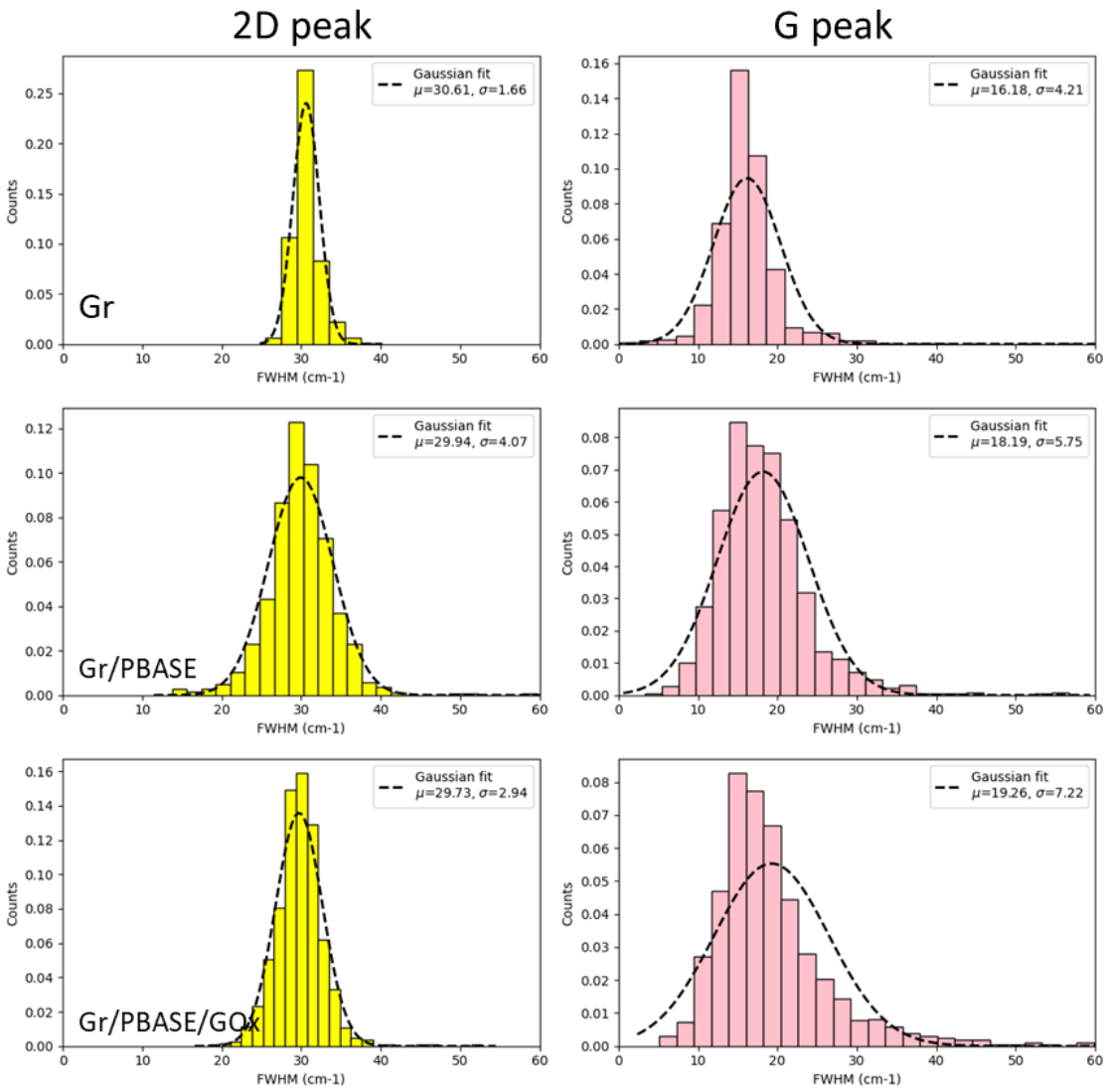


Figure 55: FWHM distribution of the 2D and G peaks of graphene for Gr, Gr/PBASE and Gr/PBASE/GOx on Si/SiO_2.

APPENDIX XIV

Table 4 shows the values, and the changes caused by each functionalization step of graphene on the CL surface and Si/SiO_2 substrate. In both cases there is an increase in the charge density when functionalizing with PBASE and an increase in tensile strain. When functionalizing with GOx, a decrease in both cases of the charge density is observed but with an increase in mechanical strain.

Table 4: Values of the graphene peaks in the functionalization process

Average Values	**2D peak (cm^{-1})**	**G peak (cm^{-1})**	**Mechanical Strain (%)**	**Charge Density (10^{12} cm^{-2})**
CL/Gr	2681.0	1586.9	0.010	11.060
+ PBASE	2684.4 **(+3.4)**	1590.5 **(+3.6)**	0.036 **(+0.026)**	17.551 **(+6.491)**
+ GOx	2683.2 **(-1.2)**	1587.6 **(-2.9)**	0.060 **(+0.024)**	9.989 **(-7.562)**
Si/SiO_2/Gr	2665.8	1580.2	-0.442	11.328
+ PBASE	2667.2 **(+1.4)**	1582.5 **(+2.3)**	-0.296 **(+0.146)**	17.151 **(+5.823)**
+ GOx	2666.9 **(-0.3)**	1580.7 **(-1.8)**	-0.267**(+0.029)**	11.691 **(-5.460)**

APPENDIX XV

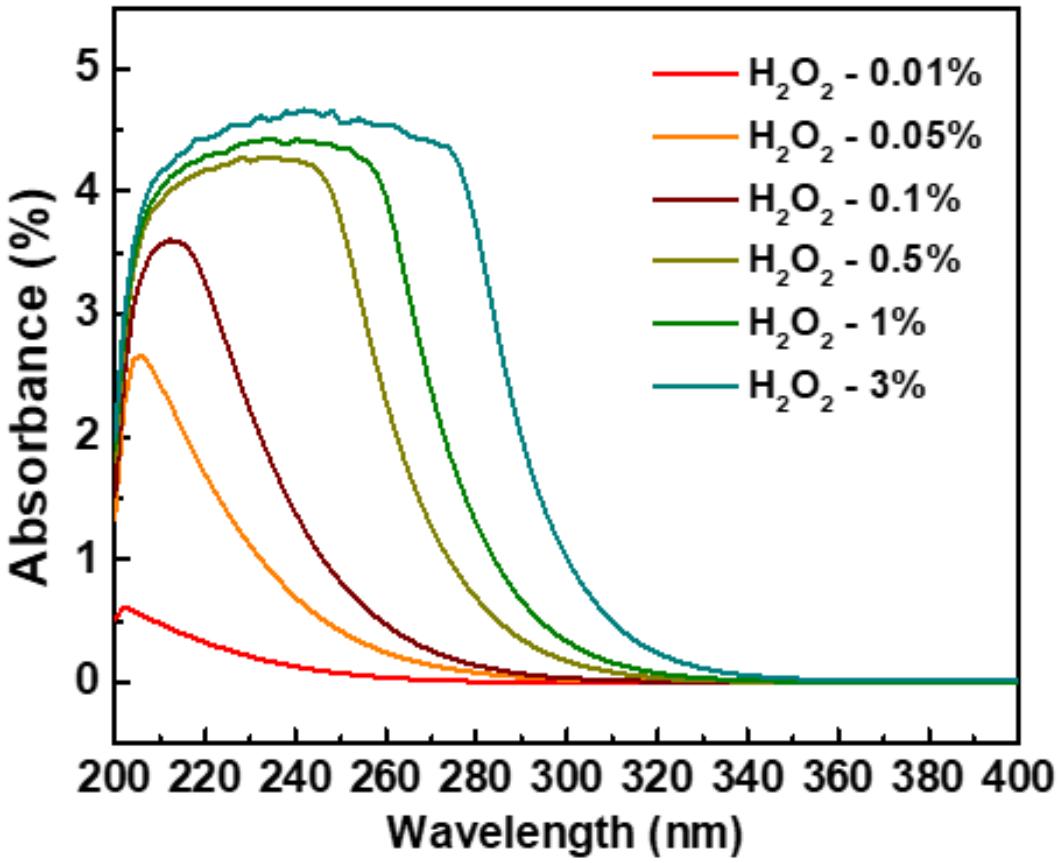


Figure 56: H_2O_2 molecular absorption for different concentrations using PBS a reference.

ANNEX I

This annex presents a succinct overview of additional projects and bodies of work that were conducted during the development of the project.

Posters

1. ESRA Symposium 2024

Primary author of the poster titled: "Towards non-invasive glucose monitoring in contact lenses"

2. CMD31-General Conference of the Condensed Matter Division

One of the authors of the poster titled: Chemical vapor deposited 2D crystals for advanced technologies 2024

Papers

1. "Graphene-based glucose sensors with attomolar limit of detection"

- Submitted to Journal of the American Chemical Society
- Role (1st author): Conducted investigation, formal analysis, and contributed to writing, review, and editing.

2. "Substrate dependent fluorination of CVD graphene for controlled wettability"

- Submitted to ACS Applied Materials & Interfaces
- Role (3rd author): Involved in data acquirement, formal analysis, and contributed to writing, review, and editing.